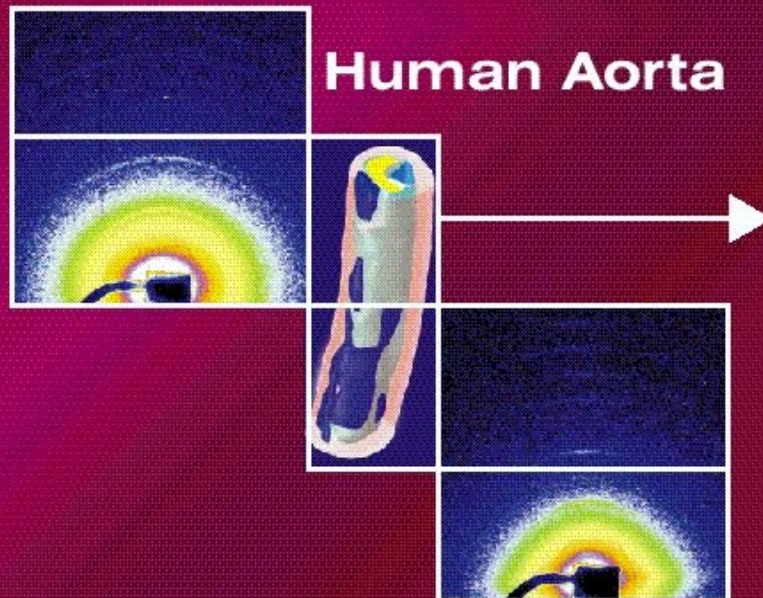




2002

ANNUAL REPORT 2002

BIOMECHANICS:



AUSTRIAN SAXS BEAMLIN AT



Cover pictures: Taken from the user contribution Schulze-Bauer et al. *Layer and age specific tensile testing of human aortas: a small angle x-ray scattering study* (page 88)

Austrian Small Angle X-ray Scattering (SAXS) Beamline at ELETTRA

Annual Report 2002

Compiled by the SAXS-Group:

- for IBR: B. Sartori, M. Rappolt & H. Amenitsch
- for ELETTRA: S. Bernstorff

Table of Contents

	<i>page</i>
› Preface	<i>1</i>
› The SAXS-Group	<i>3</i>
› The SAXS-Beamline in General	<i>4</i>
› Application for Beamtime at ELETTRA	<i>8</i>
› List of Institutes Participating in Experiments	<i>10</i>
› List of Performed Experiments	<i>18</i>
› User Statistics	<i>23</i>
› Experimental Possibilities at the SAXS-beamline	<i>27</i>
1. Latest developments	<i>27</i>
2. Accessible SAXS and WAXS ranges	<i>29</i>
3. Calibration of the s-axis and flat field correction	<i>30</i>
4. Available sample manipulation stages	<i>32</i>
› User Contributions	<i>38</i>
1. Materials Science	<i>39</i>
2. Life Sciences	<i>72</i>
3. Physics	<i>94</i>
4. Chemistry	<i>99</i>
5. Instrumentation	<i>109</i>
› Publications	<i>115</i>
› Author Index	<i>136</i>

Preface

Again, we are glad to present the annual report of the IBR-Elettra SAX beamline. It is an account of a full and successful year, and my thanks are due to all users for their fascinating projects. Equally, of course, to the scientists and technicians working with lasting commitment at the beamline, so that it performs well and improves steadily.

How can one improve something that runs very well? Change management might be one answer, but when and where to start? One thought that jumps to one's mind is people. Beamline scientists are a special brand: they have to present when needed (with a method like SAXS, this is mostly the case), frequently working unsociable hours, and ideally take the user's problem as her/his own. With the dozens of different subjects every period, this is not just physically, but also mentally and intellectually a very demanding task. Career perspectives are not as good as one would like to see them. The own scientific identity, the profile as a researcher are not top in priority. On the other hand, there are few people who are exposed to similarly stimulating and variety of science, as well as to fascinating new horizons of methodology, e.g. the FERMI project.

Every year I use this privileged page to touch on a problem or subject that arises with the management of user facility like SAXS beamline. The one I have touched here may not be close to the minds of users nor of infrastructure responsables at large. Perhaps they lie in a sabbatical scheme?

In any case, the scheme of this operation has been a patent success story for the IBR and Elettra. Let us try to sustain it by remaining open to new ideas.

Peter Laggner
Director
Institute of Biophysics and X-Ray Structure Research
Austrian Academy of Sciences



I am glad to welcome once again a new edition of the annual report of the Austrian SAXS beamline at Elettra. A very broad scientific program encompassing materials science, soft condensed matter and biological systems is developed at this beamline by a community of users from Austria, Italy and a variety of other countries. A constant effort to make the beamline user-friendly, to provide better support to the users from the point of view of technical assistance and of on-site facilities for sample preparation and handling, has produced tangible results over the last few years.

We are looking forward to an increased collaboration between the Elettra laboratory and foreign institutions. I firmly believe that it is good for science in general, and in these days of shrinking research budgets, it is more important than ever to pool resources together and join forces. Elettra is very present, in partnership with many European laboratories, in the competition for EU research funding. International collaboration may be a key factor in the success of some important projects, such as the FERMI@Elettra VUV and soft x-ray free-electron laser. In all such enterprises, we shall proudly show the Austrian – Italian collaboration on the SAXS beamline as a true success story and a showcase of an unbureaucratic, science-driven partnership to the advantage of all.

I am very grateful to the Austrian Academy of Sciences and to the people, whatever their nationality, who are working hard to keep this program so successful.



Massimo Altarelli

Director

Elettra Synchrotron Light Laboratory



The SAXS-Group

HEAD OF PROJECT: Peter Laggner¹⁾
e-mail: Peter.Laggner@oeaw.ac.at

SENIOR SCIENTISTS: Heinz Amenitsch ^{1), 3)}
e-mail: Heinz.Amenitsch@elettra.trieste.it
Sigrid Bernstorff ²⁾
e-mail: Sigrid.Bernstorff@elettra.trieste.it

SCIENTIST: Michael Rappolt ^{1), 3)}
e-mail: Michael.Rappolt@elettra.trieste.it

CHEMICAL ASSISTANT: Barbara Sartori ^{1), 3)} (since April 2003)
e-mail: Barbara.Sartori@elettra.trieste.it

TECHNICIAN: Christian Morello²⁾
e-mail: Christian.Morello@elettra.trieste.it

1) Institute for Biophysics and X-ray Structure Research, Austrian Academy of Sciences,
Schmiedlstraße 6, 8042 Graz, Austria.

Tel 0043-316-4120 302

Fax 0043-316-4120 390

2) Sincrotrone Trieste, Strada Statale 14, km 163.5, 34012 Basovizza (TS), Italy.

Tel 0039-040-375 81

Fax 0039-040-938 0902

3) Institute for Biophysics and X-ray Structure Research, Austrian Academy of Sciences
c/o Sincrotrone Trieste

The SAXS-Beamline in General

Small Angle X-ray Scattering has become a well known standard method to study the structure of various objects in the spatial range from 1 to 1000 nm, and therefore instruments capable to perform such experiments are installed at most of the synchrotron research centers. The high-flux SAXS beamline at ELETTRA is mainly intended for time-resolved studies on fast structural transitions in the sub-millisecond time region in solutions and partly ordered systems with a SAXS-resolution of 1 to 140 nm in real-space.

The photon source is the 57-pole wiggler whose beam is shared and used simultaneously with a Macromolecular Crystallography beamline. The wiggler delivers a very intense radiation between 4 and 25 keV of which the SAXS-Beamline accepts 3 discrete energies, namely 5.4, 8 and 16 keV. The beamline optics consists of a flat double crystal monochromator and a double focusing toroidal mirror.

A versatile SAXS experimental station has been set-up, and an additional wide-angle X-ray scattering (WAXS) detector monitors simultaneously diffraction patterns in the range from 0.1 to 0.9 nm. The sample station is mounted move-able onto an optical table for optimising the sample detector distance with respect to SAXS resolution and sample size.

Besides the foreseen sample surrounding the users have the possibility to install their own specialised sample equipment. In the design phase, besides technical boundary conditions, user friendliness and reliability have been considered as important criteria.

The optimisation of the beamline with respect to high-flux and consequently high flux density, allows to perform the following experiments:

- Low Contrast Solution Scattering
- Grazing Incidence Surface Diffraction
- Micro-Spot Scanning
- X-ray Fluorescence Analysis
- Time-Resolved Studies $\geq 11 \mu\text{s}$
- Simultaneously Performed Small- and Wide-Angle Measurements (SWAXS) on:
 - Gels
 - Liquid Crystals
 - (Bio) Polymers
 - Amorphous Materials
 - Muscles

Furthermore, using 5.4 and 16 keV energies, the beamline is widely applicable also to very thin, e.g. single muscle fibers, and optically thick (high Z) specimen, as often used in e.g., material science and solid state physics.

THE INSERTION DEVICE

The wiggler for the SAXS beamline consists of three 1.5 m long segments, each having 19 poles. The device can work with a minimum gap of 20 mm, which corresponds to $K=20$ at 2 GeV. The main parameters of the wiggler are:

- Critical Energy 4.1 keV
- Radiation Power 8.6 kW
- Flux 3.5×10^{14} ph/s/mrad/0.1%BW (at 400 mA)

The wiggler radiation cone has a horizontal width of 9 mrad. From this the SAXS-beamline accepts vertically 0.3 mrad, and horizontally +/-0.5 mrad at a 1.25 mrad off-axis position. The resulting source size for 8 keV photons is $3.9 \times 0.26 \text{ mm}^2$ (horiz. x vert.).

THE OPTICS

The optics common with the diffraction beamline consists of:

- C-Filter and Beryllium window assembly to reduce the power load on the first optical elements by a factor of 2 and to separate the beamline vacuum from the storage ring.
- Beam defining slit chamber which allows to define the SAXS beam on three sides before the monochromator in order to reduce the straylight in the downstream beamline sections.

The SAXS beamline optics consists of:

- A double-crystal monochromator consisting of four individual chambers, in which three interchangeable asymmetric Si(111) crystal pairs are used to select one of three fixed energies. Each of the crystal pairs is optimised for the corresponding energy to accomplish a grazing angle of 2° . The energy resolution $\Delta E/E$ of the monochromator is in the range of $0.7 - 2.5 \cdot 10^{-3}$.
- A baffle chamber after the monochromator is used as an adjustable straylight fenditure.
- A segmented toroidal mirror focuses the light in horizontal and vertical direction with a 1/2.5 magnification onto the SAXS-detector.
- An aperture slit reduces the straylight after the monochromator and the toroidal mirror.
- A guard slit defines the illuminated region around the focal spot. The spot size on the detector is 1.6 mm horizontally and 0.6 mm vertically. The calculated flux at the sample is in the order of 10^{13} ph/s at 400 mA. For a maximum sample size of $5.4 \times 1.8 \text{ mm}^2$ correspondingly a flux density of 10^{12} ph/s/ mm^2 has been calculated.

SAMPLE STAGE

The multipurpose sample stage allows to perform fast time-resolved relaxation studies based on temperature- or pressure-jumps as well as stopped flow experiments. Shear jump relaxation experiments are planned. Specifically, T-jumps can be induced by an infra-red light pulse (2 ms) from an Erbium-Glass laser, raising the temperature about 20°C in an aqueous sample volume of 10 μl . A hydrostatic pressure cell with a maximal accessible angular range of 30° for simultaneous SAXS and WAXS measurements is available. P-jumps are realised by switching fast valves between a low and a high pressure reservoir, increasing or decreasing the hydrostatic pressure in the range from 1 bar to 2.5 kbar within a few ms. A Differential Scanning Calorimeter (DSC) allows for DSC-scans simultaneously to SWAXS measurements. Also a 1.5 T magnet is available. In an overview, the following sample manipulations are possible (further details, see page 25-34):

- Temperature Manipulations: Ramps, Jumps and Gradient Scans
- Pressure Manipulation: Scan and Jumps
- Stopped Flow Experiments
- SWAXS Measurements Applying Mechanical Stress
- SWAXS Measurements Applying Magnetic Fields
- Calorimetric measurements

Scientific applications	<p>Low Contrast Solution Scattering, Grazing Incidence Surface Diffraction, Micro-Spot Scanning, X-ray Fluorescence Analysis, Time-Resolved Studies $\geq 11 \mu\text{s}$ and Simultaneously Performed Small- and Wide-Angle Measurements (SWAXS) on:</p> <p>Gels Liquid Crystals (Bio) Polymers Amorphous Materials Muscles</p>																								
Source characteristics	<p><u>Wiggler (NdFeB Hybrid):</u></p> <table border="0"> <tr> <td>Period</td> <td>140 mm</td> </tr> <tr> <td>No. full poles</td> <td>57</td> </tr> <tr> <td>Gap</td> <td>20 mm</td> </tr> <tr> <td>B_{max}</td> <td>1.607 T</td> </tr> <tr> <td>Critical Energy ϵ_c</td> <td>4.27 keV</td> </tr> <tr> <td>Power (9 mrad)</td> <td>8.6 kW</td> </tr> <tr> <td>Effective source size FWHM</td> <td>$3.9 \times 0.26 \text{ mm}^2(\text{HxV})$</td> </tr> </table>	Period	140 mm	No. full poles	57	Gap	20 mm	B_{max}	1.607 T	Critical Energy ϵ_c	4.27 keV	Power (9 mrad)	8.6 kW	Effective source size FWHM	$3.9 \times 0.26 \text{ mm}^2(\text{HxV})$										
Period	140 mm																								
No. full poles	57																								
Gap	20 mm																								
B_{max}	1.607 T																								
Critical Energy ϵ_c	4.27 keV																								
Power (9 mrad)	8.6 kW																								
Effective source size FWHM	$3.9 \times 0.26 \text{ mm}^2(\text{HxV})$																								
Optics	<table border="0"> <tr> <td><u>Optical elements:</u></td> <td>Double crystal monochromator: Si (111) asym. cut, water cooled.</td> <td>Mirror: two-segment, toroidal, Pt coated.</td> </tr> <tr> <td><u>Distance from source:</u></td> <td>18.4 m</td> <td>26.5 m</td> </tr> <tr> <td>Acceptance</td> <td colspan="2">1 mrad/0.3 mrad (HxV)</td> </tr> <tr> <td>Energy (3 selectable)</td> <td colspan="2">5.4, 8, 16 keV (0.077, 0.154, 0.23 nm)</td> </tr> <tr> <td>Energy resolution $\Delta E/E$</td> <td colspan="2">$0.7\text{-}2.5 \times 10^{-3}$</td> </tr> <tr> <td>Focal spot size FWHM</td> <td colspan="2">$1.2 \times 0.6 \text{ mm}^2 (\text{HxV})$</td> </tr> <tr> <td>Spot at Sample FWHM</td> <td colspan="2">$5.4 \times 1.8 \text{ mm}^2(\text{HxV})$</td> </tr> <tr> <td>Flux at sample</td> <td colspan="2">$5 \times 10^{12} \text{ ph s}^{-1}(2 \text{ GeV}, 200 \text{ mA}, 8 \text{ keV})$</td> </tr> </table>	<u>Optical elements:</u>	Double crystal monochromator: Si (111) asym. cut, water cooled.	Mirror: two-segment, toroidal, Pt coated.	<u>Distance from source:</u>	18.4 m	26.5 m	Acceptance	1 mrad/0.3 mrad (HxV)		Energy (3 selectable)	5.4, 8, 16 keV (0.077, 0.154, 0.23 nm)		Energy resolution $\Delta E/E$	$0.7\text{-}2.5 \times 10^{-3}$		Focal spot size FWHM	$1.2 \times 0.6 \text{ mm}^2 (\text{HxV})$		Spot at Sample FWHM	$5.4 \times 1.8 \text{ mm}^2(\text{HxV})$		Flux at sample	$5 \times 10^{12} \text{ ph s}^{-1}(2 \text{ GeV}, 200 \text{ mA}, 8 \text{ keV})$	
<u>Optical elements:</u>	Double crystal monochromator: Si (111) asym. cut, water cooled.	Mirror: two-segment, toroidal, Pt coated.																							
<u>Distance from source:</u>	18.4 m	26.5 m																							
Acceptance	1 mrad/0.3 mrad (HxV)																								
Energy (3 selectable)	5.4, 8, 16 keV (0.077, 0.154, 0.23 nm)																								
Energy resolution $\Delta E/E$	$0.7\text{-}2.5 \times 10^{-3}$																								
Focal spot size FWHM	$1.2 \times 0.6 \text{ mm}^2 (\text{HxV})$																								
Spot at Sample FWHM	$5.4 \times 1.8 \text{ mm}^2(\text{HxV})$																								
Flux at sample	$5 \times 10^{12} \text{ ph s}^{-1}(2 \text{ GeV}, 200 \text{ mA}, 8 \text{ keV})$																								
Experimental apparatus	<p><u>Resolution in real space:</u> 1-140 nm (small-angle), 0.1- 0.9 nm (wide-angle)</p> <p><u>Sample stage:</u> temperature manipulations: ramps, jumps and gradient scans, pressure manipulation: scan and jumps, stop flow experiments, SWAXS measurements applying mechanical stress, SWAXS measurements applying magnetic fields. In-line calorimetric measurements simultaneously with SWAXS.</p> <p><u>Detectors:</u> 1D gas-filled detectors for simultaneous small- and wide-angle (Gabriel type), 2D CCD-detector for small-angle.</p>																								
Experiment control	<p><u>Beamline control:</u> Program-units written in LabView for Windows</p> <p><u>1 D detector control:</u> PC-card and software from Hecus & Braun, Graz.</p> <p><u>2 D detector control:</u> Software from Photonic Science, Oxford.</p>																								

CURRENT STATUS

The beamline has been built by the Institute for Biophysics and X-ray structure Research (IBR), Austrian Academy of Science in collaboration with staff members from Sincrotrone Trieste, and is in user operation since September 1996. The set-up of the beamline started at the beginning of January 1995 with the installation of the support structure. Until the end of 1995, the 8 keV single energy system had been realised. The upgrade to the full three energy system was finished in spring 1998. Time resolved experiments require fast X-ray detectors and data acquisition hard- and software. Depending on the desired resolution in time and in reciprocal space, on isotropic or anisotropic scattering of the sample, one-dimensional position sensitive (delay-line type) or two-dimensional CCD detectors are employed.

In August 2002 our new chemistry and X-ray laboratory went into operation. The chemistry unit serves mainly for sample preparation and analysis for both, in house research and external user groups, whereas the X-ray laboratory allows on-site testing of samples before moving on to the SR beamline (see also *latest developments*, page 27).

In conclusion, due to wide versatility of the beamline and the highly flexible sample stage, there are nearly no limits for the realisation of an experiment, and you are welcome by our team to propose any interesting and highlighting investigation for the benefit of material and life sciences.

Application for Beamtime at ELETTRA

1. Beamtime Policy at SAXS beamline

According to the agreement from March 2001 regarding the co-operation between the Austrian Academy of Sciences and Sincrotrone Trieste, at the Austrian SAXS-beamline the available beamtime of about 5000 hours/year is distributed as follows:

- 35% for Austrian Users, type: "CRG" (Collaborating Research Group)
- 35% for Users of Sincrotrone Trieste (General Users (GU))
- 30% is reserved for beamline maintenance and in-house research

In both user beamtime contingents also any industrial, proprietary and confidential research can be performed according to the "General User Policy" of Sincrotrone Trieste.

To apply for CRG and GU user beamtime proposals must be submitted according to the rules of Sincrotrone Trieste. The international review committee at ELETTRA will rank the proposals according to their scientific merit assessment. Based on this decision beamtime will be allocated according to the specific quotes for the beamtimes (CRG/GU) either for the following semester ("normal application") or for the next two years ("long term application"). However, at the moment no more than a maximum of 10% of the beamtime will be assigned to "long term" projects.

2. How to apply for beamtime

There are two deadlines each year for proposals, namely August 31st and February 28th. Accepted proposals will receive beamtime either in the then following first or second half year period, respectively. The Application Form must be completed on-line according to the following instructions. In addition, one printed form is also required and must be send to:

ELETTRA USERS OFFICE
Strada Statale 14 - km 163.5
34012 Basovizza (Trieste), ITALY
Tel: +39 040 3758628 - fax: + 39 040 3758565
e-mail: useroffice@elettra.trieste.it

INSTRUCTIONS GIVEN BY THE USERS OFFICE
(see also: www.elettra.trieste.it/experiments/index.html)

1. Read carefully the following Guidelines.
2. Connect to the Virtual Users' Office: <http://users.elettra.trieste.it> using your favorite browser (Netscape 3.0 or above, Internet Explorer 4.0 or above, etc.) with JavaScript enabled.
3. Select the Virtual Users Office link.

4. When prompted, insert your ID and password. If you are a new user fill in the registration form with your data and choose your institution with the search button; in case your institution does not appear in the list, please contact useroffice@elettra.trieste.it giving all the details about it. When registered, you will receive an acknowledgment with your ID and password. You can change your password, if you wish. In case you forget your password, please don't register again but contact useroffice@elettra.trieste.it. At any moment you can select the help button and view more detailed instructions. By inserting your ID and password you will be able to continue.
5. Select the proposals button in the User functions group.
6. Select add and fill in on-line the proposal form. Please, type your proposal in English. Repeat this procedure for each proposal you intend to submit.
7. In case of continuation proposal: a) attach the experimental report of previous measurements; b) give your previous proposal number.
8. When finished, submit the proposal electronically, selecting the save button.
9. Print the proposal form together with each related safety form.
10. Sign the safety form(s).
11. Mail one complete printed copy to the Users Office.

NOTE

From July 2002 on there exists a new possibility for users from developing countries to apply for financial support for their travel expenses. For all other users everything remains as before. For further information, please have a look into the web-pages

http://www.elettra.trieste.it/experiments/users_handbook/index.html)

or contact the USERS OFFICE.

List of Institutes Participating in Experiments

Austria

Austrian Academy of Science, Erich Schmid Institute of Materials
Science, Leoben

AICHMAYER Barbara
FRATZL Peter
GUPTA Himadri Shikhar
MISOF Klaus
VALENTA Angelika
WEBER Markus

Austrian Academy of Science, Institute for Biophysics and X-ray Structure Research,
Graz

AMENITSCH Heinz
KRIECHBAUM Manfred
LAGGNER Peter
LOHNER Karl
PABST Georg
POZO-NAVAS Beatriz
PROSSNIG F.
RAPPOLT Michael
STROBL Marlene

LKT-TGM, Laboratorium für Kunststofftechnik G.m.b.H, Wien

WILHELM Harald

Ludwig Boltzmann-Institut of Osteology, 4th Medical Department, Hanusch-Hospital
& UKH-Meidling Hospital, Vienna

KLAUSHOFER Klaus
ROSCHGER Paul

Technische Universität Wien, Institut für Werkstoffkunde und
Materialprüfung, Wien

KOCH Thomas
SPITZBART Manfred

Technische Universität Graz, Institut für Computational Biomechanics, Graz

HOLZAPFEL G.A.
SCHULZE-BAUER Christian A.J.
SOMMER Gerhard

University of Vienna, Institute of Material Physics, Vienna
Universität Wien, Institut für Materialphysik, Wien

PARIS Alfred
SCHAFLER Erhard
ZEHETBAUER Michael

Bulgaria

Sofia University, Faculty of Physics, Department of General Physics, Sofia
TODOROVA G.

Croatia

"Ruder Boskovic" Institute, Zagreb

BULJAN Maya
DESNICA-FRANKOVIC Ida-Dunja
DESNICA Uros V.
DUBCEK Pavo
KOVACEVIC Ivana
PIVAC Branko
RADIC Nikola

University of Zagreb, Institute of Physics, Zagreb

MILAT Ognjen
SALAMON Kresimir

Czech Republic

Academy of Sciences of the Czech Republic, Institute of Macro- molecular
Chemistry, Prague

BALDRIAN Josef
SIKORA A.

Joint Laboratory of Solid State Chemistry, Institute of
Macromolecular Chemistry, Academy of Sciences and University of
Pardubice, Pardubice

BENES Ludvik
MELÁNOVÁ Klara
ZIMA Vitezslav

University of Pardubice, Pardubice

STEINHART Milos

Finland

Åbo Akademi University, Dept. of Physical Chemistry, Materials Research Group,
Turku

LINDÉN Mika
TIEMANN Michel
LIND Anna

France

Arilait Recherches, Paris

LOPEZ Christelle

Equipe Physico-Chimie des Systèmes Polyphasés, Chatenay-Malabry

ALLAIS Celile

KALNIN Daniel

KELLER Gerhard

OLLIVON Michel

Nestlé S.A. PTC, Beauvais

WILLE H.

Université Blaise Pascal - Clermont-Ferrand II / C.N.R.S. –

Laboratoire de Thermodynamique des Solutions et des Polymères,

Aubière Cedex, Paris

GAETAN Bergin

SAIANI Alberto

STACHOWIAK Christian

Université de Grenoble J. Fourier - Laboratoire de Grenoble J.

Fourier - Laboratoire de Spectrométrie, Grenoble

ROCHAS Cyrille

University Paris 6, Chimie de la Matière Condensée, Paris

BABONNEAU Florence

BLUM R.

GOLETTO V.

CREPALDI Eduardo

GROSSO David

MAMMERI Fayna

SOLER-ILLIA Galo

Germany

Forschungszentrum Jülich, Abteilung IFF

HITOSHI Endo

Hamburger Synchrotronstrahlungslabor (Hasylab), Hamburg

FLEGE Jan-Ingo

Johannes Gutenberg Universität, Institut für Anorganische Chemie und Analytische Chemie, Mainz (D-55099 Mainz, Duesbergweg 10-14, hanh@mail.uni-mainz.de))

HAHN Andreas

ZOEFRE Bayraun

Max-Planck-Institut für Kohlenforschung, Mülheim / Ruhr

TEIXEIRA Cilaine Veronica

Max-Planck-Institut for Colloids and Interfaces, Golm

DUFAU Natalie

SCHMIDT Wolfgang

WEISS Oezlem

Universität Augsburg, Institut für Physik
GROSSHANS I.
KARL Helmut
STRITZKER B.

Universität Bremen, Institut für Festkörperphysik
ALEXE Gabriela
CLAUSEN Torben
FALTA Jens
GANGODADYHAY Subhasish
HOMMEL Detlev
SCHMIDT Thomas

Universität Karlsruhe, Institut für Angewandte Physik
PASSOW Thorsten

Universität–GH Siegen, Fachbereich Physik, Siegen
BESCH Hans-Juergen
ORTHEN Andre'
WAGNER Hendrik
WALENTA Albert Heinrich

Hungary

Eötvös University, Institute for General Physics, Budapest
RIBARIK G.
UNGÁR Tamas

India

Inter University Consortium for DAE Facilities, Univ. Campus, Khandwa Road,
Indore

GUPTA Ajay
REDDY V. Raghavendra
SARAIY Amit
SHARMA Pooja

Inter University Consortium for DAE Facilities, BARC, Mumbai
GOYAL Prem S.

Solid State and Structural Chemistry, IISC, Bangalore
SAPRA S.
SARMA D.D.
VISWANATHA R.

Italy

CNR, direzione progetto finalizzato biotecnologie, Genova
GIOVINE Marco

CNR, Istituto per l'Energetica e le Interfasi (IENI), Genova
BUSCALIA V.

CNR, Istituto Processi Chimico-Fisici, Messina
TRIOLO Alessandro

MEMC Electronic Materials, Merano
PORRINI M.

Sincrotrone Trieste, Trieste
BERNSTORFF Sigrid
MENK Ralf
MORELLO Christian

Università Politecnica delle Marche, Istituto di Scienze Fisiche, and INFN, Ancona
AUSILI P.
DI GREGORIO Giordano M.
FEDERICONI Francesco
MARIANI Paolo
PACCAMICCIO Lydia
SATURNI Letizia
SPINOZZI Francesco

Università Politecnica delle Marche, Dipartimento di Fisica e Ingegneria dei Materiali e del Territorio, Ancona
PISANI Michela

Università di Ancona, Ist. Scienza del Mare
BAVESTRELLO G.

Università di Firenze, Dip. Scienze Fisiologiche, Firenze
BAGNI Maria Angela
CECCHI Giovanni
COLOMBINI Barbara

Università di Genova, DIMES sez. Biochimica, Genova
BENATTI Umberto

Università di Genova, Dip. Te. Ris. Genova
CERRANO Carlo

Università di Milano Bicocca, Dipartimento di Scienza dei Materiali,
Milano
BORGHESI A.
SASSELLA A.

Università di Modena, Dipartimento di Fisica, Modena
CORNI Federico
OTTARINI Gianpiero
TORINI Rita

Università di Napoli, Dipartimento di Chimica, Napoli
PADUANO L.

Università di Padova, Dip. di Biologia, Padova
GATTO Sara
BELTRAMINI Mariano

Università di Padova, Dip. di Fisica, e Istituto Nazionale di Fisica Nucleare, Sezione di Padova, Padova
DE JULIAN FERNANDEZ, Cesar

Università di Padova, Dep. of Mechanical Engineering, Padova
FALCARO Paolo

Università di Padova, Dep. of Organic Chemistry, Padova
MAGGINI M.

Università di Palermo, Dipartimento di Chimica Fisica, Palermo
LO CELSO Fabrizio
TRIOLO Roberto

Università di Perugia, Dipartimento di Fisica and INFN, Perugia
CINELLI Stefania
MACCHEGANI Stefania
ONORI G.

Università del Piemonte Orientale „A.Avogadro“, Dip. Scienze e Tecnologie Avanzate (DISTA), Alessandria
CAUSA' M.
CROCE Gianluca
FRACHE Alberto
MARCHESE L.
MILANESIO Marco
VITERBO Davide

Università di Sassari, Dipartimento di Architettura e Pianificazione, Laboratorio di Scienza dei Materiali e Nanotecnologie, Alghero
INNOCENZI P.

University of Trieste, Dep. of Biochemistry, Biophysics and Macromolecular Chemistry, Trieste
CESÀRO Attilio
SUSSICH Fabiana

University of Trieste, Trieste
VOLTOLINA Francesco

Poland

Polish Academy of Sciences, Institute of Metallurgy and Material Science, Krakow
BONARSKI Jan T.
TARKOWSKI L.

Slovenia

Josef Stefan Institute, Ljubljana
ZIDANSEK Alexander

Spain

Instituto de Ciencia de Materiales de Madrid
HERNANDO-MANERU Antonio
PALOMARES F. Javier

Switzerland

Ecole Polytechnique Fédérale de Lausanne, Laboratoire Technologie
des Poudres, Lausanne
BOWEN P.
JONGEN Nathalie
SOARE Lucia C.

ETH Zurich & Paul Scherrer Institute, Laboratory for Neutron
Scattering, Villigen
GUPTA Mukul

Nestle Research Center, Lausanne
SCHAFFER Olivier

Paul Scherrer Institute, Spallation Neutron Source Division, Villigen
ASWAL Vinod K

United Kingdom

Cambridge University, Cavendish Laboratory
GAETAN Bergin
MILLER Aline
STACHOWIAK Christian

Keele University, Department of Physics, Keele
FULLER Watson
ARUMUGAM Mahendrasingam
WRIGHT Anthony

University Laboratory of Physiology, Oxford
ASHLEY Christopher C
GRIFFITHS Peter J.

USA

Oak Ridge National Laboratory, Oak Ridge TN
WHITE C.W.

List of Performed Experiments

2002 (first half year)

Proposal	Proposer	Institution	Country	Title	Research Area
2001267	Saiani Alberto	Université Blaise Pascal - Clermont-Ferrand II / C.N.R.S. - Laboratoire de Thermodynamique des Solutions et des Polymères U.M.R. Aubière, Cedex	France	Gelation dynamics and mechanism(s) in syndiotactic PMMA	Chemistry
2001286	Viterbo Davide	Università di Torino - Dip. di Chimica I.F.M.	Italy	High resolution fiber diffraction for structure elucidation of silicatein filaments in spicules from different sponges	Materials Sciences
2001344	Baldrian Josef	Czech Acad. of Sciences, Inst. of Macromol. Chemistry, Prague	Czech Republic	Time-resolved SAXS/WAXS Studies on Macromolecular Materials: Cocrystallization Dynamics in Lamellar Systems of PEO/PEO and PEO/PEO-PPO Blends	Physics
2001348	Grosso David	Université Paris 6 Chimie de la Matière Condensée	France	In-situ SAXS study of functionalised mesoporous film formation	Chemistry
2001349	Lo Celso Fabrizio	Università di Palermo Dip. Di Chimica Fisica	Italy	Mixtures of reverse pluronic copolymer and surfactants as controlled-release drug delivery systems.	Materials Sciences
2001358	Sussich Fabiana	Università di Trieste, Dipartimento di Biochimica, Biofisica e Chimica delle Macromolecole (BBCM)	Italy	Mechanism and application of trehalose biopreservation: interaction with model lipid membranes	Life Sciences
2001362	Schulze-Bauer Christian	Institute for Structural Analysis, Computational Biomechanics, Technische Universität Graz	Austria	SAXS investigation of layer-specific collagen structures in arteries under tension	Life Sciences
2001382	Lo Celso Fabrizio	Università di Palermo Dip. di Chimica Fisica	Italy	Structural Investigation on Phospholipidic-Cyclodextrin Derivatives	Materials Sciences
2001385	Gupta Himadri Shikhar	Erich Schmid Institute for Material Sciences AAS, Leoben,	Austria	Structure-function relations in demineralized collagen and collagen with variable cross-linking.	Life Sciences
2001401	Arumugam Mahendrasingam	Keele University - Dept. of Physics, School of Chemistry and	United Kingdom	Molecular reorganisation prior to strain induced crystallisation in polyesters	Chemistry

		Physics, Keele			
2001411	Jongen Nathalie	Ecole Polytechnique Federale de Lausanne, Laboratoire Technologie des Poudres, Lausanne	Switzerland	Epitaxial Self-Assembly of Nanocrystallites – A New Particle Growth and Design Mechanism	Materials Sciences
2001428	Falta Jens	Universität Bremen -Institut für Festkörperphysik	Germany	Structural characterization of thin SiNx films on Si(111)	Materials Sciences
2001433	Falta Jens	Universität Bremen -Institut für Festkörperphysik	Germany	Ordering of buried CdSe quantum dots on ZnSe	Materials Sciences
2001435	Zidansek Aleksander	Institute Jozef Stefan, Ljubljana	Slovenia	Smectic Ordering of Liquid Crystal 8CB Confined to CPG Glasses	Chemistry
2001436	Laggner Peter	IBR, AAS, Graz	Austria	Self-Assembly and Structural Dynamics of Membrane-Mimetic Systems at Solid Surfaces 1. Self alignment of lipid films on surfaces studied with surface diffraction 2. X-ray surface diffraction to study highly aligned phospholipids under influence of amphiphilic molecules and salt 3. Unbinding transition of lipid multibilayers	Life Sciences
2001442	Zehetbauer Michael	Univ. Wien Institut für Materialphysik	Austria	Synchrotron WAXS & SAXS Studies of Microstructural Evolution During Post-Yield Deformation of Isotactic Polypropylen (pt. II)	Materials Sciences
2001445	Zehetbauer Michael	Univ. Wien Institut für Materialphysik	Austria	Time and Space Resolved Scanning Synchrotron X-ray Profile Analyses during Plastic Deformation of BCC and HCP Metals, pt. II	Materials Sciences
2001115	Besch Hans-Juergen	Universität GHS Siegen, Dept. of Physics	Germany	LONG TERM: Test measurements on advanced gaseous detectors for time-resolved SAXS	Instrumentation
2001229	Laggner Peter	IBR, AAS, Graz	Austria	LONG TERM: as prop. 2001436	Life Sciences
In-house	Bernstorff, Desnica Uros, Desnica-Frankovic Dunja	Sincrotrone Trieste + Rudjer Boskovic Institute, Zagreb	Italy / Croatia	Study of nanocrystalline wide-band-gap semiconductors formed by ion implantation	Materials Sciences
In-house	Amenitsch, Babonneau Florence	IBR, AAS + Université Paris 6, Chimie de la Matière Condensée	Austria / France	In-situ X-ray diffraction study of the formation of mesoporous organosilicates under acidic conditions.	Chemistry

In-house	Amenitsch, Ollivon Michel	IBR, AAS + CNRS UMR 8612, University Paris- Sud, 5	Austria / France	Triglyceride crystallisation in milk emulsions at subzero temperatures : Study of liquid- crystalline structures and phase transitions by coupling of Differential Scanning Calorimetry and High Resolution Small Angle X-ray Scattering.	Life Sciences
In-house	Bernstorff, Pivac Branko, Dubcek Pavo	Sincrotrone Trieste + Rudjer Boskovic Institute, Zagreb	Italy / Croatia	Grazing incidence small angle X- ray scattering investigation of structural changes in annealed deuterium implanted monocrystalline silicon	Materials Sciences
In-house	Bernstorff, Pivac Branko, Dubcek Pavo	Sincrotrone Trieste + Rudjer Boskovic Institute, Zagreb	Italy / Croatia	Oxygen precipitation in Cz single crystal Si	Materials Sciences
In-house	Bernstorff, Pivac Branko, Dubcek Pavo	Sincrotrone Trieste + Rudjer Boskovic Institute, Zagreb	Italy / Croatia	Defects in amorphous silicon	Materials Sciences
Pilot	Gubaidullin Aidar	Arbuzov Institute of Organic and Physical Chemistry - Kazan Scientific Center - Russian Academy of Sciences, Kazan	Russia	Investigation of microheterogeneities in nonlinear optical cross-linked polymers	Chemistry
Pilot	Palomares Javier	Consejo Superior de Investigaciones Cientificas - Instituto Ciencia de Materiales	Spain	Grazing Incidence Small-Angle X-ray Scattering and X-ray Diffraction study of magnetic nanoparticulate films grown by Pulsed Laser Deposition	Materials Sciences

2002 (second half year)

Proposal	Proposer	Institution	Country	Title	Research Area
2002008	Aswal Vinod Kumar	S.L.S. -Paul- Scherrer Institut, Villigen	Switzerland	SAXS study for the first direct observation of the selective counterion condensation around the ionic micelles	Chemistry
2002016	Griffiths Peter John	University Laboratory of Physiology, Oxford	United Kingdom	Mechanical and structural studies of states of myosin head domain tilt in different contractile states.	Life Sciences
2002030	Mariani Paolo	Università di Ancona - Ist. di Scienze Fisiche	Italy	Structure and self-assembling properties of guanosine four- stranded helices in dilute solutions	Life Sciences

2002034	Falta Jens	Universität Bremen -Institut für Festkörperphysik	Germany	Ordering of buried CdSe quantum dots on ZnSe	Materials Sciences
2002036	Gupta Ajay	Inter University Consortium for DAE Facilities - University Campus, Indore	India	Study of swift heavy ion induced intermixing in metal/silicon thin films	Materials Sciences
2002041	Innocenzi Plinio	Università di Padova - Dip. Ingegneria Meccanica (Settore Materiali)	Italy	Small angle X-ray scattering study of self-assembled mesoporous thin films doped with fullerene derivatives	Chemistry
2002059	Mariani Paolo	Università di Ancona - Ist. di Scienze Fisiche	Italy	Pressure-assisted cold denaturation of metmyoglobin by SAXS	Life Sciences
2002110	Grosso David	Université Paris 6, Chimie de la Matiere Condensee	France	In-situ study of thermal crystalisation of transition metal oxide mesoporous films	Chemistry
2002120	Laggner Peter	Institute of Biophysics and X-ray Structure Research (IBR), Austrian Academy of Sciences (AAS), Graz	Austria	Self-Assembly and Structural Dynamics of Membrane-Mimetic Systems at Solid Surfaces 1. Self alignment of lipid films on surfaces studied with surface diffraction 2. X-ray surface diffraction to study highly aligned phospholipids under influence of amphiphilic molecules and salt 3. Unbinding transition of lipid multibilayers	Life Sciences
2002147	Linden Mika	ÅBO Academi University - Dept. of Physical Chemistry, Materials Research Group,, Turku	Finland	In situ SAXS study of the initial stages of particle nucleation and growth from solution with microsecond resolution	Chemistry
2002157	Koch Thomas	Technische Universität Wien, Institut für Werkstoffkunde und Materialprüfung	Austria	Morphology and microhardness of alpha- and beta-spherulites of iPP and ethylene-propylene random copolymer	Materials Sciences
2002172	Desnica Uros	Rudjer Boskovic Institute, Zagreb	Croatia	Study of semiconductor quantum dots formed by ion implantation	Materials Sciences
2002183	Grosso David	Université Paris 6, Chimie de la Matiere Condensee	France	In-situ SAXS study of the organisation of organically modified silica meso-structured films (influence of the chemical parameters)	Chemistry
2002242	Gupta Himadri Shikhar	Erich Schmid Institute for Material Sciences, AAS, Leoben	Austria	Investigation of tendon size effects and synchrotron radiation damage on in-situ tensile testing of collagen	Life Sciences
2002246	Zehetbauer Michael	Univ. WIEN, Institut für Materialphysik	Austria	Synchrotron WAXS & SAXS Studies of Microstructural Evolution during Post-Yield Deformation of Isotactic Polypropylen (pt. III)	Materials Sciences

2001229	Laggner Peter	IBR, AAS, Graz	Austria	LONGTERM: as Prop. 2002120	Life Sciences
2001115	Besch Hans- Juergen	Universität GHS Siegen, Dept. of Physics	Germany	LONGTERM: Test measurements on advanced gaseous detectors for time- resolved SAXS	Instrumen- tation
In-house	Bernstorff, Pivac Branko, Dubcek Pavo	Sincrotrone Trieste + Rudjer Boskovic Institute, Zagreb	Italy / Croatia	GISAXS study of irradiation induced defects in monocrystalline silicon	Materials Sciences
In-house	Laggner, Amenitsch, Ollivon Michel	IBR, AAS, Graz + CNRS UMR 8612, University Paris- Sud	Austria / France	Triglyceride crystallisation in milk emulsions at subzero temperatures : Study of liquid- crystalline structures and phase transitions by coupling of Differential Scanning Calorimetry and High Resolution Small Angle X-ray Scattering.	Life Sciences
In-house	Bernstorff, Radic Nicola, Dubcek Pavo	Sincrotrone Trieste + Rudjer Boskovic Institute, Zagreb	Italy / Croatia	Characterisation of grains in Tungsten-Carbon films	Materials Sciences
In-house	Steinhart Milos	Czech Academy of Sciences - Inst. of Macromolecular Chemistry, Prague	Czech Republik	Study of Phase Properties of Intercalates by SWAXS	Physics
Pilot	Sarma D.D.	IISc, dept. Solid State and Structural Chemistry, Bangalore	India	Study of the growth process in semiconducting CdS nanoparticles	Materials Sciences

User Statistics

1. Number of submitted proposals and assigned shifts from 1995 until December 2002

The Austrian SAXS-beamline at ELETTRA opened to users in September 1996. Since then many experiments have been performed related to the fields of life science, materials science, physics, biophysics, chemistry, medical science, technology and instrumentation.

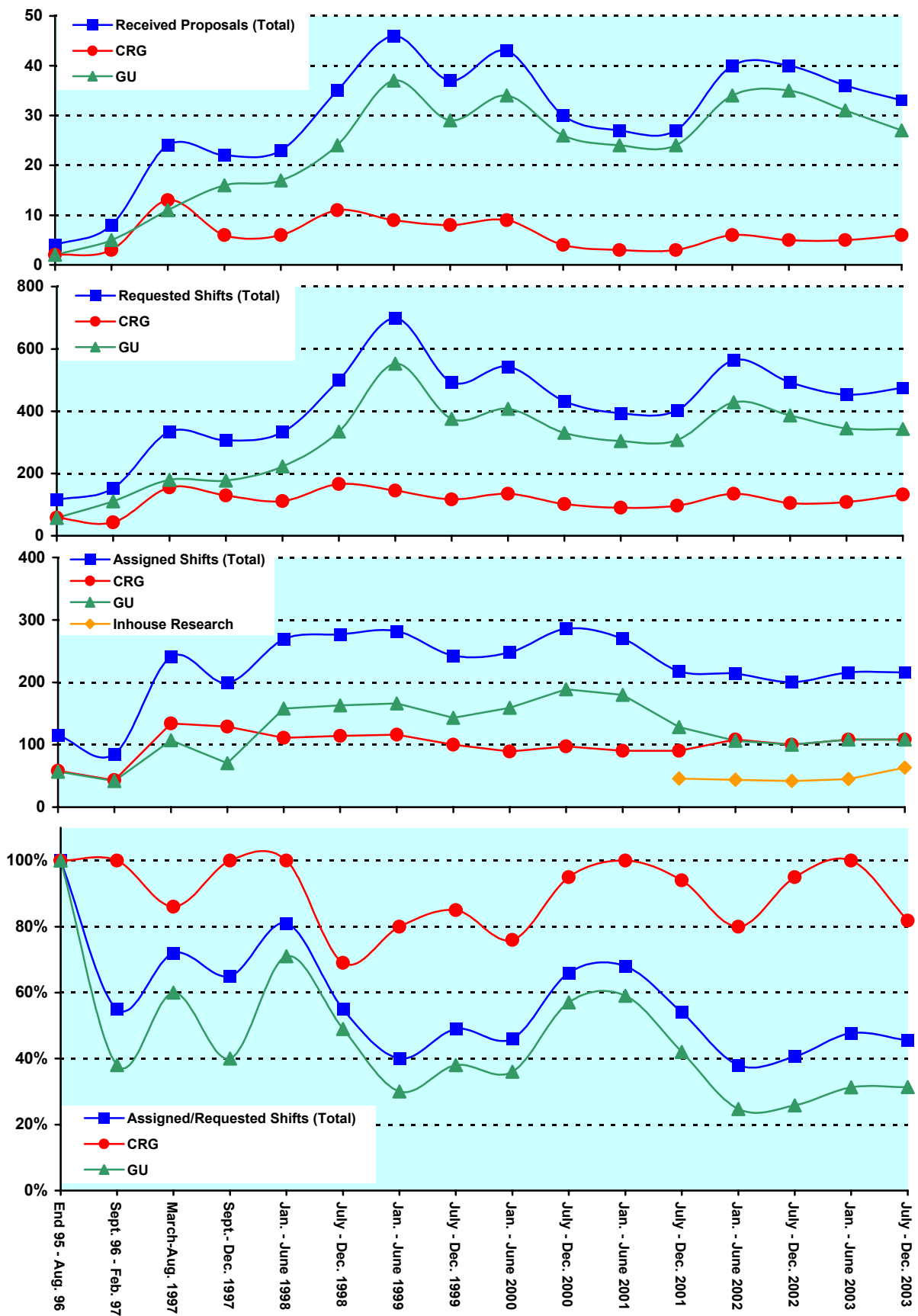
From September 96 on users gained access to the SAXS-beamline on the basis of the proposals received for the periods shown in Fig. 1. The assignment of beamtime at this beamline is done separately for the group of "General Users" (GU) and the "Collaborating Research Group" (CRG), i.e., the Austrian users. Beamtime was assigned to the proposals of each group in the order of the rating received by the Scientific Committee, and up to the maximum number of shifts available to each group according to the contract between "The Austrian Academy of Sciences" and the "Sincrotrone Trieste". Until December 1997 up to 55 % of the beamtime was given to CRG, up to 30 % to GU, and 15% was reserved for maintenance purposes. From January 98 to June 2001 the quota for beamtime was up to 35 % for CRG, up to 50 % for GU, and again 15% reserved for maintenance purposes. From July 2001 on the two contingents for user proposals from CRG and GU receive up to 35% of the beamtime each. The remaining 30 % of beamtime are used for inhouse research projects as well as for maintenance purposes.

Fig. 1 gives an overview of the numbers of received proposals, the numbers of requested and assigned shifts, as well as the percentage between assigned and requested shifts. Included in Fig.1 are also the same data for the period End 1995 - August 1996, during which some beamtime had been given already to users in order to perform first pilot- and test-experiments together with the beamline staff. These first experiments during the commissioning phase were not yet based on proposals, since the goal was mostly to evaluate and improve the performance of the beamline and the equipment of its experimental station. As can be seen in Fig.1, the request for beamtime at the SAXS-beamline increased continuously and strongly until the first half year of 1999 (also during the period Sept.-Dec. 1997, if one takes into account that this period was only 4 instead 6 month long, and that for this reason less proposals were submitted). Then, probably due to the high rejection rates, the number of submitted proposals decreased somewhat during 2001, which resulted in a better ratio of accepted / rejected proposals. This oscillating behaviour of beamtime request can also be seen for the period 2002 - 2003, where again after a high number of submitted proposals a slightly reduced request period followed.

In 2002, in total 80 proposals (11 from CRG, and 69 from GU) were submitted. From these 16 proposals (2 from CRG and 14 from GU) were submitted by "new" usergroups, i.e. groups which so far had never beamtime at the SAXS beamline. From these both CRG and 3 GU proposals were officially accepted, while 3 GU proposals received some shifts for a first „pilot“ experiment.

Figure 1 (Next page). The statistical information about the beamtime periods since end of 1995 are given for the groups "CRG", and "GU" separately, as well as for both together ("Total"). Shown are, for all beamtime periods (from top to bottom):

- Number of received proposals, ● Number of requested shifts,
- Number of assigned shifts, and ● Relation between assigned and requested shifts



2. Provenience of users

During 2002, 161 users from 68 institutes in 16 countries have performed experiments at the SAXS beamline. In Fig. 2 are shown both the provenience of these users, and of their respective institutes. Each user or institute was counted only once, even though many users performed experiments in both beamtime periods of 2002.

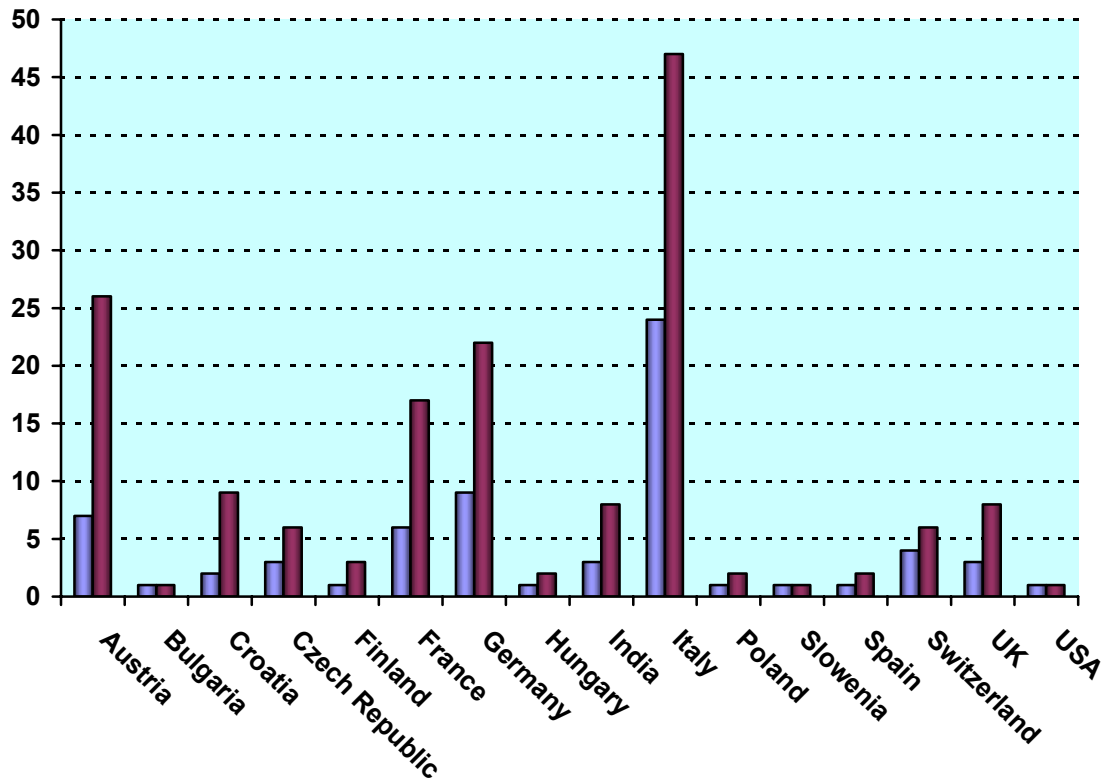


Figure 2. Provenience of users (dark grey) and of their corresponding institutes (light grey).

3. Documentation of experimental results

As could be expected, with the start of user-operation at the SAXS-beamline the number of contributions to conferences started to increase strongly. With a delay of one year - the average time needed for paper publications - also the number of publications increased accordingly, as can be seen in Fig. 3.

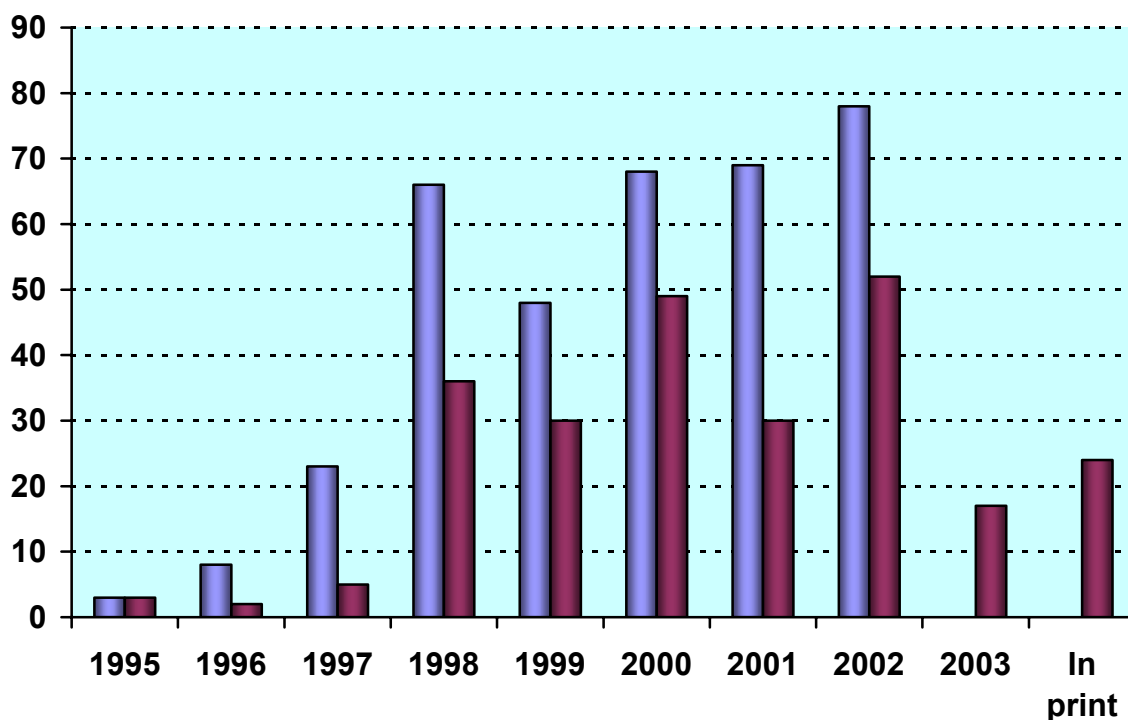


Figure 3. Number of conference contributions (light grey) and of refereed paper publications (dark grey) for the years 1995-2002. Also contributions, which have been published until July 2003 as well as those in print at that time are included.

In addition, from 1995 until July 2003, the following documentations based on instrumentation of the SAXS-beamline, or on data taken with it, have been produced.

Unrefereed publications:

Technical Reports on Instrumentation:	5
Contributions to Elettra Newsletters:	15
Contributions to Elettra Highlights:	16
PhD Thesis:	23
Master Thesis :	16

Furthermore, during 2002 also three SAXS training courses for students have been performed at ELETTRA. These workshops consisted of lectures, "hands-on" experience during experiments at the SAXS beamline or in the new X-ray lab, and data-evaluation on computers (see page 134).

Experimental Possibilities at the SAXS-beamline

1. Latest developments

1. Site laboratories

In August 2002 our new chemistry and X-ray laboratory went into operation. The 70 m² big laboratory is divided in two parts, in which the bigger share of 43 m² is occupied by the chemistry lab. This unit serves mainly for sample preparation and analysis for both, in house research and external SAXS user groups. In the X-ray laboratory the set-up of a SWAX camera for simultaneous small and wide angle scattering has been completed (Hecus-M. Braun, Graz, Austria: www.hecus.at), which allows on-site testing of samples before moving on to the SR beamline. The chemistry lab is meanwhile equipped with:

- micro centrifuge (max. 13200 rpm; model 5415D from Eppendorf, Hamburg, Germany)
- chemical fume hood (model GS8000 from Optolab, Concondordia, Italy)
- vacuum drying oven (min. pressure 1 mbar; max. T: 200 °C; Binder WTB, Tuttlingen, Germany)
- balance (min.-max.: 0.001 - 220 g; model 770 from Kern & Sohn, Balingen, Germany)
- magnetic stirrer with heating plate and a vortexer for microtubes (model MR 3001 and REAX; both from Heidolph, Schwabach, Germany)
- two water baths (the model Unistat CC is freely programmable in range from -30 to 100 °C from Huber, Offenburg, Germany; the model M3 from Lauda can only heat; Lauda-Könighofen, Germany)

Further, two working benches (one with a water sink), two fridges and a separate freezer (- 20 °C), standard glassware, syringes and needles of different sizes, μ -pipettes (10 - 50 - 200 - 1000), as well as some standard solutions (e.g., chloroform, ethanol, methanol) and de-ionized water are available.



Figure 1.
Typical lab activity:
Barbara Sartori loads the
centrifuge (September
2003).

2. Tension cell

Together with the external user group Schulze-Bauer/Holzapfel the research team constructed a general-purpose tension cell. This particular cell was designed for *in-situ* tensile testing with the particular feature that the sample could be completely immersed in a solvent (e.g. physiological solution), which is of particular interest for the blood vessel or collagen fiber testing. The sample container can be attached to a thermal bath to control the temperature in the range from 5 to 95 °C. A screw with an appropriate opening for the passage of the X-ray beam can adjust the optical thickness of the sample container continuously and optimize the set-up for different sample geometries.

The fully remote controlled system allows to control not only the fiber extension from 0 to 50 mm, but also it records simultaneously the force signal in the range from 0 to 25 N and as an option the optically determined Video extensometer signal to measure the transversal contraction of the sample. The complete system is shown in Fig. 2.

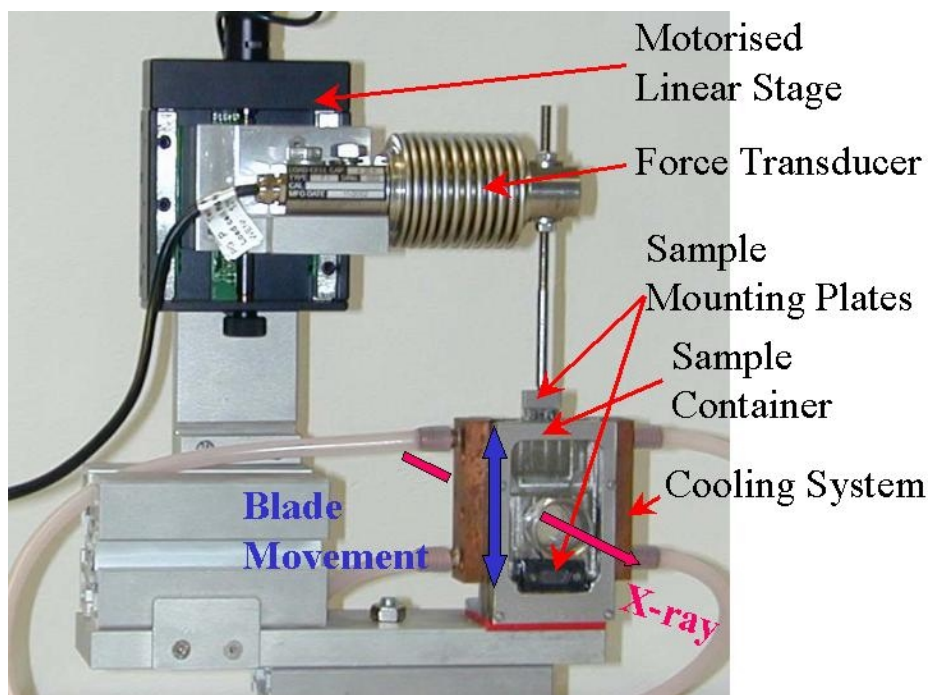


Figure 2. Photograph of the stretcher with cooling system and sample compartment.

2. Accessible SAXS and WAXS ranges

Simultaneous SAXS- and WAXS-measurements can be performed using a linear sensitive gas detector (Gabriel type, windows size 8 x 100 mm, active length 86.1 mm with a resolution of 0.135 mm/channel) for the WAXS-range, and either a second linear Gabriel type detector (windows size 10 x 150 mm, active length 134 mm with a resolution of 0.159 mm/channel), or the 2D CCD-system for the SAXS-range. A specially designed vacuum chamber (SWAXS-nose, see Annual Report of 1996/97, p. 32) allows to use both scattering areas below (for SAXS) and above (for WAXS) the direct beam, respectively.

Depending on the photon energy maximum SAXS resolutions of 2000 Å (5.4 keV), 1400 Å (8 keV) or 630 Å (16 keV) are available. The available possible WAXS-ranges are summarised in Table 1. The overall length of the SWAXS-nose in the horizontal direction, measured from the sample position, is 512 mm and the fixed sample to WAXS-detector distance is 324 mm. At the shortest SAXS camera-length an overlap in the d-spacings covered by the SAXS- and WAXS-detectors, respectively, is possible: then, the common regime lies around 9 Å.

Table 1. Possible d-spacing ranges in the WAXS-regime at the SAXS-beamline at ELETTRA. Since the WAXS-detector can be mounted at four different fixed positions on the SWAXS-nose (range 1-4), with the three possible energy choices (5.4, 8 and 16 keV) this results in 12 different d-spacing regimes. In italic the most common choice (8 keV, range 1) is highlighted. This range is suited for experiments, e.g., on lipid-systems and (bio)polymers.

Range	2 θ [deg]	d-spacing (Å)		
		8 keV	5.4 keV	16 keV
1	9.4	<i>9.40</i>	14.03	4.27
	27.6	3.23	4.82	1.47
2	27.4	3.25	4.86	1.48
	45.6	1.99	2.97	0.90
3	45.4	2.00	2.98	0.91
	63.6	1.46	2.18	0.66
4	63.4	1.47	2.19	0.67
	81.6	1.18	1.76	0.54

3. Calibration of the s-axis and flat field correction

At the SAXS beamline various standards are used for the angular (s-scale) calibration of the different detectors:

- rat tail tendon for the SAXS detector - high resolution (rtt*.dat)
- Silver behenate for the SAXS detector – medium and low resolution (agbeh*.dat)
- Para-bromo benzoic acid for the WAXS detector – WAXS range 1 and 2 (pbromo*.dat)
- Combination of Cu, Al foils and Si powder for the WAXS detector – WAXS range 2 and higher

In Fig. 1 a typical diffraction pattern of rat tail tendon is shown, depicting the diffraction orders (from the first to the 14th order) measured with a "high" resolution set-up (2.3 m) and the delay-line gas detector. The d-spacing is assumed to be 650 Å, but this value can vary depending on humidity up to 3%. Thus, the rat tail tendon is often used only to determine the position of the direct beam (zero order), while the absolute calibration is performed using the diffraction pattern of Silver behenate powder. Fig. 2 depicts a diffraction pattern of Silver behenate measured with "medium" resolution set-up (1.0 m) from the first to the 4th order (repeat spacing 58.4 Å) [1].

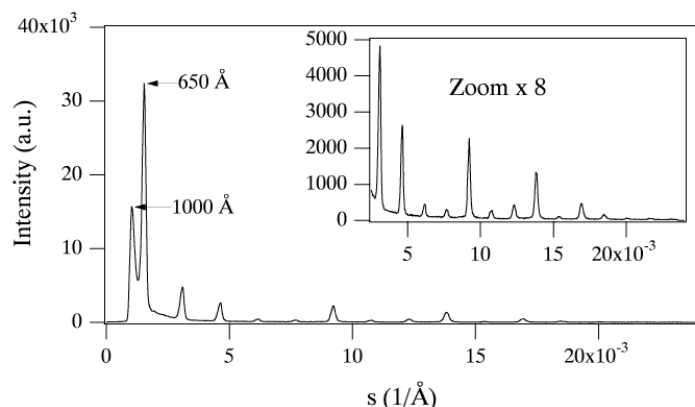


Figure 3. SAXS diffraction pattern of the collagen structure of rat tail tendon fibre at a distance of 2.3 m.

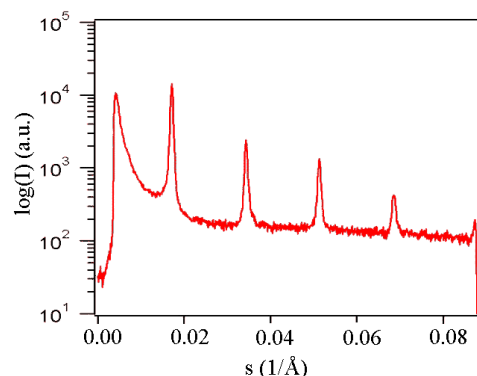


Figure 4. SAXS diffraction pattern of Ag behenate powder at a distance of 1.0 m

In Fig. 3 a typical WAXS pattern of p-bromo benzoic acid is shown. The diffraction peaks are indexed according to the values given in Table 2, taken from [2].

Table 2. d-spacings and relative intensities of p-bromo benzoic acid according to [2].

d-spacing/Å	rel. intensity	d-spacing/Å	rel. intensity
14.72	18000	4.25	490
7.36	1200	3.96	2380
6.02	330	3.84	10300
5.67	980	3.74	26530
5.21	6550	3.68	1740
4.72	26000	3.47	760

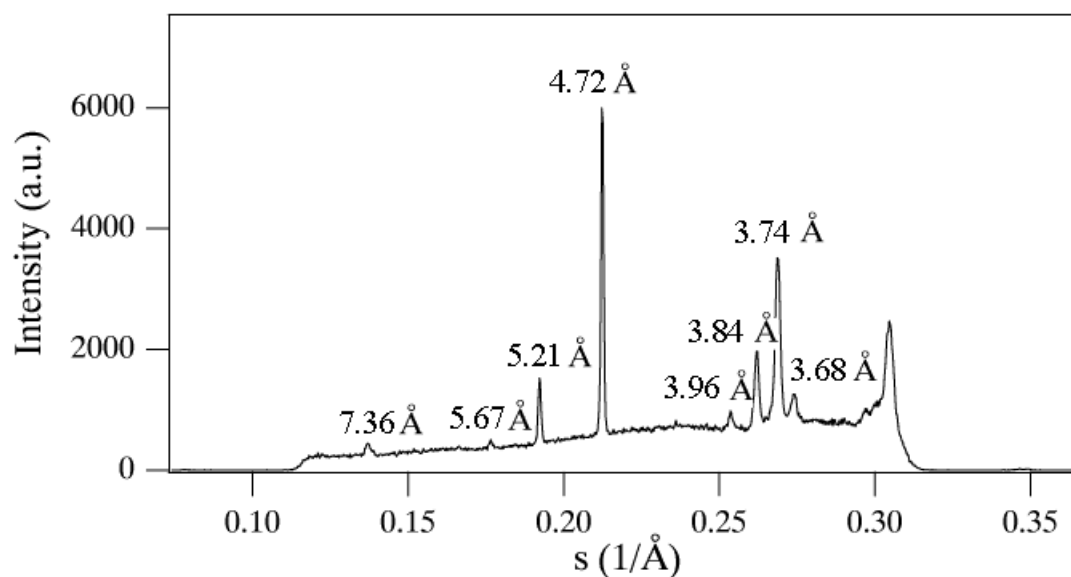


Figure 5. WAXS pattern of p-bromo benzoic acid measured in the WAXS range 1.

The s -scale for both, the SAXS and the WAXS range, can be obtained by linear regression, i.e., the linear relation between the known s -values of the calibrant versus the measured peak positions has to be found.

A further correction is regarding the flat field response (efficiency) of the detectors. For this correction, the fluorescence light of various foils are used to illuminate the detectors rather homogeneously:

- At 8 keV: iron foil (100 μm thick), fluorescence energy: 6.4 keV K_{α} , 7.1 keV K_{β} (effic*.dat)
- At 16 keV: copper foil (> 100 μm thick), fluorescence energy: 8.028 keV $K_{\alpha 2}$, 8.048 keV $K_{\alpha 1}$, 8.905 keV K_{β} (effic*.dat)

The measured scattering pattern are corrected for the detector efficiency simply by dividing them by the fluorescence pattern. Note: The average of the detector efficiency data should be set to unity and a small threshold should be applied to avoid any division by zero.

[1] T.N. Blanton et. al., Powder Diffraction 10, (1995), 91

[2] K. Ohura, S. Kashino, M. Haisa, J. Bull. Chem. Soc. Jpn. 45, (1972), 2651

4. Available sample manipulations stages

1. General

Usually the sample is mounted onto the sample alignment stage which allows the user to place the sample into the beam with a precision of 5 μm (resolution: 1 μm). In Fig. 4 the ranges for vertical and horizontal alignment as well as the maximum dimensions of the sample holders are given. The maximum weight on the sample stage is limited to 10 kg. In case the envelope dimensions of a sophisticated sample station provided by the users are slightly larger than those given in Fig. 4, the user can ask the beamline responsible for a check up of his space requirements. If it does not fit at all to these specifications, user equipment can also be mounted directly onto the optical table, which allows much larger spatial dimensions.

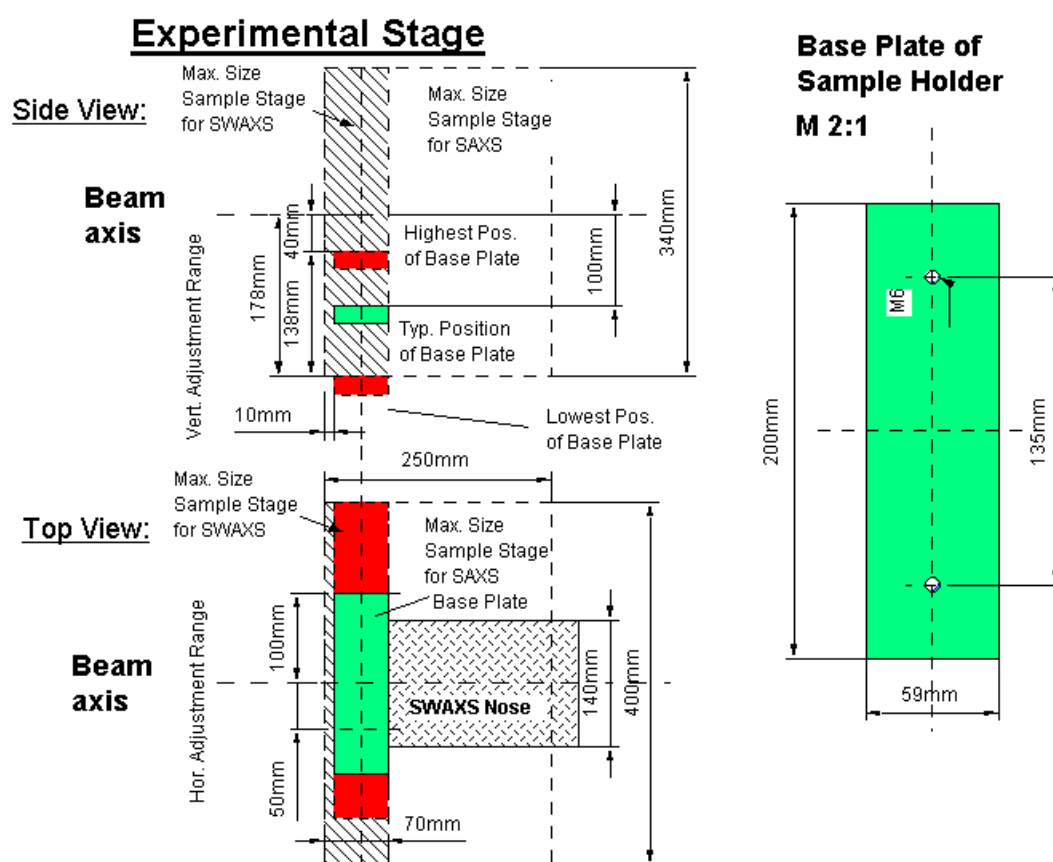


Figure 6. Maximum dimensions and alignment range of the sample holder to be mounted via a base-plate onto the standard alignment stage (left), and dimensions of the base-plate (right).

2. Sample holders

As standard equipment for liquid samples Paar capillaries (diameter: 1 and 2 mm) are used thermostated with the KHR (electrical heating) or KPR (Peltier heating/cooling) sample holders (Anton Paar, Graz, Austria). For use in these sample holders flow through capillaries and Gel holders are standard equipment. Temperature scans can be performed with KHR and/or KPR in the range from 0 to 150 $^{\circ}\text{C}$, typically the precision and the stability of this systems is < 0.1 $^{\circ}\text{C}$. Additionally thermostats for temperature control or cooling proposes can

be used at the beamline (0-95 °C, at present). Helium and Nitrogen gas bottles are available at the beamline, for other gases please contact the beamline responsible.

Multiple-sample holders can be mounted onto the standard sample manipulator. At present holders are available for measuring in automatic mode up to 30 solid samples at ambient temperature or up to 4 liquid or gel samples in the temperature range 0 – 95 °C.

3. Online exhaust system

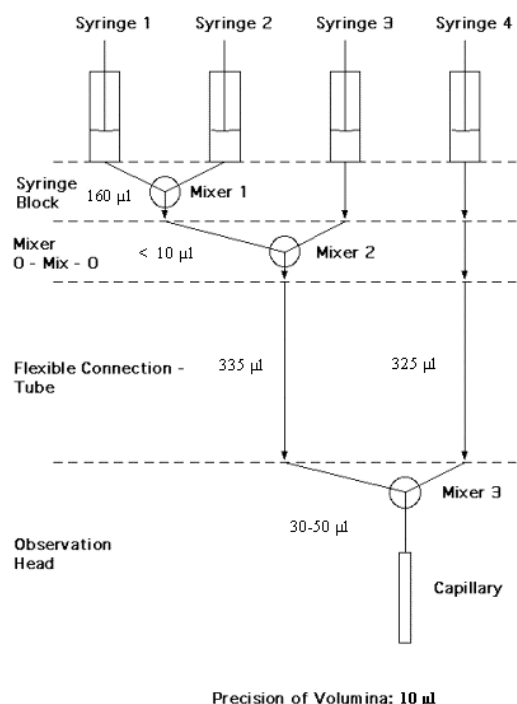
At the experimental station is available a custom-built fume cover and chemical exhaust system for toxic gases. Thus it is possible to e.g. study in-situ chemical reactions, during which toxic gases might develop.

4. Magnet System

For studying magnetic effects in samples, capillaries or sample holders with suitable dimensions can be mounted inside an electromagnet. Up to now a sample holder for standard Paar capillaries (Anton Paar, Graz, Austria) is available for ambient temperature only. The alignment of the magnetic field is horizontal or vertical (transversal to the photon beam). For short times the maximum magnetic field can be up to 1.5 T, and 1.0 T for continuous operation, respectively, assuming a pole gap of 10 mm for both.

5. Stopped Flow Apparatus

A commercial stopped flow apparatus (manufactured by Bio-Logic, Paris, France), especially designed for Synchrotron Radiation SAXS investigations of conformation changes of proteins, nucleic acids and macromolecules, is available. The instrument consists of a 4 syringe cell with 3 mixer modules manufactured by Bio-Logic. Each syringe is driven independently from the others by an individual stepping-motor, which allows a high versatility of the mixing sequence (flow-rate, flow duration, sequential mixing). For example, injection sequences using one or up to 4 syringes, unequal filling of syringes, variable mixing ratio, reaction intermediate ageing in three- or four-syringe mode etc.. The solution flow can be entirely software-controlled via stepping motors, and can stop in a fraction of a millisecond.



The software allows the set-up of the shot volumes of each of the 4 syringes in a certain time interval. Up to 20 mixing protocols can be programmed. Additionally macros for the repeated execution of individual frames can be defined. Furthermore, the input and output trigger accessible for user operation can be programmed. In the usual operation modus the start of rapid mixing sequence is triggered from our X-ray data-acquisition system (input trigger).

After the liquids have been rapidly mixed, they are filled within few ms into a 1 mm quartz capillary - situated in the X-ray beam- , which is thermostated with a water bath. Depending on the diffraction power of the sample time resolutions of up to 10 ms can be obtained.

Figure 7. Sketch of the stop flow system.

The main parameter of the system are:

- Thermostated quartz capillary (1 mm)
- Temperature stability 0.1 °C
- Total sample used per mixing cycle (shot volume): 100 µl
- Maximum 2θ angle of 45°
- Total Volume 8 ml
- Dead volume 550 µl
- Speed: 0.045 – 6 ml/s
- Duration of flow 1 ms to 9999 ms/Phase
- Dead time: 1 ms
- Reservoir volume: 10 ml each

Further information can be found in the homepage: <http://www.bio-logic.fr/>

6. Grazing Incidence Small Angle X-ray Scattering

Grazing incidence studies on solid samples, thin film samples or Langmuir-Blodgett-films can be performed using a specially designed sample holder, which can be rotated around 2 axes transversal to the beam. Furthermore the sample can be aligned by translating it in both directions transversal to the beam. The precisions are 0.001 deg for the rotations and 5 µm for the translations. Usually the system is set to reflect the beam in the vertical direction. According to the required protocol and the actual assembly of the rotation stages ω , θ , 2θ and φ scans can be performed.

7. Temperature Gradient Cell

A temperature gradient cell for X-ray scattering investigations on the thermal behaviour of soft matter manybody-systems, such as in gels, dispersions and solutions, has been developed. Depending on the adjustment of the temperature gradient in the sample, on the focus size of the X-ray beam and on the translational scanning precision an averaged thermal resolution of a few thousands of a degree can be achieved.

8. IR-Laser T-Jump System for Time-Resolved X-ray Scattering on Aqueous Solutions and Dispersions.

The Erbium-Glass Laser available at the SAXS-beamline (Dr. Rapp Optoelektronik, Hamburg, Germany) delivers a maximum of 4 J per 2ms pulse with a wavelength of $1.54 \mu\text{m}$ onto the sample. The laser-beam is guided by one prism onto the sample, which is filled in a glass capillary (1 or 2 mm in diameter) and Peltier or electronically thermostated in a metal sample holder (A. Paar, Graz, Austria). With a laser spotsize of maximal 7 mm in diameter a sample-volume of maximal $5.5 \mu\text{l}$ or $22 \mu\text{l}$, respectively, is exposed to the laser-radiation. In a water-solutions/dispersions with an absorption coefficient of $A = 6.5 \text{ cm}^{-1}$ T-jumps up to $20 \text{ }^\circ\text{C}$ are possible.

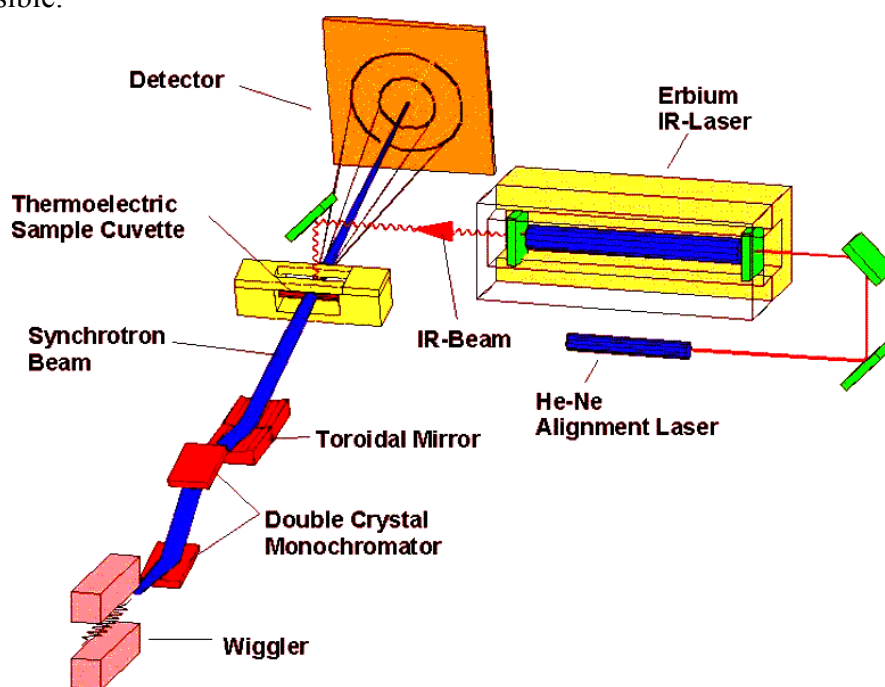


Figure 8. Sketch of the T-jump set-up.

9. High Pressure Cell System

SWAXS measurements of samples under pressure can be performed from 1 to 2500 bar, from 0 to $80 \text{ }^\circ\text{C}$ in the scattering angle region up to 30 degrees, both in the static or time-resolved mode, e.g. p-jump or p-scan, with a time-resolution down to the ms range. Precise pressure scans of any speed within a broad range (e.g. ca. 1.0 bar/s - 50 bar/s in the case of water as pressurising medium, and a typical sample volume) can be performed. Alternatively, dynamic processes can be studied in pressure-jump relaxation experiments with jump amplitudes up to 2.5 kbar/10ms in both directions (pressurising and depressurising jumps).

In most applications diamond windows of 0.75 mm thickness (each) are used. The transmission of one pair (entrance and exit window) is 0.1 at 8 keV, i.e. lower than 0.3, the value for the originally used 1.5 mm thick Be-windows. However the loss in intensity is more than compensated for by the considerably lower background scattering of diamond thus leading to higher q-resolution in the experiments.

The sample thickness can be 0.6-4.0 mm, with a volume of approximately 0.5-3 mm³ completely irradiated by pin-hole collimated (< 1.0 mm diameter) X-rays.

The pressure cell system is flexible and can be built according to the needs of the particular experiment. Normally, a liquid (water, ethanol or octanol) is used as pressurising medium. But in principle, also gaseous media can be employed as well. N₂ has been successfully tested, and measurements in supercritical CO₂ became frequent.

Beside bulk measurements on samples in transmission set-up, also grazing incidence experiments using silicon wafer with highly aligned samples on its surface inserted in the high-pressure cell have been carried out successfully.

10. Oxford Cryostream Cooler

The Cryostream cooler creates a cold environment only a few millimeters from the nozzle position. The temperature and the flow of the nitrogen gas stream is controlled and regulated by a Programmable Temperatur Controller based on an 'in stream' heater and a thermo-sensor before it passes out over the sample.

The system has been especially developed for X-ray crystallography to perform diffraction experiments on e.g. shock frozen bio-crystals. However, the programmable temperature controller allows further implication for SAXS-experiments, e.g., rapid temperature drops in solvents. The design of the Cryostream Cooler facilitates:

- nitrogen stream temperatures from -190 to 100 °C,
- a stability of 0.1 °C,
- a system that can be refilled without creating any disturbance of the temperature at the sample,
- temperature ramps can easily be carried out remotely controlled with scan rates up to 6 °C/min
- individual temperature protocols can be cycled
- T-jumps in both directions can be performed by rapid transfer of the sample in a pre-cooled or -heated capillary using a fast syringe driver reaching a minimum temperature of -80 °C. Here, typical scan rates are about 15 °C/sec with a total process time in the order of 10 sec.

11. In-line Differential Scanning Calorimeter (DSC)

The in-line micro-calorimeter built by the group of Michel Ollivon (CNRS, Paris, France) allows to take simultaneously time-resolved synchrotron X-ray Diffraction as a function of the Temperature (XRDT) and high sensitivity DSC from the same sample.

The microcalorimetry and XRDT scans can be performed at any heating rate comprised between 0.1 and 10 °C/min with a 0.01 °C temperature resolution in the range -30/+130 °C. However, maximum cooling rates are T dependent and 10°C/min rates cannot be sustained below 30°C since cooling efficiency is a temperature dependent process. Microcalorimetry

scans can be recorded independently, and also simultaneously, of X-ray patterns. The microcalorimeter head can also be used as a temperature controlled sample-holder for X-ray measurements while not recording a microcalorimetry signal. Isothermal microcalorimetry is also possible when a time dependent thermal event such as meta-stable state relaxation or self-evolving reaction, is expected. The sample capillaries have a diameter of 1.5 mm and are filled over a length of 10 mm.

12. The 2D CCD-camera system

The CCD has a 115 mm diameter input phosphor screen made of a gadolinium oxysulphide polycrystalline layer. The screen is coupled by means of a fiber optic to the image intensifier. The image intensifier is coupled again with an additional taper to the CCD itself. The achieved spatial resolution of a pixel is 79 μm for the whole set-up.

The number of pixels is 1024 x 1024 and they can be pinned down to 2 x 2 and 4 x 4. The dynamic range of the CCD is 12 bit. The dark current of the CCD is in the order of 100 ADU (off-set) and the readout noise (read out speed: 10 MHz) is in the order of 6 ADU. (The CCD is cooled by multistage Peltier element for reducing the dark noise.) The intensifier gain is adjustable between 200 and 20000 photons full dynamic range. Typical readout times and exposure times are 150 ms and 100 ms, respectively. The readout times can be reduced down to 100 ms by using the pinning mode of the CCD. Between the frames additional wait times can be programmed e.g. for reducing the radiation damage in the sample or to extend the time for measuring long time processes.

For the external control a TTL trigger signal is provided (active low, when the CCD is accumulating an image), which is used to control the electromagnetic fast shutter of the beamline on one hand. On the other hand this signal can be used also to trigger processes as requested by the user.

The CCD is controlled by Image Pro+, which also includes non too sophisticated data treatment capabilities. The program is featuring a comprehensive set of functions, including:

- flat fielding/background corrections
- enhanced filters and FFT
- calibration utilities (spatial and intensity)
- segmentation and thresholding
- arithmetic logic operations
- various measurements, like surface, intensity, counts, profiles
- advanced macro management

The data are stored in 12 bit – TIFF format. At the present state up to 300 full images (1024 x 1024) can be recorded by the system, but a strict conservation of the timing sequence is maintained only for the first 15 - 17 frames until the RAM memory is full. Afterwards the images are stored in the virtual memory on the hard disk. At present a software development for the CCD readout system is under way to improve the stability of the readout cycles.

For the complete treatment of the 2D data Fit2D available from the ESRF is used, which is able to perform both interactive and "batch" data processing (homepage: http://www.esrf.fr/computing/expg/subgroups/data_analysis/FIT2D/index.html, programmed by Dr. Andy Hammersley), which supports a complete spatial correction, flat field correction and background correction. Furthermore more elevated data-treatment can be performed within this software package, like circular integration, segment integration and similar.

User Contributions

1. Materials Science

GISAXS STUDIES OF ORDERING IN CdSe/ZnSSe QUANTUM DOT STACKS

G. Alexe¹, Th. Schmidt¹, T. Clausen¹, S. Bernstorff², T. Passow^{1,3}, D. Hommel¹ and J. Falta¹

1.) Institut für Festkörperphysik Universität Bremen, P.O.Box 330440, 28334 Bremen, Germany

2.) ELETTRA, Strada Statale 14, 34012 Basovizza, Italy

3.) Present address: Institut für Angewandte Physik Universität Karlsruhe, Kaiserstraße 12, 76128 Karlsruhe, Germany

The system CdSe/ZnSe has attracted much interest because of the possible application to opto-electronic devices working in the blue/green/yellow spectral range. Especially the self-assembled formation of CdSe/ZnSe quantum dots due to the high lattice mismatch [1] and the quantum dot structures [2] have been widely studied motivated by the perspective of incorporating quantum dot structures in laser diodes. Recently the first quantum dot laser operation has been realized in this system [3].

For the systematic study of the ordering of CdSe quantum dots we have chosen two series of CdSe quantum dot stacks in ZnSSe which were grown in a molecular beam epitaxy system on GaAs(001) substrates. The substrate temperature was 280°C. 1.8 monolayers CdSe were deposited for each quantum dot sheet using migration enhanced epitaxy. The first series consists of three samples with an increasing number of 3, 5 and 10 quantum dot sheets in the stacks separated by 4.2 nm thick ZnSSe spacer layers (samples A-C). The second series consists in three samples with fivefold stacks with varying spacer layer thickness of 2, 4.5 and 8 nm ZnSSe, respectively (samples D-F).

Grazing incidence small angle x-ray scattering (GISAXS) experiments were performed at the SAXS beamline at various incidence angles in order to characterize the lateral and vertical ordering of the quantum dots and determine the corresponding correlation parameters. We were able to identify satellite spots in the small angle scattering signal which we attribute to the presence of a vertical and lateral correlation of the quantum dots for samples B, C, D and E, but not for samples A and F. The experimental results are summarized in Fig. 1.

An ordering of the CdSe quantum dots due to stacking indeed occurs, as shown by the appearance of satellite spots in Fig. 1 (C-E). These are a clear indication of correlations in position of quantum dots. The corresponding data sets for samples A and F show no indication of satellite spots. The mechanisms of ordering of stacked quantum dot layers are linked to strain fields which modify the lateral nucleation probability for subsequently deposited quantum dot layers [4]. Crystal anisotropy has also been shown to play a mayor role for the order of stacking [5].

From this qualitative analysis we can conclude that for the sample with a 8 nm thick spacer layer (F) the vertical correlation of quantum dots in subsequent layers is too weak to allow for a lateral ordering of the dots. For thicker spacer layers, the intrinsic changes of the nucleation probability due to growth related parameters and statistics become dominant and no ordering is observed therefore. For the threefold stack sample (A) the spacer layer thickness is identical to samples B and C for which ordering could be detected. Therefore it must be considered that the number of quantum dot sheets is not sufficient to allow ordering to be established. However, further experiments are needed to elucidate this issue.

The material system of CdSe/ZnSSe is very sensitive to accumulated strain which leads to the formation of stacking faults [2,6]. Their influence on the strain fields will decrease the order with increasing number of layers in the stack. However, strain compensation by the use of ZnSSe spacer layers overcomes this problem, as seen from comparing the intensity of the satellite peaks for sample E and sample C. Clearly, sample C shows even better ordering than sample E(B) indicating that strain compensation leads to enhancement of the active volume fraction available for light emission in devices.

A first quantitative analysis of the CCD data yields a lateral correlation length of the dot-dot distance of 14.5 nm for sample E. This value is compatible with corresponding TEM and PL data [7]. We have measured x-ray reflectivity scans on samples B, D, E, and F. The analysis of these is expected to allow the correlation of the GISAXS results with the vertical structure and interface quality of the samples.

In summary, using GISAXS we were able to identify and quantify ordering of stacked CdSe quantum dot arrays. Our preliminary data analysis shows that ordering is only possible for thin spacer layers with a thickness below 5 nm. The results point towards an optimum number of stacks for given compositions of the quantum dot array and the spacer layers.

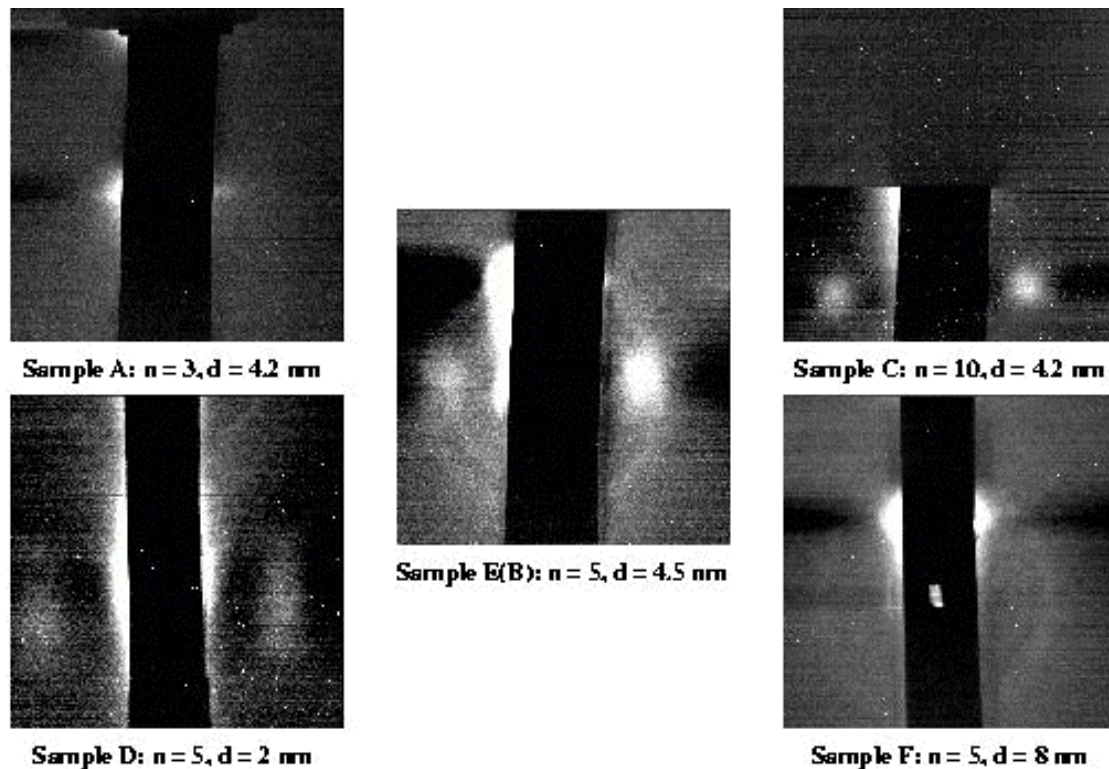


Figure 1. GISAXS data obtained for samples A, C, D, E, F as described above (n is the number of quantum dot sheets in the stack and d is the thickness of the ZnSSe spacer layer).

References:

- [1] T. Passow, K. Leonardi, H. Heinke, D. Hommel, D. Litvinov, A. Rosenauer, D. Gerthsen, J. Seufert, G. Bacher, and A. Forchel; Quantum dot formation by segregation enhanced CdSe reorganization; *J. Appl. Phys.* **92**, 6546-6552 (2002)
- [2] T. Passow, K. Leonardi, and D. Hommel; Optical and structural properties of CdSe/Zn(S)Se quantum dot stacks; *phys. stat. sol. (b)* **224**, 143-146 (2001)
- [3] M. Klude, T. Passow, R. Kröger, and D. Hommel; Electrically pumped lasing from CdSe quantum dots; *Electron. Lett.* **37**, 1119-1120 (2001)
- [4] J. Tersoff, C. Teichert, and M.G. Lagally; Self-organization in growth of quantum dot superlattices; *Phys. Rev. Lett.* **76**, 1675-1678 (1996)
- [5] V. Holý, G. Springholz, M. Pinczolit, and G. Bauer; Strain induced vertical and lateral correlations in quantum dot superlattices; *Phys. Rev. Lett.* **83**, 356-359 (1999)
- [6] R. Engelhardt, U.W. Pohl, D. Bimberg, D. Litvinov, A. Rosenauer, and D. Gerthsen; Room-temperature lasing of strain-compensated CdSe/ZnSSe quantum island laser structures; *J. Appl. Phys.* **86**, 5578-5583 (1999)
- [7] T. Kümmell, R. Weigand, G. Bacher, A. Forchel, K. Leonardi, D. Hommel, and H. Selke; Single zero-dimensional excitons in CdSe/ZnSe nanostructures; *Appl. Phys. Lett.* **73**, 3105-3107 (1997)

FIBER DIFFRACTION STUDY OF SPICULES FROM MARINE SPONGES

H. Amenitsch¹, G. Bavestrello², U. Benatti³, G. Croce⁴, A. Frache⁴, M. Giovine⁵, L. Marchese⁴, M. Milanese⁴, D. Viterbo⁴

- 1.) Institute of Biophysics and X-Ray Structure Research, Austrian Academy of Science, Schmiedlstr. 6, A-8043 Graz, Austria.
- 2.) Ist. Scienza del Mare, Università di Ancona, V. Breccie Bianche – Monte Dago, I-60100 Ancona, Italy
- 3.) DIMES sez. Biochimica, Università di Genova, V. L.B. Alberti 2, I-16132 Genova, Italy
- 4.) DISTA, Università del Piemonte Orientale “A. Avogadro”, C.so T. Borsalino 54, I-15100 Alessandria, Italy
- 5.) CNR, direzione progetto finalizzato biotecnologie, Via L.B. Alberti 4, I-16132 Genova, Italy

Silicon, the second most abundant element in the Earth's crust, is also present in a wide variety of living organisms [1] and is required for the production of structural materials. The biological formation of amorphous hydrated silica is called *biosilicification* [2, 3]. Some families of sponges have also been found to contain silica as all or part of their skeleton. Indeed siliceous sponges deposit hydrated silica in needle-like spicules. Siliceous spicules contain an organic axial filament [4, 5], generally made of proteins called *silicateins* [6] (for SILICA proTEINS), around which hydrated silica is deposited. The precise involvement in the process is largely unknown.

The aim of our fiber diffraction work is the structural study of the axial filaments of spicules from different sponges in order to achieve a more realistic picture of their organization. We carried out SAXS measurements on four species of spicules belonging to two different families: the three Demosponges *Geodia cydonium*, *Tethya aurantium*, *Petrosia ficiformis* and the Hexactinellid *Scolymastra joubini*. The analyzed samples present a sufficient length of some mm to be oriented inside a boron-glass capillary. This allowed the collection of fiber diffractograms from a still sample composed by a bundle of almost parallel spicules. Single spicules were also mounted on a sample holder to perform fiber diffraction experiments. This allowed the collection of fiber diffractograms during the rotation of the samples along its main axis.

The sharp diffraction spots, for all samples analysed, indicated a high degree of order in the organisation of the filaments. These kind of measurements suggested also some degree of order along the fibre axes. The protein units appear to be packed in a compact hexagonal way and from the position and distribution of the spots it is possible to derive some structural parameters. The different number and disposition of diffraction spots obtained from different samples indicates that the degree of order varies from species to species.

For example, the demosponge *G. cydonium* gives three spots along the vertical equatorial axis and the diffraction angle of the first spot corresponds to a d-spacing of about 5.0nm. This pattern is related to a regular 2D lattice of protein units in the direction perpendicular to the spicule axis, with the units linked to form fibers along the axis (Figure 1), in agreement with the TEM evidences given by Garrone [7]. Even though the derivation of a possible unit cell from just three diffraction spots might be questionable, the values of the d-spacing of the observed spots are consistent with the plausible hexagonal lattice shown in Figure 2 with a cell edge a of about 5.8nm, a value close to that estimated by Garrone [7] for *Haliclona rosea*. A similar structural organization, giving rise to a similar diffraction pattern, was hypothesized for some mesoporous molecular sieves [8].

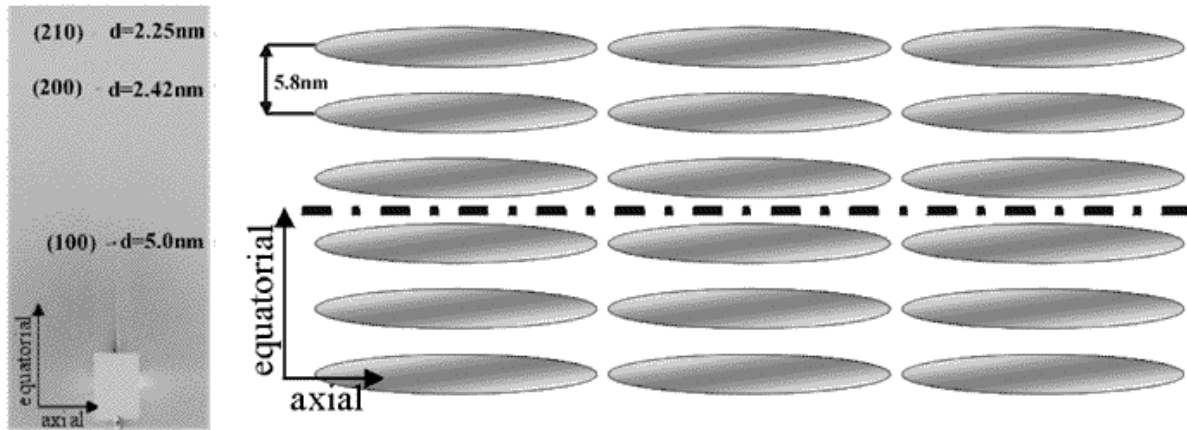


Figure 1. X-ray diffraction pattern and structural model of the organization of the filaments in the *G. cydonium* spicules.

The hexactinellid *S. joubini* sample gives four non-equatorial spots all with the same d-spacing of about 7.3nm and rotated of about $\Phi = 50^\circ$ with respect to the horizontal polar axis (Figure 2). No higher order spots are observed. This pattern indicates the presence of two different 2D lattices in which the repeating protein units are inclined of $+\Phi$ and $-\Phi$ respectively with respect to the elongation axis, as shown in Figure 3. If we also in this case assume a hexagonal lattice, the distance between the units becomes $a = 8.4\text{nm}$.

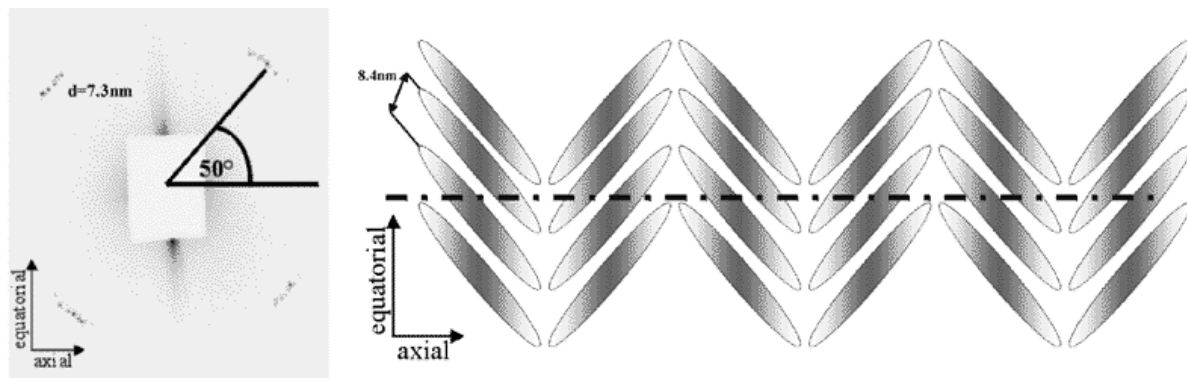


Figure 2. X-ray diffraction pattern and structural model of the organization of the filaments in the *S. joubini* spicules.

The series of diffraction diagrams, recorded every 1° while a single spicule of *S. joubini* was rotated by 180° , with its axis normal to the X-ray beam, shows that the pattern with 4 non-equatorial spots (Figure 3), similar to that of Figure 2, is only recorded at discrete angular ranges (approximately 10° wide) separated by about 60° . When the single spicule is tilted by 10° with respect to the incoming beam, the discrete ranges become wider ($\sim 21^\circ$) and are constituted by 2-3 images with two diagonally opposed spots, followed by a number of blank images and ended with 2-3 images with two spots on the other diagonal. With the spicule tilted by 5° and 20° similar patterns are obtained. A 3D model of the arrangement of the protein units in the spicule filaments, consistent with these single-spicule diffraction patterns and with the 2D model of Figure 2, can be hypothesized. This model consists of a hexagonal packing of spirally oriented cylindrical protein units, elongated along the filament axis (Figure 3)[9].

The analysis and interpretation of the more complex diffraction patterns from the demonsponges *T.aurantium* and *P.ficiformis* is still in progress.

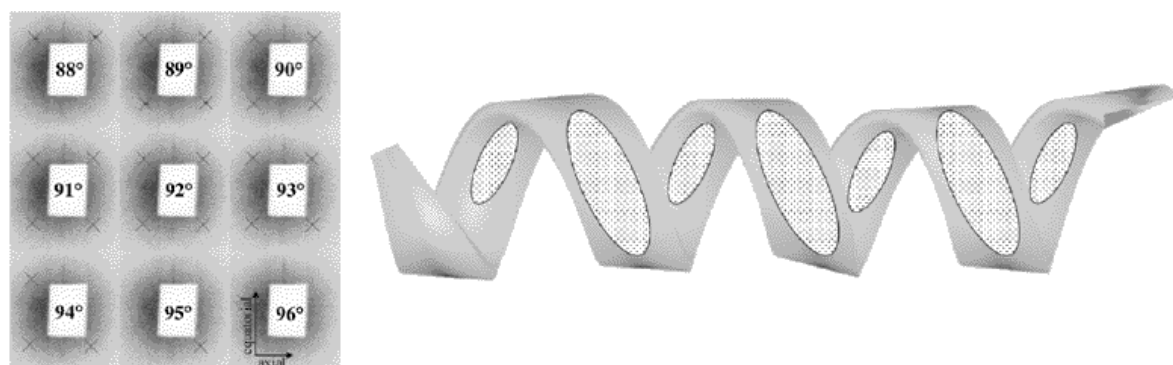


Figure 3. Sequence of 9 diffraction patterns of a single spicule of *S. joubini* taken every 1° of rotation with its axis normal to the X-ray beam. Model of *S. joubini* filament, formed by spirally oriented protein units elongated along the filament axis.

On the basis of our findings, we can finally suggest the following possible mechanism for the biosilification process in spicules. In the initial step silicatein units act as template for the formation of a highly organized structure similar to that in mesoporous materials. In a second step the biosilification process should continue with a deposition of amorphous silica on the outer walls of the mesoporous filament.

References:

- [1] Simpson, T.L. & Volcani, B.E.; *Silicon and Siliceous Structures in Biological Systems*, Springer, New York (1981).
- [2] Voronkov, M.G., Zelchan, G.I. & Lukevits, E.J.; *Silicon and Life*, Zinatne, Riga, 2nd ed (1977).
- [3] Bendz, G. & Lindqvist, I; *Biochemistry of Silicon and Related Problems*, Plenum Press, New York (1977).
- [4] Perry, C. C., Keeling-Tucker, T. J.; Biosilicification: the role of the organic matrix in structure control, *Biol. Inorg. Chem.*; **5**, p. 537-550, (2000).
- [5] Garrone, E.; *Phylogenesis of Connective Tissue*, Karger, Basel, pp. 176-179, (1978).
- [6] Shimizu, K., Cha, J., Stucky, G.D., Morse, D.E.; Silicatein α : Cathepsin L-like protein in sponge biosilica *Proc.Natl. Acad. Sci. USA*; **95**, pp. 6234-6238, (1998).
- [7] Garrone R., Collagène, spongine et squallette minéral chez l'éponge *Haliclona rosea* (O.S.) (Démospone, Haploscléride). *J. Microsc.* ; **8**, 581-598, (1969).
- [8] Grosso D, Babonneau F, Klotz M, Albouy P-A, Amenitsch H, Balkenende AR, Brunet-Bruneau A, Rivory J. An in situ study of mesostructured CYAB-silica film formation during dip coating using time-resolved SAXS and interferometry measurements. *Chem. Mater.*; **14**, 931-939, (2002).
- [9] Kakudo M, Kasai N. X-Ray Diffraction by Polymers. Amsterdam: Elsevier Publishing Co. pp. 421-424 (1972).

GISAXS STUDIES OF SIZE DISTRIBUTION OF CdS NANOCRYSTALS FORMED IN SiO₂ BY ION IMPLANTATION

U. V. Desnica¹, P. Dubcek¹, I.D. Desnica-Frankovic¹, M. Buljan¹, K. Salamon², O. Milat², S. Bernstorff³, and C.W. White⁴

- 1.) R. Boskovic Institute, Bijenicka 54, 10000 Zagreb, Croatia
 2.) Physics Institute, Bijenicka 58, 10000 Zagreb, Croatia
 3.) Sincrotrone Trieste, SS 14 km163,5, 34012 Basovizza, Italy
 4.) Oak Ridge National Laboratory, P.O.Box 2008, Oak Ridge T 37831, USA

There is an intense research activity going on to develop technology for an efficient and controllable synthesis of nanocrystals or quantum dots (QDs) [1-3]. This interest is mainly due to the strong modification of electronic, optical and other properties of QDs with respect to the corresponding bulk materials, offering a number of potential applications in semiconductor and other industries [1]. Grazing incidence small angle X-ray scattering (GISAXS) was applied to study the synthesis and size evolution of CdS nanocrystals. CdS was formed in SiO₂ substrate by successive multi-energy implantation of constituent elements (three different ion doses) and subsequent thermal annealing ($T_a = 800^\circ$ or 1000°C). The well-resolved GISAXS spectra (Fig. 1) from CdS nanoparticles were obtained for all samples, proving the successful synthesis of CdS QDs for all doses and annealing temperatures.

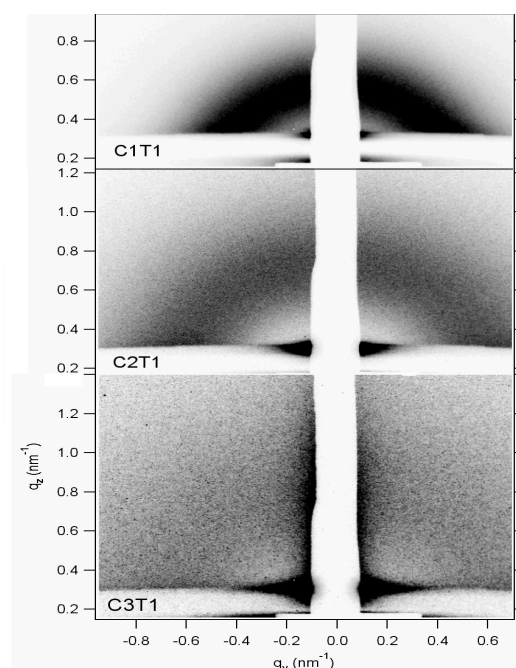


Figure 1. 2D GISAXS spectra of CdS in SiO₂, obtained by implantation of constituent atoms and subsequent annealing at $T_1 = 1000^\circ\text{C}$, for the concentration of implanted Cd and S atoms: a) $C_1 = 5.3 \times 10^{21} / \text{cm}^3$ b) $C_2 = 2.0 \times 10^{21} / \text{cm}^3$ c) $C_3 = 0.8 \times 10^{21} / \text{cm}^3$.

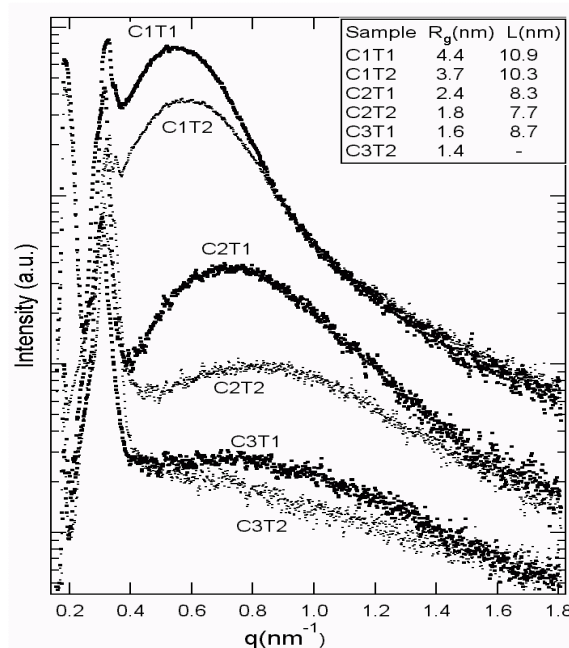


Figure 2. Specular scans, offset for the beam-stopper width, of 2D GISAXS spectra for 3 doses, C_i , and two annealing temperatures, T_i . Sample T1C1 denotes sample implanted to C1 and annealed at $T_1 = 1000^\circ\text{C}$, etc. Insets show numerical data for the Guinier radius R_g and the average inter-cluster distance L.

The analysis of 2D GISAXS patterns with the Guinier plot (Fig. 2) was compared to the fit results of the local mono-disperse approximation (LMA), (Fig.3). In LMA approximation, it is assumed that the positions and the sizes of particles are completely correlated. The model assumes that a hard sphere includes the ‘precipitate’ of diameter D plus surrounding a depleted zone with no other precipitates.

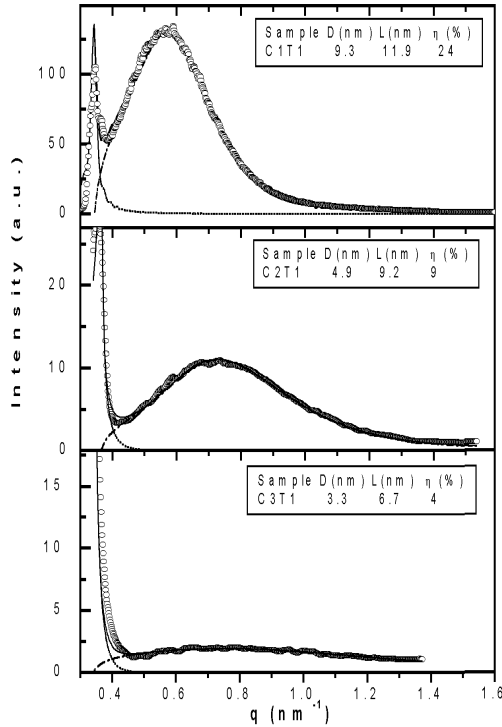


Figure 3. 1D GISAXS pattern (open circles) of three samples implanted with doses C1, C2 and C3 and annealed at T1=1000°C. The solid line is the best fit of the local monodisperse approximation, dash-dot-dash line represents CdS nanocrystal contribution, and dotted line surface effects contribution. Insets show numerical data for average diameter D, average inter-cluster distance L, and CdS volume fraction η , obtained from the best fits.

Both the Guinier and the LMA approximations give similar values for L as well as for D, if one assumes the relation $D = 2R_g$ [4]. Results indicate that the selected applied implantation+annealing procedure resulted in the formation of isolated, spherical CdS nanoparticles embedded in SiO₂ amorphous matrix, evenly distributed in the substrate in all three dimensions, where QDs

diameter and interparticle distance varied with implantation and post-implantation parameters.

The nanoparticle average size, size distribution, inter-particle distance and fraction of synthesized atoms were determined for each ion dose and selected T_a. The presented GISAXS results were compared with high-resolution TEM results. For T_a = 1000 °C the TEM-determined D_{TEM} were 9.8 nm, 6.5 and 4.9 nm, respectively [3]. Considering all the differences between GISAXS and TEM techniques, in particular that GISAXS averages over a large part of the sample surface, while TEM probes very locally, giving the projected area of buried clusters, the agreement for D is reasonably good, particularly for larger doses.

The LMA-calculated values for FWHM (w = 6.5 nm, 4 nm and 2.7 nm, for C1, C2 and C3, respectively) agree very well with the ones estimated from TEM distributions [3].

Furthermore, for all 3 doses the LMA values for the CdS volume fraction in SiO₂, η , (Fig. 3) are in very good agreement with values calculated under the assumption that virtually all implanted Cd and S atoms are indeed synthesized into CdS after 1000°C annealing. All these results promote GISAXS as an excellent and nondestructive tool to investigate the role of implantation and annealing steps, in quest for the desired size, morphology and size distribution of CdS nanocrystals -and probably other II-VI compounds-, formed by ion implantation of constituent atoms into a light matrix.

References:

- [1] A. Meldrum *et al*, *Advanced Materials (Review)* **13**, 1431-1443 (2001)
- [2] U V. Desnica, *et al*, *Nucl. Instr. Methods Phys. Res. B*, **200**, 191-195 (2003)
- [3] C.W White *et al*, *Nuclear Instruments & Methods in Physics -B*; **148**, 991-998 (1999)
- [4] D. Babonneau *et al*, *Phys. Rev. B*, **63**,195401 (2001)

ZnTe NANOCRYSTALS ION-BEAM SYNTHESIZED IN SiO₂

I.D. Desnica-Frankovic¹, U. V. Desnica¹, P. Dubcek¹, M. Buljan¹, S. Bernstorff², H. Karl³, I. Großhans³ and B. Stritzker³

1.) R. Boskovic Institute, PO Box 180, 10002 Zagreb, Croatia,

2.) Sincrotrone Trieste, SS 14, km 163.5, 34012 Basovizza, Italy

3.) Institut für Physik, Universität Augsburg, Universitätsstr. 1, D-86135 Augsburg, Germany

In this report we are presenting our studies on nucleation and growth of ZnTe quantum dots (QDs) formed by implantation of energetic ions into the thermal SiO₂. We have employed grazing incidence small angle X-ray scattering (GISAXS) to analyze the influence of implantation parameters and various post-implantation thermal treatments on the QDs' size and size distributions.

The samples were produced by implanting equal doses ($4 \times 10^{16}/\text{cm}^2$) of Te and Zn ions into the 300-nm thick thermally grown SiO₂ on (100)-silicon at room temperature (RT). The samples were subsequently annealed in a rapid-thermal-processing furnace at $T_{a1} = 800^\circ\text{C}$ for 16 min, at $T_{a2} = 1000^\circ\text{C}$ for 30 sec and $T_{a3} = 1000^\circ\text{C}$ for 16 min, in the flow of Ar+ 4% H₂ at atmospheric pressure.

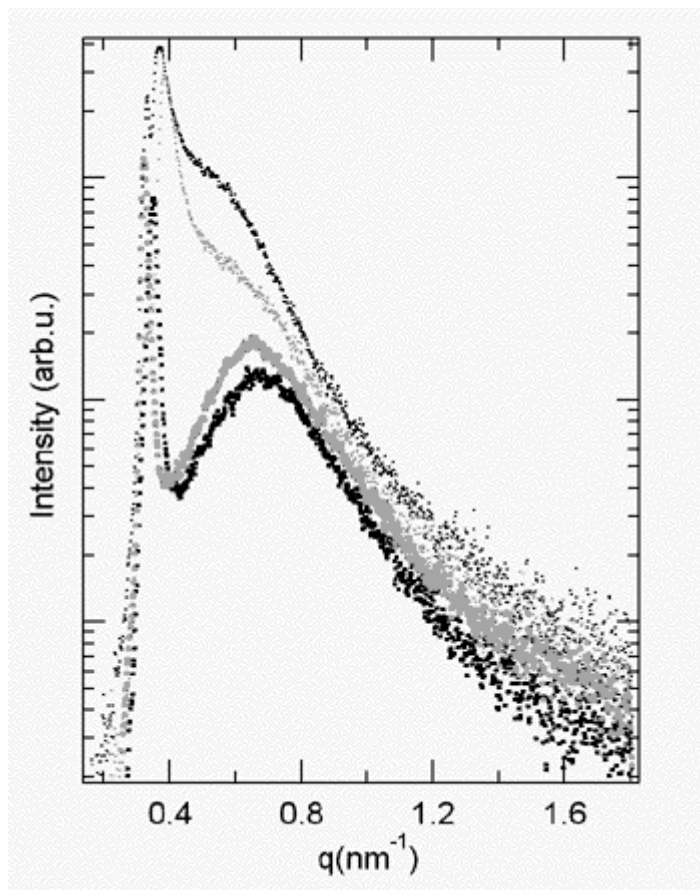


Figure 1. 1D cross-sections of GISAXS patterns for the Zn and Te-implanted samples, cut parallel to q_z . Curve (a) -black thick line- corresponds to the as-implanted sample; (b) -gray thick line- annealed at $T_a=800^\circ\text{C}$, $t_a=16\text{min}$; (c) -black thin line- at $T_a=1000^\circ\text{C}$, $t_a=30\text{sec}$; (d) -gray thin line- at $T_a=1000^\circ\text{C}$, $t_a=16\text{min}$. The curves are vertically offset for clarity.

The synthesis of nanoclusters begins already during implantation, giving rise to the scattering (a) in Fig. 1. Small nanoclusters are spatially correlated, with average radius $R_g = 3.3\text{ nm}$ and an average interparticle distance of $d \approx 8\text{ nm}$ throughout the layer. The annealing at 800°C for 16 min introduces just slight changes in the scattering profile (b). However, after just 30 s

annealing at 1000 °C the correlation is lost, only weak shouldering is now present at the previous position of the interference maximum (curve *c*). A similar profile is obtained after 16 min annealing at 1000°C (curve *d*). From the linear parts of the plot of $\ln(I(q))$ vs. q^2 the average mean radius R_g was estimated, showing a steady increase from 3.3 nm, 3.4 nm, 3.8 nm up to 4.4 nm, with annealing temperature and time. Depth profiling for a sample annealed at 1000°C for 16 min is depicted in Fig. 2.

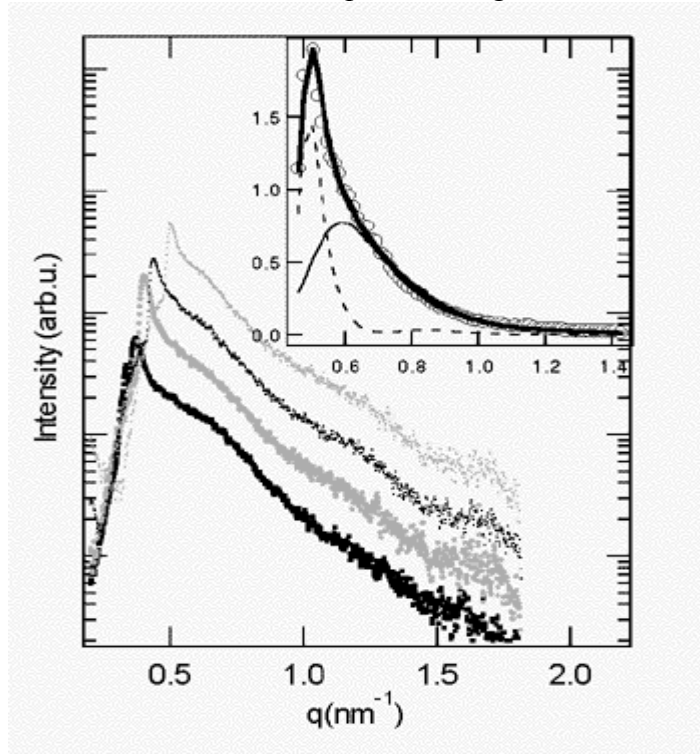


Figure 2. Cross-sections of GISAXS patterns for the Zn and Te-implanted sample annealed for 16 min at 1000°C. (a)-black thick line: $\alpha_i = \alpha_c$, (b)-gray thick line: $\alpha_i = \alpha_c + 0.05^\circ$, (c)-black thin line: $\alpha_i = \alpha_c + 0.1^\circ$, (d)-gray thin line: $\alpha_i = \alpha_c + 0.2^\circ$. The curves are vertically offset for clarity. *Inset:* the LMA fit to the 1D profile of (c), cut at a polar angle $F = 30^\circ$ with respect to the specular plane, together with the corresponding contributions of smaller and larger particles.

The angle of incidence was varied from $\alpha_i = \alpha_c$ to $\alpha_i = \alpha_c + 0.2^\circ$. For $\alpha_i = \alpha_c$ and $\alpha_i = \alpha_c + 0.05^\circ$ the signals are interpreted as arising from agglomerated clusters with a broad size distribution, that are not spatially correlated. The Fig. 2 - inset depicts the LMA fit to the 1D profile cut at a polar angle $F = 30^\circ$, together with the corresponding contributions of smaller and larger particles. The results suggest the presence of bi-modal size distributions with a maximum centered at $R_{LMA,1} = 2.5$ nm for smaller particles, and a larger clusters diameter of approximately 30 nm. The size distribution is very broad with $w_1 = 2.4$ nm and $w_2 = 9.6$, respectively. Nonetheless, at least two concerns complicate these conclusions. First, the fit with so many parameters does not a priori yield fully reliable numerical results and, second, the contribution of larger particles is partially blocked by the shadow of the sample, thus not easily discernable.

In conclusion, by the analysis of 2D GISAXS patterns a successful ion-beam synthesis of ZnTe quantum dots in SiO_2 samples was confirmed. The formation of small particles was noticed already in the as-implanted sample, indicating that the diffusion of Zn and Te atoms and their fusion into the ZnTe nanocrystals occurs already during the process of implantation itself when the implanted doses are sufficiently high. A successive thermal treatment of the implanted samples causes further growth of particles, with the average size depending strongly on annealing time and temperature. However, various effects influence these processes, in the first place, the influence of the radiation-induced damage. Those defects serve as nucleation sites for precipitation, implying that the distribution of the QDs and especially its size distribution, could be significantly influenced by the initial damage distribution.

GISAXS STUDY OF DEFECTS IN DEUTERIUM IMPLANTED MONOCRYSTALLINE SILICON

Pavo Dubcek¹, Branko Pivac¹, Sigrid Bernstorff², Federico Corni³, Rita Tonini³ and Gianpiero Ottaviani³

1.) Rudjer Boskovic Institute, P.O. Box 180, HR-10000 Zagreb, Croatia

2.) Sincrotrone Trieste, SS 14 km 163.5, I-34012 Basovizza (TS), Italy

3.) Department of Physics, University of Modena, Via Campi 213a, I-41100 Modena

We present a grazing incidence small angle X-ray scattering (SAXS) study on deuterium implanted silicon with a subsurface damaged layer. Samples were p-type (1.7-2.5Ωcm), Czochralski grown, (100)-oriented silicon wafers implanted with D₂⁺ ions at an energy of 24 keV and a dose of 2x10¹⁶ cm⁻². The samples were kept at liquid nitrogen temperature while the beam was scanned over the sample surface during the implantation process and tilted by 7° to minimize ion channelling. The implantation energy of 24 keV was chosen to achieve the D projected range R_v of about 220 nm with straggling ΔR_v of 85 nm according to simulation by SRIM98 code. This implantation energy is high enough to ensure that D does not effuse and escape from the surface during the implantation and during the storage at room temperature. At the same time the D projected range is in the correct order of magnitude for technological applications related to solid state devices of the next generation.

Two dimensional GISAXS intensity patterns for the as-implanted and for the sample annealed at 773 K are shown in Fig.1. The grazing angle was 1°, which corresponds to about 500 nm penetration depth, i.e. the whole implanted region (220 nm) is covered. By an appropriate choice of absorber for attenuation of the specular intensity, simultaneous detection of both in- and out-of specular plane intensity is possible. The Yoneda peak is situated at q_z=0.9 nm⁻¹, and the specular one at q_z=1.6 nm⁻¹. It is worthwhile to note that the broadening of the specular peak intensity is due to a slight detector overflow (it is not due to the correlation in the surface).

There is an additional diffuse scattering intensity further away from the specular plane, a fingerprint of particles randomly distributed within the sample. The voids generated by implantation are too small to be detected by SAXS, and therefore this diffuse signal is barely visible in Fig.1(a). There is also a signal parallel to the specular plane, which we attribute to a high concentration of defects arranged parallel to the sample surface, since the energy transfer during the implantation process is depth dependant. When the sample was annealed at 773 K, the voids have obviously agglomerated to larger particles, giving rise to the stronger diffuse signal in Fig.1(b).

In Fig.2, the vertical scans of intensity vs. the scattering angle q_z along q_y = 0 (the upper set of curves, specular scan) and along q_y = -0.2 nm⁻¹ (the lower curves, off-specular scan) are shown for three annealing temperatures, as indicated for each curve. The lower set can be used to gauge the size of the agglomerates of the voids. These sizes vary from 0.9 to 1.2 nm, as obtained from the fit to Guinier approximation after correcting for refraction and absorption of the X-rays in the film (Lee, 1995), although the error margin is large due to low intensity.

However, there is a general trend of increment of the diffuse scattering intensity with the annealing temperature as can be seen from the lower set of the scattering curves in Fig. 2.

The specular plane intensities (Fig.2) are showing the onset of fringes (quite clearly resolved in the vicinity of the Yoneda peak, even for the as implanted sample, but dissolving into the noise at wider angles). These can be used for a rather precise film thickness determination. The values obtained by fitting to the scattering from two weakly correlated rough surfaces are decreasing from 40 nm for the not annealed sample, to 34 nm for the 573 K, and to 20 nm for

the 773 K annealed one. Keeping in mind that deuterium was implanted down to the projected range of about 220 nm, this can only be explained by a build up of a certain sharp interface between a defect rich and a defect poor region, which is governed by the crystal planes of the monocrystalline sample, and therefore correlated to the sample surface. The diffusion of defects increases with increasing temperature, and this pushes the interface towards the sample surface. This process is accelerated above 573 K.

An X-ray reflectivity experiment is planned in order to precisely determine the surface parameters and also to gain better insight into the particle scattering, which could thus be deconvoluted from the surface contribution in GISAXS.

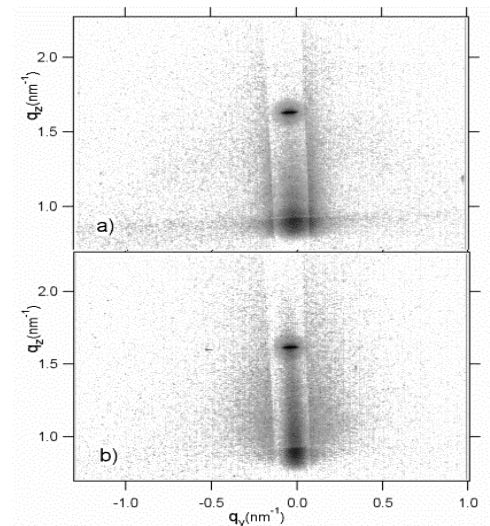


Figure 1. 2D GISAXS intensity pattern from D implanted a) not annealed and b) 773 K annealed monocrystalline silicon. The vertical white strip is the shadow of the absorber, while the Yoneda and the specular peaks are visible at $q_z=0.9\text{nm}^{-1}$ and $q_z=1.6\text{nm}^{-1}$, respectively.

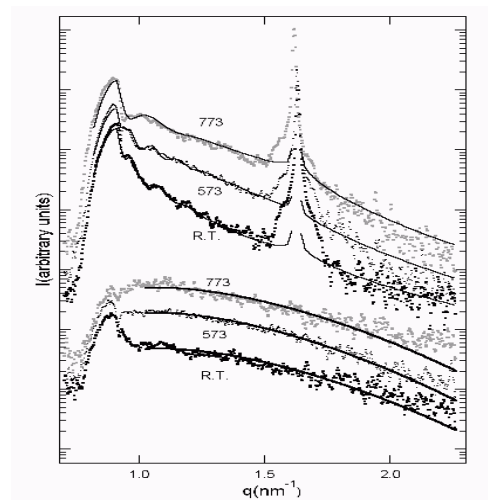


Figure 2. Specular (upper set) and off-specular (lower set) GISAXS intensities (dots) and the corresponding best fits (full lines) vs. the scattering angle, extracted from 2D detector pattern like that in Fig.1. for several annealing temperatures (indicated in the graph in K) and with the specular peak intensity attenuated. The curves are offset vertically for clarity.

GRAZING INCIDENCE SMALL ANGLE X-RAY SCATTERING STUDY OF IRRADIATION INDUCED DEFECTS IN MONOCRYSTALLINE SILICON

P. Dubcek¹, B. Pivac¹, S. Bernstorff², F. Corni³, R. Tonini³, and G. Ottaviani³

1.) Rudjer Boskovic Institute, P.O. Box 180, HR-10000 Zagreb, Croatia

2.) Sincrotrone Trieste, SS 14 km 163.5, I-34012 Basovizza (TS), Italy

3.) Department of Physics, University of Modena, Via Campi 213a, I-41100 Modena, Italy

We present a grazing incidence small angle X-ray scattering (GISAXS) study on He implanted silicon, in which a subsurface damaged layer was formed. Samples were *p*-type (1.7-2.5 Ωcm), Czochralski grown, (100)-oriented silicon wafers implanted at 20 keV with a fluence of $2 \times 10^{16} \text{ cm}^{-2}$, at a beam current density of about $8 \mu\text{A cm}^{-2}$. The samples were kept at liquid nitrogen temperature during the implantation process and tilted by 7° to minimize ion channeling. The implantation energy of 20 keV was chosen to achieve the He projected range R_p of about 220 nm with straggling ΔR_p of 85 nm. The implantation dose was below the bubble formation threshold.

The helium and defects distribution is known to vary smoothly with depth, apart from slightly different distributions for interstitials and voids. Nonetheless, the intensity fringes close to the Yoneda peak (see fig. 1.) suggest the presence of a clearly defined film structure with a sharp transition interface already in the not annealed sample. These oscillations are a precise measure of the film thickness. In case of the 300°C annealed sample, these intensity oscillations are present in the full range of the scattering angle. The detected film thickness (about 250nm) is attributed to the implanted layer itself. In order to exclude the influence of an impure surface and/or a surface oxide layer, the sample surface has been cleaned by etching (CP4), and the experiment was repeated with the same outcome.

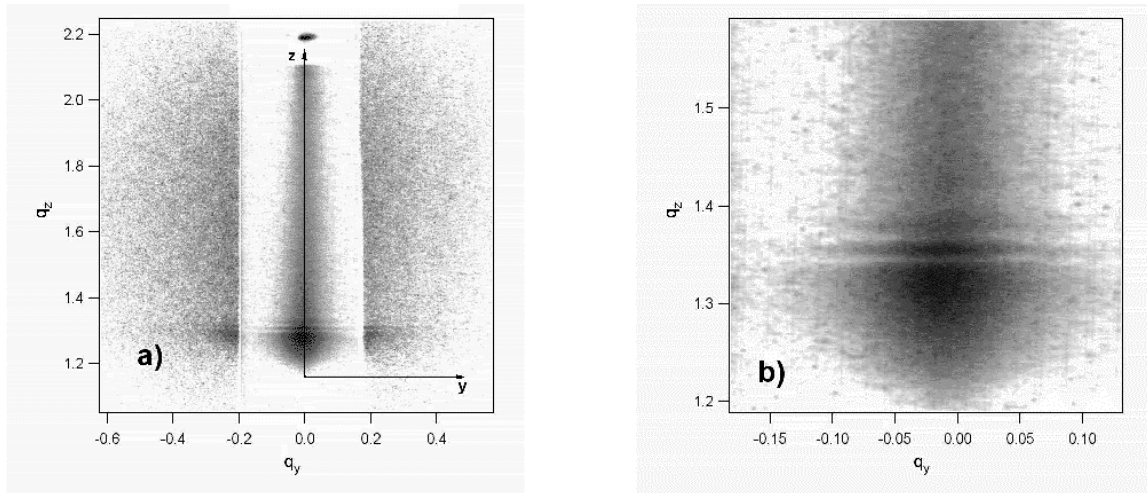


Figure 1. a) 2D GISAXS intensity pattern from He implanted not annealed silicon, b) detail from a) around the Yoneda peak. The vertical and horizontal lines represent the specular (*z*) and the sample surface plane (*y*), respectively.

Additional to this surface signal, there is a weak diffuse scattering intensity further away from the specular plane (see fig 2), a fingerprint of particles randomly distributed within the sample. Taking vertical scans in the specular plane, we can measure the film structure contribution (here, the surface signal is much stronger than the particle scattering). This is

shown in Fig.2, for the not annealed sample, and for samples annealed at 300°C, 500°C and 700°C, respectively.

Immediately after the implantation a film type structure is formed, giving rise to intensity oscillations, but, except for the 300°C annealed sample, these can only be seen close to the Yoneda peak (as shown in fig. 1.b for the not annealed sample). The thickness of this film type structure is slowly decreasing with the annealing temperature. The surface roughness value, obtained from the fit to the distorted wave Born approximation is similar for all the intensities displayed ($\sigma = 0.7-0.9$ nm). This is most obvious in the case of the 300°C annealed sample, where there is a broad maximum in intensity at $q_z=1.7\text{nm}^{-1}$ partly masked by the oscillations of the film scattering intensity. To make it more obvious, we plotted over it the so called off-specular scan for the same sample. This is the diffuse scattering intensity taken parallel to the specular plane at the edge of the attenuator (vertically at $q_y = -0.2\text{nm}^{-1}$ in fig 1.). Note the low intensity of this scattering, as compared to the background values on the same curve, on the left from the Yoneda peak ($q_z=1.5\text{nm}^{-1}$).

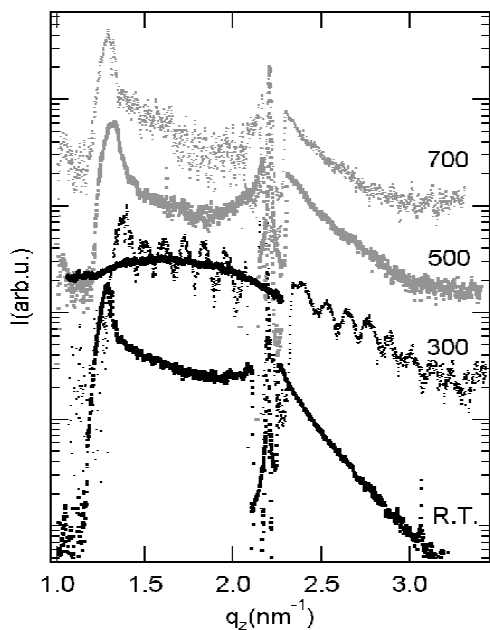


Figure 2. Specular plane GISAXS intensities vs. the scattering angle, extracted from 2D detector measurements as that in Fig.1. for several annealing temperatures (indicated in the graph in °C) and with the specular peak intensity attenuated. In addition, the diffuse part of intensity (see the discussion) is plotted for the 300°C annealed sample.

We must keep in mind that 300°C is the temperature at which the defects in silicon start to move and to rearrange, which results in structural relaxation, and in an enhancement in the surface-to-voids depth correlation (see the clearly resolved scattered intensity fringes). Higher temperature annealing partly destroys this correlation, due to enhanced freedom of voids/helium atoms movement and, possibly, the onset of the real bubbles formation.

Taking account the refraction and absorption, and applying the Guinier approximation, the detected sizes are in the order of $R_G=1\text{nm}$. The absence of this signal at smaller grazing angles suggests that the agglomeration of defects/helium atoms, about 2nm in diameter, are present some 150nm below the sample surface.

GISAXS STUDY OF STRUCTURAL RELAXATION IN AMORPHOUS SILICON

P. Dubcek¹, B. Pivac¹, S. Bernstorff², R. Tonini³, F. Corni³, and G. Ottaviani³

1.) Rudjer Boskovic Institute, POBox 180, 10000 Zagreb, Croatia

2.) Sincrotrone Trieste, SS 14km163,5, 34012 Basovizza(TS), Italy

3.) Dipartimento di Fisica, University of Modena, Via Campi 213a, 41100 Modena, Italy

The amorphous silicon network where Si atoms are fourfold coordinated and covalently bonded is very well described by a continuous random network. Structural relaxation of the amorphous network and defect annihilation in pure amorphous silicon has been recently extensively studied. To understand the evolution of such residual defects in crystalline Si at very high implantation doses, Si self-ions have been used to eliminate chemical effects.

It has been shown that amorphous silicon prepared by ion implantation is about 2% less dense than the crystalline one. Moreover, it has been also reported that the density was not affected by annealing to temperatures up to 580°C, indicating that changes in vibrational, structural, and thermodynamic properties of ion-implanted amorphous silicon are intrinsic to the system described with covalently bonded continuous random network and are distinctly different from densification involving removal of macroscopic voids sometimes observed in deposited films of silicon alloys. Although several studies of high temperature annealing of amorphous silicon have been done, only little is known about the structural changes which occur before the first stable seeds appear in the film.

The experiment was performed on monocrystalline samples implanted with a dose over the amorphisation threshold. Since a single energy of implantation was used, the damage in the sample is a asymmetrical, rather smooth function of depth, where the maximum of stopped ions is expected to be at about 40nm below the surface, with half-width-half-maximum of about 25nm, while the damage is rather low at the very surface (where the energy of the implantation ions is still too high) and increases deeper in the sample. Obviously, only at a certain depth the volume dose (i.e. damage to the crystal structure) was high enough to cause the onset of amorphisation. Therefore, below the topmost part of the sample, weakly affected by the implantation process, an amorphous silicon film of a certain thickness is expected to be generated.

For probing the film structure, grazing incidence is a preferred orientation. For GISAXS, the scattered intensity carrying the information about the film would be reduced to the specular plane (a flat sample surface). We used a high-dynamical-range gas detector to measure this GISAXS intensity, which is shown in Fig.1. for two different samples and for three grazing angles.

For both samples and all three grazing angles, the Yoneda peak at the critical angle above the grazing angle position is well resolved. The diffuse part of the specular peak (at twice the grazing angle) indicates a somewhat increased diffuse component suggesting that part of it comes from the monocrystalline/amorphous interface below. Also the roughness value ($\sigma=0.7 \pm 0.1$ nm for the received sample and $\sigma=0.8 \pm 0.1$ nm for the annealed one), obtained from the fit to the Distorted Wave Born Approximation (DWBA), and higher than measured for a monocrystalline sample, is dominated by the mentioned monocrystalline/amorphous interface. The hump in the scattering curves at about $S=0.2\text{nm}^{-1}$ for the lowest grazing angle, as well as an unusually strong diffuse part of the specular intensity in the second grazing angle curves suggests contribution to the scattering which is not grazing angle dependent, and which is typical for the presence of particles as scattering centers, evenly distributed within the film. It would be below the grazing angle, and therefore not detectable, for the third pair of the scattering curves (the largest grazing angle). In the case of scattering from correlated particles within the film, a diffuse ring in intensity is expected for the given 2θ scattering angle,

superposed to the surface scattering, but not dependant on the grazing angle, apart for the necessary correction for refraction and absorption [1]. The average particle distance is given roughly by the position of the maximum in the scattering intensity, while the particle size would be somewhat smaller.

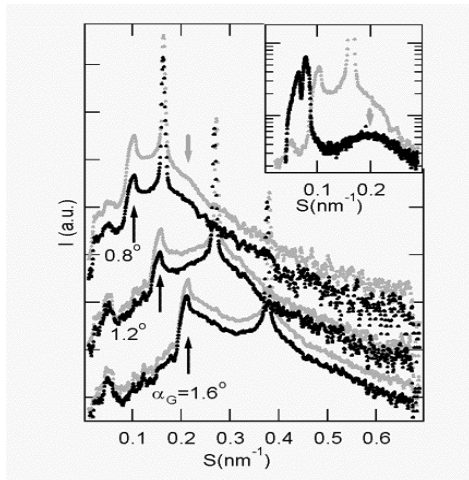


Figure 1. GISAXS from as implanted (black) and annealed (gray) sample vs. scattering angle for three different grazing angles. In the insert scattering from the annealed sample taken in the specular plane with a 1-dim detector (gray) is compared to the offset scan from the 2-dim detector (black). The position of the particle contribution is indicated by a gray arrow.

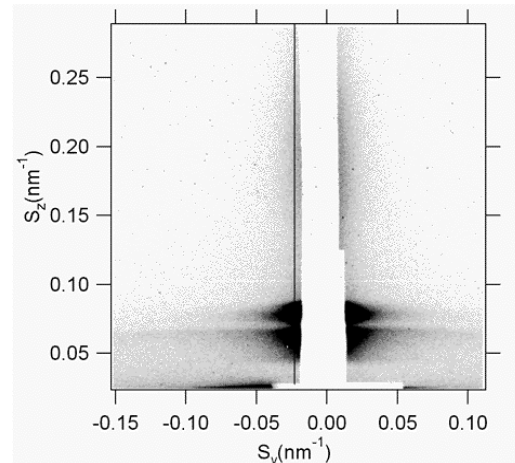


Figure 2. GISAXS from the annealed sample measured by the 2-dim detector with the specular plane intensity depleted by an absorber (vertical white strip). The position of the offset specular scan is indicated by the line.

In order to test for the presence of particles, another GISAXS experiment was performed, this time using a 2-dim detector, and the scattering pattern for the annealed sample is shown in fig.2. The absence of a diffuse, ring like intensity distribution is evident although a slight increase of the scattering intensity in the vicinity of the specular plane can be seen. Since the generation of rather big (about 10nm) agglomerates of voids and/or defects is not expected in the case of self implantation, this scattering is attributed to the thickness of the topmost monocrystalline part of the sample: due to a slight difference in density and a sharp interface between the crystalline and amorphous part, which is highly correlated to the top surface of the sample (due to the nature of the implantation process) this is the first oscillation in scattering intensity due to the interference between scattering from the top surface and the mentioned interface [2], revealing the thickness of the top monocrystalline layer to be about 10nm. X-ray reflectivity measurements are under way to confirm this assertion.

The film structure of the sample as the origin of the scattering in this range is supported by the insert in Fig 1. where a scan taken in the specular plane, and a so called off-specular scan, are compared.

References:

- [1] S. Dietrich, A. Haase, Phys Rep., **260**, 1 (1995)
- [2] C. Schug, P. Lamparter and S. Stib, Physica B **248**, 62 (1998)

CHARACTERISATION OF GRAINS IN TUNGSTEN-CARBON FILMS

P. Dubcek¹, N. Radic¹, O. Milat² and S. Bernstorff³

1.) Ruder Boskovic Institute, Bijenicka 54, 10000 Zagreb, Croatia

2.) Institute of Physics, Bijenicka 46, 10000 Zagreb, Croatia

3.) Sincrotrone Trieste, SS 14 km 163.5, 34012 Basovizza (TS), Italy

Tungsten carbides with their superior mechanical, electrical and chemical properties are promising materials for a variety of applications, especially in form of thin films. In this work, WC films have been deposited onto monocrystalline silicon substrates by reactive d.c. magnetron sputtering, with benzene as the carbon-supplying admixture. The presence of tungsten-carbide grains in these films had already been verified [1], but the question of their shape remained unanswered.

2D GISAXS and SAXS patterns are displayed in fig.1. In the case of grazing incidence (fig1.a) the rough surface scattering is the dominating part of the signal: strong and rather wide (in the sample surface plane). Due to the high electron density contrast between the tungsten carbide particles and the surrounding amorphous matrix rich in carbon, fairly strong particle scattering is evident as a diffuse ring around the direct beam direction. Making use of the low intensity of the surface scattering outside of the specular plane, the particle scattering intensity was determined from the so called off specular scans (measurement of the intensity in the plane parallel to the specular plane, but far enough that the particle scattering becomes dominant).

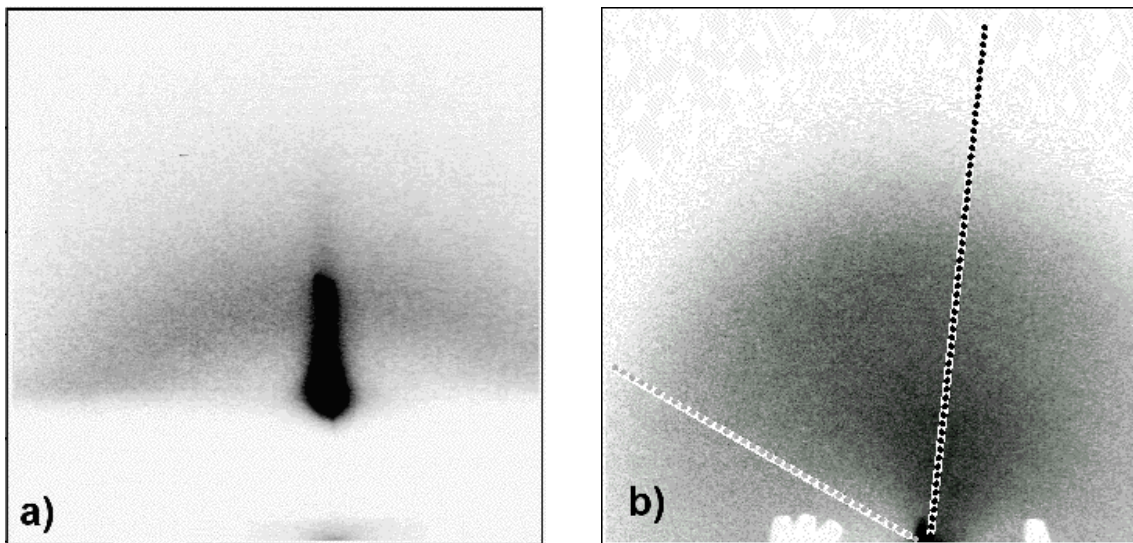


Figure 1. Two dimensional GISAXS (a) and SAXS (b) pattern from magnetron sputtered tungsten-carbide film.

The result of the scan is displayed in fig.2 (black line). The diffuse ring around the direct beam is a fingerprint of a densely packed system, where the low angle side of the scattering intensity has been depleted due to the vicinity of the particles. Supposing that the structure factor is not influencing too heavily the slope of the curve, a simple Guinier approximation is used to evaluate the size of the particles ($R_G=0.96\text{nm}$). On the other hand, the position of the scattered intensity maximum is a very good approximation for the particle interdistance ($L=2.9\text{nm}$ from fig 2). However, the homogenous diffuse ring of

scattered intensity, equally distanced from the direct beam for all azimuthal orientations, suggests spherical particles.

In fig.1.b) the transmission scattering pattern (standard SAXS) is shown, with the scattered intensity somewhat higher in vertical direction. The anisotropy of the scattered intensity is an indication of the nonspherical particle shape and/or uneven particle to particle distance in horizontal and vertical direction. The linear scans of intensity from fig 1.b) are also shown in fig 2. These have been taken in the direction of high (dotted black line) and low intensity (dotted gray line). These scans have also been analyzed using Guinier approximation and the particle to particle distance was gauged from the position of the maximum. The obtained values for the Guinier radius are 0.98 nm, 0.96 nm and 0.95 nm for maximum intensity, minimum intensity and GISAXS scan, respectively. Considerably higher is the difference in the distance: 2.8nm, 2.9nm and 3.4nm, respectively.

The apparently contradicting results from transmission and grazing incidence SAXS can be explained by the limited penetration depth for X-rays in grazing incidence (about 110nm, while the film thickness is a few hundreds of micrometers) accompanied by the inhomogeneity of the film in respect of the particle size and/or shape. A more detailed experiment is under way to resolve the question of homogeneity from particle shape and orientation anisotropy.

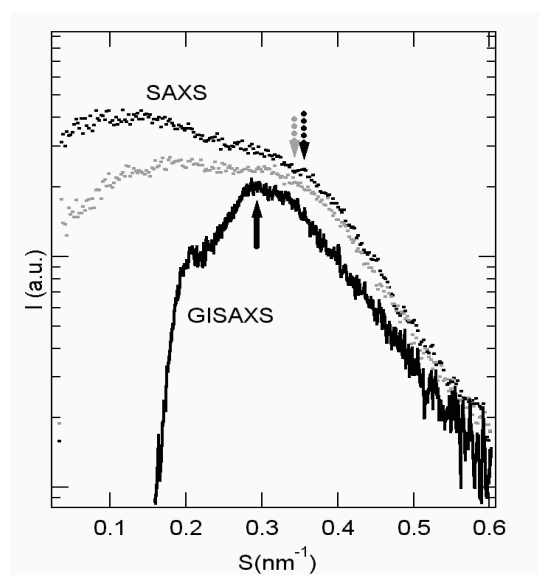


Figure 2. SAXS vs. scattering angle for magnetron sputtered tungsten-carbide film. The full line is the GISAXS scan from Fig. 1a, while the dotted lines are taken along the lines in Fig. 1b: for maximum (black) and minimum (gray) low angle intensity. The arrows indicate the positions of the maximum in the structure factor.

References:

- [1] P. Dubcek, N. Radic, O. Milat and S. Bernstorff, *Surface and Coatings Technology*, **151-15** (2002) 218

DEPTH PROFILING OF MARKER LAYERS USING COMBINED X-RAY REFLECTIVITY AND STANDING WAVES ANALYSIS IN X-RAY WAVE-GUIDE STRUCTURES

A. Gupta¹, A. Saraiya¹, V.R. Reddy¹, M. Gupta², S. Bernstorff³ and H. Amenitsch⁴

1.) Inter University Consortium For DAE Facilities, Khandwa Road, Indore, India

2.) Laboratory for Neutron Scattering, ETHZ & PSI, CH-5232 Villigen PSI, Switzerland

3.) Sincrotrone Trieste, SS 14, Km 163.5, I-34012 Basovizza, Trieste, Italy

4.) Institute for Biophysics and X-ray Structure Research, Austrian Academy of Sciences, Schmiedlstrasse 6, A-8042 Graz, Austria

Accurate depth profiling of thin marker layers (typically a few nm thick) is needed in a variety of measurement like, i) study of atomic diffusion in solid, ii) heavy-ion induced intermixing etc. Conventionally techniques like Rutherford backscattering spectrometry or SIMS/AES-depth profiling are used for this purpose with a typical depth resolution of 5-10 nm. We have used combined X-ray reflectivity and x-ray standing wave analysis techniques in order to obtain depth profile of a single marker layer with a resolution of better than 1nm.

The multilayer structure shown in fig. 1 was used for the studies. Measurements were done for two different metals, namely M= W, Fe. The bottom Au layer was deposited in order to achieve total external reflection of x-rays so as to form x-ray standing wave inside the multilayer [1], while the top 2 nm Au layer is used to achieve x-ray wave-guide structure [2]. Simultaneous x-ray reflectivity and x-ray fluorescence measurements were done using a linear PSD for reflectivity measurements and a PIN-diode detector with an energy resolution of 250 eV for x-ray fluorescence measurements. As the angle of incidence varies, the positions of the antinodes inside the multilayers shift and accordingly the fluorescence of the marker layer also exhibit variation, providing information about the depth distribution of the concentration of the marker element [1]. The formation of X-ray wave-guide structure results in sharpening of the antinodes as well as in improvement of the intensity of higher order antinodes, and thus is expected to increase the depth resolution.

Figure 2 gives the X-ray fluorescence yield from the W marker layer as a function of the angle of incidence of the x-rays (16 keV). The multilayer was irradiated with 100 MeV Au ions in order to induce intermixing with Si. The X-ray fluorescence yield after an irradiation influence of 1×10^{13} ions/cm² is also shown in figure 2. Substantial broadening of fluorescence peak after irradiation indicates intermixing as a result of Au irradiation. Figure 3 gives the x-ray reflectivity of the pristine multilayer. A combined fitting of XRR and X-ray fluorescence data has been done in order to obtain accurate depth profile of W layer. The continuous curves in the figure 2 and 3 show the preliminary fittings of the data. Figure 4 gives the corresponding depth distribution of various element in the pristine sample. The analysis shows that the W layer is not in the center of the Si layer, rather it is shifted by 1nm towards the bottom of the multilayer. A large interface roughness results in broadening of the depth profile of the W layer with a FWHM of ~5nm. Detailed analysis of the experimental data is underway in order to get information about the efficiency of intermixing of W and Fe layers with Si under the irradiation of 100MeV Au ions.

References:

[1] S. K. Ghose, B. N. Dev and *Ajay* Gupta, Phys. Rev. B 64 (2001)233403

[2] Y.P. Feng et al., Phys. Rev. Lett. 71 (1993) 537.

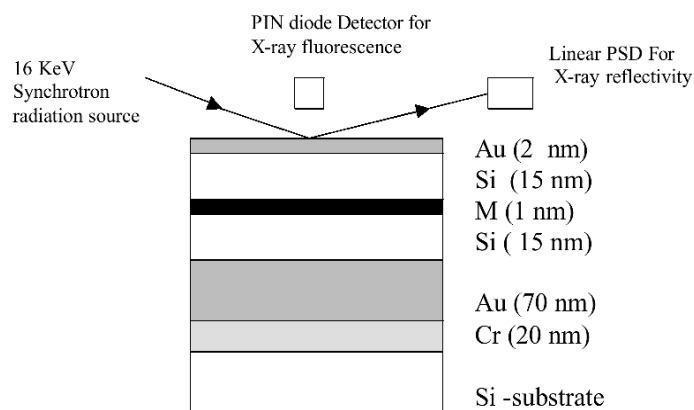


Figure 1. Structure of the multilayer used in the present studies. Two sets of multilayers with M=W and Fe were studied. Thickness of M layer was varied.

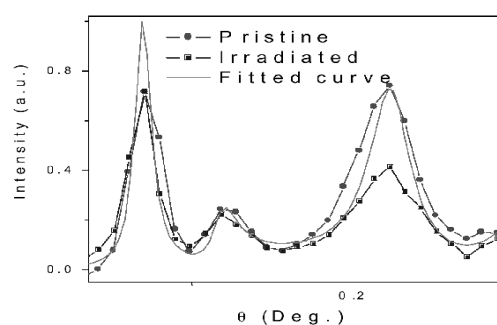


Figure 2. X-ray fluorescence yield data from the pristine and irradiated (1×10^{13} Au ions/cm²) specimens. The continuous curve represents theoretical fit to the data of pristine specimen.

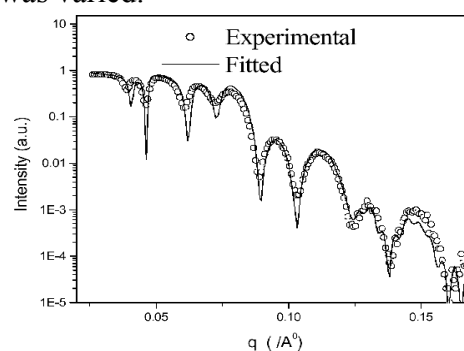


Figure 3. X-ray reflectivity data of the pristine specimen. The continuous curve represents theoretical fit to the data using Parratt's formulism.

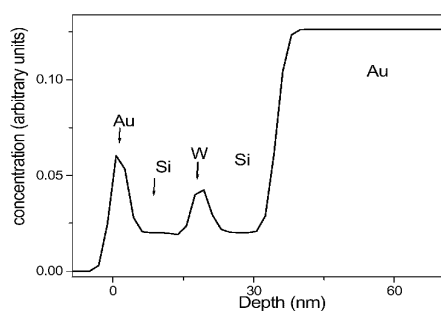


Figure 4. Depth profiles of different elements in the pristine specimen obtained by simultaneous fitting of the reflectivity and fluorescence yield data.

MIXTURES OF REVERSE PLURONIC COPOLYMER AND SURFACTANTS AS CONTROLLED-RELEASE DRUG DELIVERY SYSTEMS

L. Paduano¹, F. Lo Celso², A. Triolo³ and R. Triolo²

1.) Dipartimento di Chimica, Università di Napoli, Napoli, Italy

2.) Dipartimento di Chimica Fisica, Università degli Studi di Palermo, Palermo, Italy

3.) Istituto Processi Chimico-Fisici, Sezione di Messina – CNR, Italy

Self assembly properties of polyethylene oxide (PEO) based block copolymers in selective solvents have been largely investigated in recent years. In particular much attention has been devoted to aqueous solutions of tri-block copolymers containing PEO and polypropylene oxide (PPO) units. Polyoxyalkylene tri-blocks, are commercially known under their trade name Pluronic (BASF). The term direct Pluronics (D-Pluronics) is used to indicate tri-blocks with the sequence PEO-PPO-PEO, while the term reverse Pluronics (R-Pluronics) is used for the sequence PPO-PEO-PPO. Despite their wide spread use in a variety of industrial formulations, only few structural investigations of aqueous solutions of reverse Pluronics have been performed. While both D- and R-Pluronics may form spherical micelles in water in a large region of the phase diagram, one expects differences between the two. In fact, the hydrophobic tails (PPO segments) favor the interaction between the micelles, promoting the formation of a network of micelles (R-Pluronics) rather than independent micelles like those generally found in the case of D-Pluronics. SAXS results have been obtained for aqueous solutions of R-Pluronics 25R4 and 25R5 corresponding to $(\text{PO})_{19}\text{-(EO)}_{33}\text{-(PO)}_{19}$ and $(\text{PO})_{18}\text{-(EO)}_{48}\text{-(PO)}_{18}$, respectively.

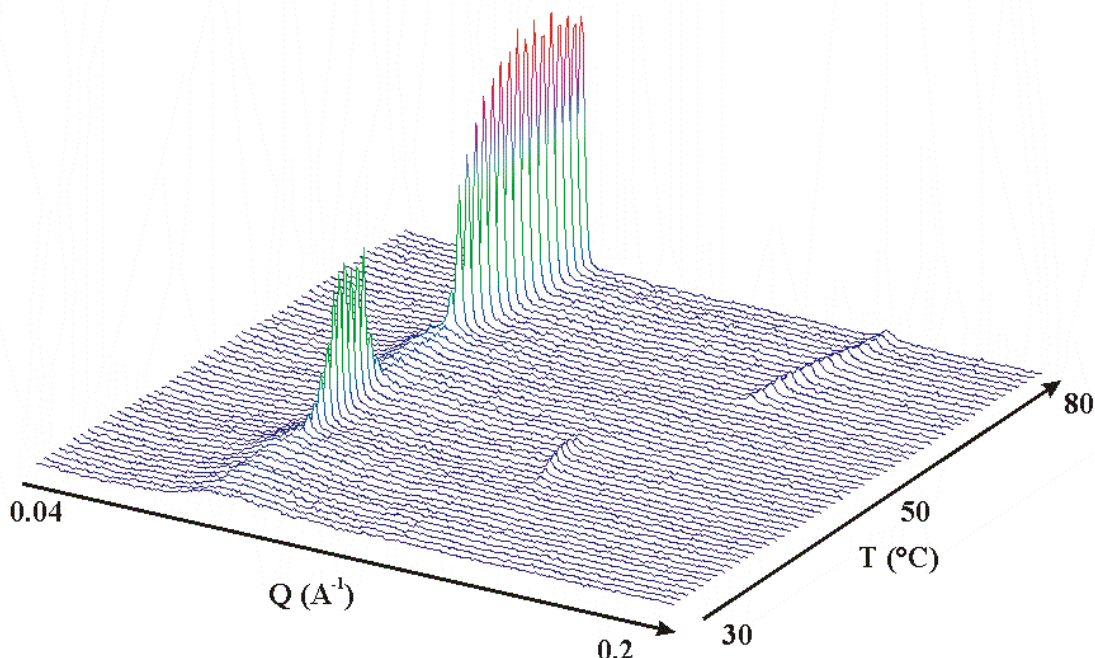


Figure 1. TR SAXS pattern for a 50% 25R4 aqueous solution as function of temperature.

Time Resolved (TR) SAXS pattern for a 50% (w/w) solution of 25R4 in D_2O as function of temperature are shown in figure 1. Close to room temperature the SAXS pattern is almost featureless, while a strong peak appears at higher temperatures. It is also present a secondary

peak (rather weak) which identifies an ordered mesophase (hexagonal packing, since the positions of the maxima are in a ratio of $1:3^{0.5}$). By further increasing the temperature (~ 60 °C) an additional transition is found. In this case the positions of the maxima are in a ratio of $1:2$, indicating that the system undergoes a transition from hexagonal packing to lamellae.

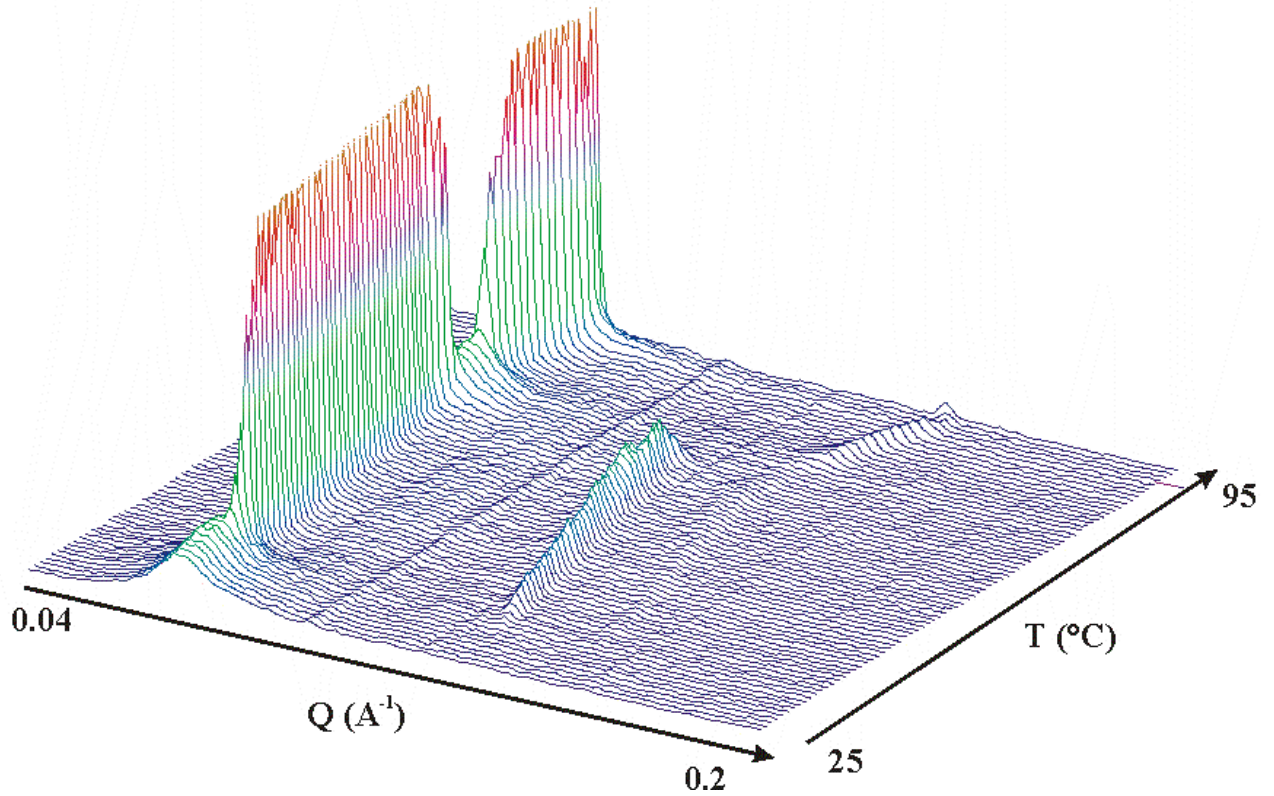


Figure 2. TR SAXS pattern for a 50% 25R5 aqueous solution as function of temperature.

TR-SAXS measurements have been also performed on aqueous solutions of the R-Pluronic 25R5 (see fig. 2). The pattern is characterized, in a wide range of temperatures ($35\text{-}75$ °C), by the presence of 3 peaks. The position of these peaks (in the ratio $1: 2^{0.5}: 3^{0.5}$) identifies a ordered microcubic structure. At higher temperatures a transition from cubic to hexagonal packing can be seen.

SAXS STUDY OF OXYGEN PRECIPITATION IN SILICON

B. Pivac¹, P. Dubcek¹, S. Bernstorff², A. Borghesi³, A. Sassella³, and M. Porrini⁴

1.) Rudjer Boskovic Institute, POBox 180, 10000 Zagreb, Croatia

2.) Sincrotrone Trieste, SS 14km163,5, 34012 Basovizza (TS), Italy

3.) Dipartimento di Scienza dei Materiali, Universita di Milano Bicocca, Via Cozzi 53, 20125 Milano, Italy

4.) MEMC Electronic Materials, Via Nazionale 59, 39012 Merano (BZ), Italy

Dislocation-free single crystal silicon grown by the Czochralski (Cz) method is used almost exclusively by the semiconductor industry in the manufacture of modern ULSI devices. In such material oxygen is the most important present nondoping light impurity which typically reaches about 10^{18} oxygen atoms cm^{-3} (20 ppm). Upon heat treatment during the processes of device fabrication, oxygen atoms diffuse through the lattice to form small agglomerates (nuclei) which further grow into precipitate particles of silica (SiO_2) [1]. These oxygen (silica) precipitates have very beneficial effects in the bulk of material since they getter unwanted impurities (typically metallic ions) and mechanically strengthen the silicon wafers. However, if they are formed in the electrically active regions of ULSI devices they can have disastrous effects on the device performance.

Czochralski grown single-crystal silicon samples, (100) oriented and boron doped with resistivity higher than $10 \Omega\text{cm}$ cut from adjacent positions at the tail of the ingot were used in this experiment. All the samples were subjected to the following sequence of thermal treatment: 15 min at 1000°C , nuclei formation at 650°C , homogenisation at 800°C and growth at 1000°C .

Due to the thickness of the samples ($500\mu\text{m}$) the first part of the experiment was performed using 16keV (0.77nm wavelength) radiation which is more penetrating and the obtained SAXS data are shown in fig.1. The growth of precipitates is evident from the stronger SAXS from a67 as compared to a62 at very small angles as a direct consequence of a much longer time of growth (120 h at 1000°C compared to 4h in a62). On the other hand, a longer nucleation time is not evident in figure 1 since the nucleation centers are too small to be detected as scattering centers.

In order to obtain a better signal to noise ratio, as well as to improve further the resolution towards the large particle side, the samples have been thinned down to $\sim 50\mu\text{m}$ thickness, and SAXS intensities have been collected at 8 keV using a 2D CCD detector, with averaging over pixels laying at the same scattering angle (2θ). The results are displayed in figure1, where the samples with longer precipitate growth time and longer nucleation time are compared to a referent one. Here, the difference due to the annealing is pronounced much better than in the case of 16keV scattering.

A normal size distribution was fitted to the measured intensities, as displayed in fig.2a. The maximum of the distribution is shifted to higher values (18nm compared to 13nm) for the longer growth time, while the halfwidth also increases (from 5.7 to 7.3nm respectively). According to this size distribution, a longer nucleation time causes only a change in the width of the distribution (from 5.7 to 6.7nm), while it peaks at a similar value (13.3nm and 14.6nm).

Table 1. Thermal treatment of the samples.

Sample	Thermal treatment
62	15 min @ 1000°C , 4h @ 650°C , 4h @ 800°C , 4h @ 1000°C
67	15 min @ 1000°C , 4h @ 650°C , 4h @ 800°C , 120h @ 1000°C
68	15 min @ 1000°C , 8h @ 650°C , 4h @ 800°C , 4h @ 1000°C

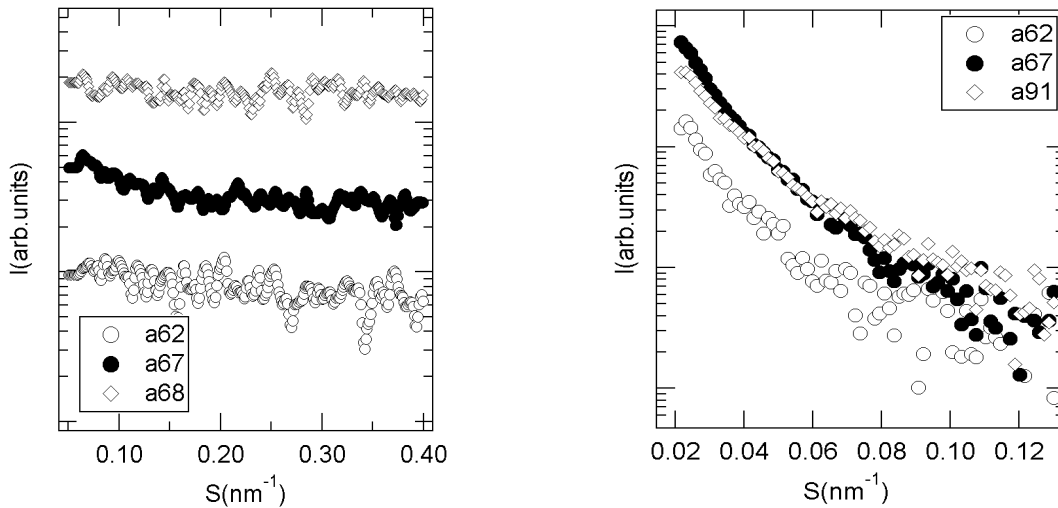


Figure 1. SAXS intensity for 16keV (left) and 8keV (right) radiation vs. scattering angle

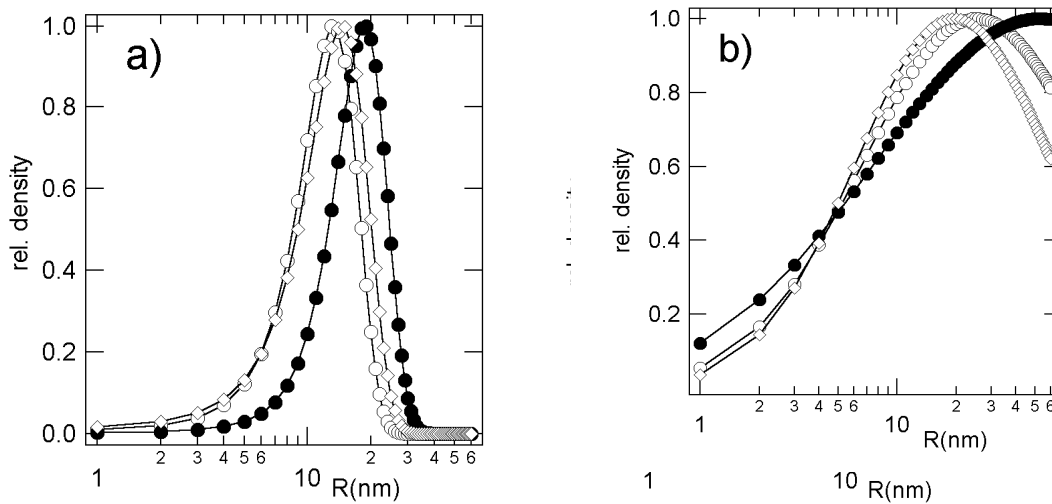


Figure 2. Size distributions from best fit to normal (a) and log-normal (b) distribution

Keeping in mind the nature of the precipitates production involved (nucleation of the centers, then the growth of the precipitates around these centers that are being generated also during the growth phase), it could be argued that the log-normal size distribution would be more appropriate for the fit. Also, the contribution of very small precipitates to the scattering is not overestimated as in the case of the symmetrical size distribution. The results of the fit to log-normal size distribution are displayed in fig.2b.

The most striking effect of this asymmetric fit is that the maximum of the size distribution is close to the edge of the experimental resolution in sizes suggesting the presence of much larger particles that cannot be resolved within the angular range used. This is true especially for the sample a68, where the maximum of the calculated distribution is almost the biggest particle size resolvable.

STUDY OF THE GROWTH PROCESS IN SEMICONDUCTING CDS NANOPARTICLES

S. Sapra¹, R. Viswanatha¹, H. Amenitsch², and D.D. Sarma¹

1.) Solid State and Structural Chemistry, IISc, Bangalore-12, India

2.) Institute of Biophysics and X-ray Structure Research, Austrian Academy of Sciences, Schmiedlstr. 6, 8042 Graz, Austria

It is now well-known that semiconducting nanoparticles provide us the unprecedented opportunity to tailor-make electronic and optical properties by varying the size of the nanoparticles. This arises from a tuning of the bandgap of the nanoparticle within the quantum confinement regime with the size of the particle and can be understood, though approximately, in terms of a particle-in-a-box like quantum mechanical approaches. There are more reliable calculation methods already established to provide a quantitative description of such quantum effects [2]. There are two distinctly different approaches to the synthesis of such nanoparticles, often termed as the physical and the chemical approaches. The chemical approach, which owing to its simplicity, flexibility and tunability is used extensively to prepare a wide range of systems so far, depends basically on stopping the reaction process leading to the formation of the semiconductor in a solution by adding a capping agent that binds to the surface of the growing nanoparticle and stops it from growing any further. This is therefore often termed the arrested precipitation method, e.g. [1]. Thus, it is evident that a systematic in-depth study of the growth of nanoparticles and its dependence on the various synthetic parameters, such as the concentrations of the precursor solutions and temperature, is urgently required and in principle, small angle x-ray scattering is an ideal technique to probe the growth.

As a model system of such formations we have studied the thermal initiated growth of CdS particles with the SWAXS camera in the SAXS beamline laboratory. After mounting of the capillary containing the freshly prepared precursors solutions inside the camera, the samples have been heated fast to 120 °C. The following evolution of the system has been monitored with a time resolution of 30 min. The obtained time dependent diffraction pattern are shown in fig. 1a. Guinier-radius and forward intensity (fig. 1b) calculated from the data evidence the fast growth and the interaction of the capping agent is seen by stopping the growth behavior after 10 h. A better understanding of the process has been achieved by calculating the size distribution for spherical particles from the desmeared scattering data with the GIFT program [3]. As seen in fig 2, in the beginning only the precursors with a size of about 1.2 nm are present, but within 4 hours the first large particles are formed with a final size of 3 nm stopped by the capping agent. The further development is based only in the conversion of the precursors into particles and consequently the increase of the volume fraction. The whole process is stopped as the precursors have been consumed fully.

From a fundamental point of view, there is hardly anything known about the growth mechanism in the regime of such small sizes. As observed from the results, such SAXS measurements will contribute for a deeper inside in the kinetics of nanoparticle formation.

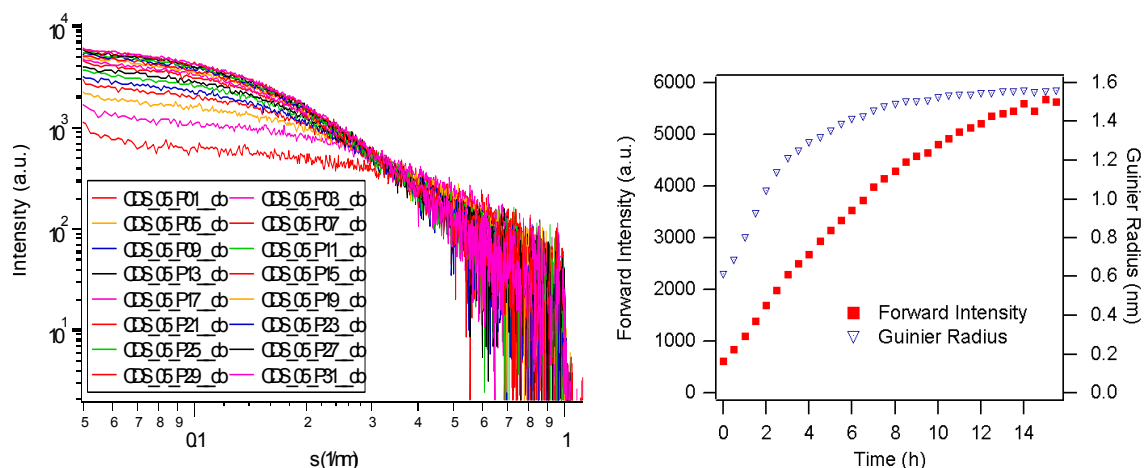


Figure 1. Experimental scattering curves measured during the thermal induced formation of CdS particles with the laboratory SWAXS system (a). Evolution of the forward intensity and guinier radius determined from the scattering data, clearly resolved the fast formation in the beginning and the final particles with a nearly monodisperse size of 3 nm (b).

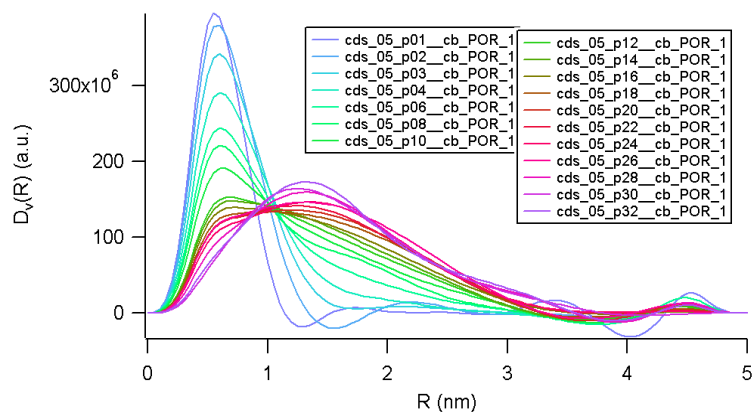


Figure 2. Evolution of the volume size distribution $D_v(R)$ assuming spherical particles with radius R depicting a bimodal size distribution given by the precursors 1.2 nm and the final particles 3 nm.

References:

- [1] Proc. of the 3rd Japan-Korea Joint Workshop on First-Principles Electronic Structure Calculations, pp. 105, 2001; Nano Lett. 2 (2002) 605; Phys. Rev. B 66 (2002) 205202.
- [2] Spectrochim. Acta 48A (1992) 1779; Appl. Phys. Lett. 61 (1992) 1655; Appl. Phys. Lett. 71 (1998) 1335; Phys. Rev. B 59 (1999) 7473; Appl. Phys. Lett. 74 (1999) 871; Chemistry of Materials 12 (2000) 1018; J. Appl. Phys. 90 (2001) 2504; Chem. Comm., 2188 (2001)
- [3] Bergmann, A., G. Fritz, and O. Glatter. 2000. Solving the generalized indirect Fourier transformation (GIFT) by Boltzmann simplex simulated annealing (BSSA). *Journal of Applied Crystallography* 33:1212-1216.

EPITAXIAL SELF ASSEMBLY OF NANOCRYSTALLITES – A NEW PARTICLE GROWTH AND DESIGN MECHANISM

L.C. Soare¹, N. Jongen¹, P. Bowen¹, V. Buscalia², H. Amenitsch³

1.) Ecole Polytechnique Fédérale de Lausanne, Laboratoire Technologie des Poudres, CH-1015 Lausanne, Switzerland

2.) Istituto per l'Energetica e le Interfasi (IENI), Consiglio Nazionale delle Ricerche, Area della Ricerca di Genoa, Via de Marini 6, I-16149, Genoa Italy,

3.) Institute of Biophysics and X-Ray Structure Research, Austrian Academy of Sciences, Schmedlstr. 6, 8042 Graz, Austria

Copper oxalate $\text{CuC}_2\text{O}_4 \cdot x\text{H}_2\text{O}$ ($0 < x < 1$) precipitates as polycrystalline particles built by the self-organization of nano-units. The particles have very regular morphologies and consist of crystallographically aligned subunits. The shape of the copper oxalate particles is influenced by the concentration of a polymer additive, hydroxypropylmethylcellulose (HPMC), when it is added to the precipitating agents. HPMC not only influences the final particle shape but also influences the shape of the nanocrystallite building blocks by adsorption onto specific crystal faces and modifying their growth. Surface energy and interactions of a hydrophilic-hydrophobic nature seem to be the dominating mechanism for the self organization of copper oxalate nanoparticles.

Kinetics experiments carried out in our laboratory show the nanostructure of copper oxalate aggregates as they are building up. According to Atomic Force Microscope and Scanning Electron Microscope characterization (figure 1), the particles reach a size of about 500 nm after 2 minutes of reaction (reactant concentration after mixing is 5×10^{-3} mol/L).

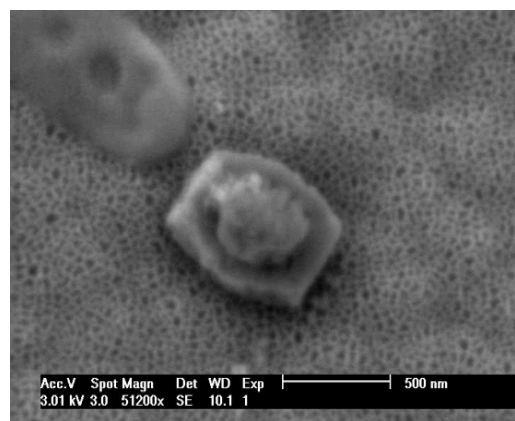


Figure 1a. SEM image of copper oxalate after 2 minutes of ageing time.

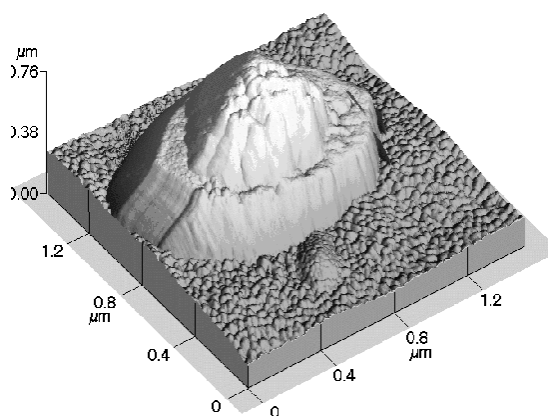


Figure 1b. Topography of a typical particle under construction.

Using laser light scattering it is difficult to detect the nanocrystals formed by reaction in the first two minutes. It is also important to understand which forces are responsible for lining up the crystallites as they approach the self-organization structure, as well as the kinetics of crystal growth. The analysis and understanding of nucleation from solution is a challenging task. For very fast precipitation reactions only a few techniques are available. Small Angle X-ray Scattering (SAXS) can give new insights in the early stages of the precipitation on a ms scale. Therefore an attempt to follow the evolution of the crystallite in situ during the first 2 minutes of precipitation was undertaken using SAXS.

One of the limitations of the method is the need of a volume ratio solid/liquid above 0.1% to ensure a reasonable signal/background ratio. To meet these conditions the reactant concentrations were increased to 25×10^{-3} mol/L. A higher concentration implies a high supersaturation and therefore a much shorter induction time and an increased growth rate. The precipitation of copper oxalate was carried out in a stopped flow capillary (2 mm diameter) with 60 μ L volume. Data were collected every 0.1 seconds for the first 60 seconds, every 0.5 seconds for the following 120 seconds and for the next 7 minutes every 1 second. The experiments were always made at room temperature.

The investigation of the copper oxalate by SAXS in general supports our model involving nucleation, crystal growth and aggregation. The particles reach a size of 25 nm in the first few seconds and then the intensity is constant (Figure 2), suggesting the crystallites nucleate and grow quickly then agglomerate as seen in the AFM and SEM.

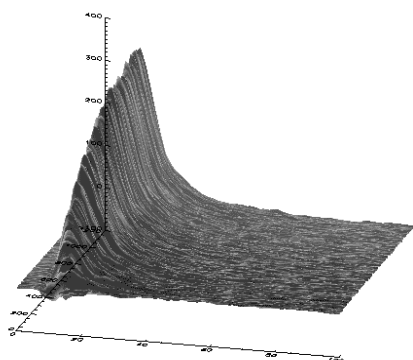


Figure 2a. SAXS profile of copper oxalate precipitation in the first few seconds with a nano crystal size of about 25 nm.

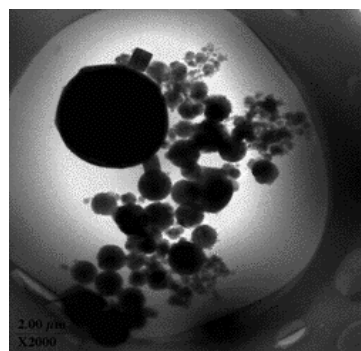


Figure 2b. Cryo TEM measurement with an ageing time of 30 seconds.

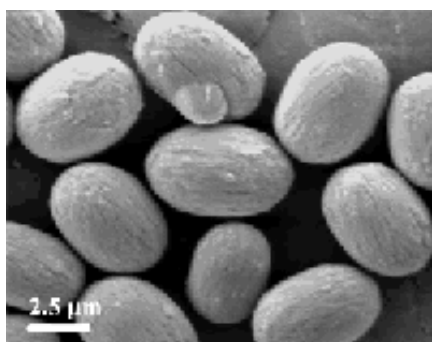


Figure 2c. SEM image of copper oxalate particles after 30 minutes.

To complete the SAXS experiments, methods such as Cryo-Transmission Electron Microscopy was also used. By Cryo-TEM, the size of the nano crystals before agglomeration after 30 second of ageing time was evaluated by freezing the suspension. The results were then correlated with the SAXS measurements. However, the Cryo-TEM shows a wide aggregate size distribution together with nanosized crystals.

The SAXS experiments still support the hypothesis of the formation of copper oxalate particles through a self-organisation process involving nucleation, crystal growth and growth by agglomeration. But further works with better signal to noise, better mixing and lower intervention with glass capillary wall should lead to better resolution and a more detailed understanding of the growth mechanism.

SYNCHROTRON WAXS & SAXS STUDIES OF MICROSTRUCTURAL EVOLUTION DURING POST-YIELD DEFORMATION OF ISOTACTIC POLYPROPYLEN (PT.II)

H. Wilhelm¹, A. Paris¹, E. Schafner¹, S. Bernstorff², J. Bonarski³, T. Ungar⁴, M. Zehetbauer¹

1.) Institute of Material Physics, University of Vienna, Vienna, Austria

2.) Sincrotrone Trieste, Trieste, Italy

3.) Institute of Metallurgy and Materials Science, Polish Academy of Sciences, Krakow, Poland

4.) Department of General Physics, Eötvös University Budapest, Budapest, Hungary

This work was carried out to check samples from melt-crystallised and deformed polypropylene for the evidence of dislocations before and after plastic deformation. In contrast to metals, polymers are not well understood as concerns the fundamental mechanisms operating during plastic deformation. One reason is that classical methods like electron microscopy are not universally applicable with polymers. While it is possible to observe dislocations in solution-grown single crystals, for melt-crystallised spherulites no preparation method exists which allows for the detection of dislocations. In this situation a new X-ray diffraction method revealed to be useful, i.e. the Multiple X-ray Profile Analysis (MXPA) [1, 2] which has been applied here for the first time to both undeformed and deformed samples of isotactic polypropylene. The check for dislocations has been done by evaluation of the width of the profiles (FWHM analysis) in the modified Williamson-Hall-plot. In case of the presence of dislocations, the peak width ΔK should increase linearly with $K^2 C$ (C is the contrast factor of dislocations, and K is the diffraction vector). From the slope of this plot, the density of dislocations can be derived while the lamella (crystal) thickness is determined from the section at the ΔK axis.

Samples of isotactic polypropylene with a high degree of crystallinity and pure α -phase have been investigated. One series was deformed by rolling, another one by uniaxial compression. Deformations up to true strains of 50 % have been achieved. The measurements were carried out in transmission by means of a simultaneous investigation by WAXS & SAXS from the same sample volume (Fig.1). The WAXS information has been analyzed in terms of the MXPA yielding the presence and density of dislocations, and the lamella (crystal size, while the SAXS signal was used to evaluate the thickness of lamellae and the distance in between them.

For the analysis of the profiles a particular algorithm had to be created, in order to fit a number of different parameters simultaneously [3]. Reliable evaluations were possible only by means of automatic determination of the starting values in a pre-fit. Results of the fit procedure are shown in Fig.2. The linear increase clearly gives high evidence for the presence of dislocations in polypropylene, with a density of $2 \times 10^{16} \text{ m}^{-2}$, increasing to $5 \times 10^{17} \text{ m}^{-2}$ with increasing plastic deformation (Fig.3.). These values are much higher than those usually found in metals, but they are consistent with the assumption that the mean free path of dislocations just equals the lamella (crystal) thickness [3, 4].

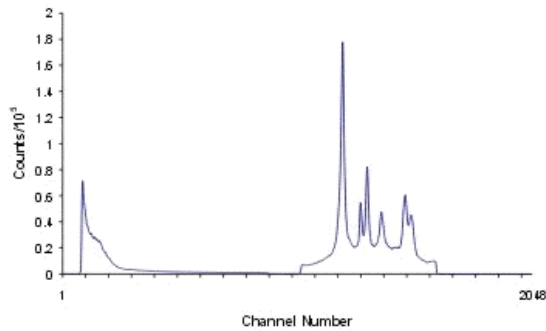


Figure 1. SAXS and WAXS spectra of an undeformed iPP sample.

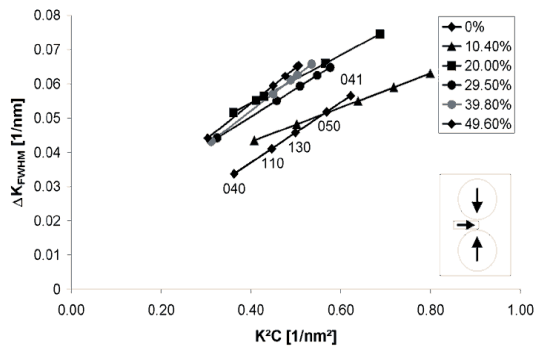


Figure 2. Modified Williamson-Hall plot of iPP after rolling deformation.

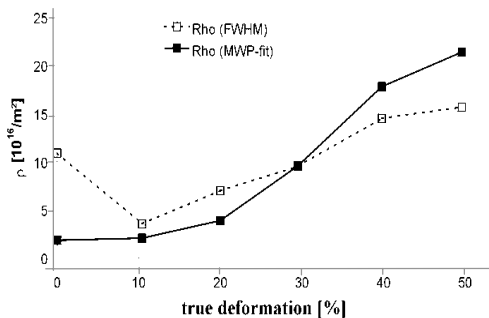


Figure 3. Evolution of dislocation density in cold rolled iPP as a function of true deformation, for two kinds of evaluation for the peak broadening effect observed.

References:

- [1] T. Ungár, A. Borbély: „The effect of dislocation contrast on X-ray line broadening: A new approach to line profile analysis“, *Appl. Phys. Lett.* **69**, 3173-3175 (1996)
- [2] T. Ungár, J. Gubicza, G. Ribárik and A. Borbély : „Crystallite size distribution and dislocation structure determined by diffraction profile analysis“, *J. Appl. Cryst.* **34**, 298 (2001)
- [3] A. Paris: “Application of the Bragg Profile Analysis for the determination of deformation induced dislocations in Polypropylene”, Diploma Thesis, University of Technology, Wien, and University of Vienna, Wien, Austria (2002)
- [4] H. Wilhelm, A. Paris, E. Schafner, S. Bernstorff, J. Bonarski, T. Ungar, M. J. Zehetbauer: “Evidence of dislocations in melt-crystallised and plastically deformed polypropylene”, paper accepted for presentation at the 13th Int.Conf. Strength of Materials (ICSMA 13), Budapest 2003, to be published in: *Mater.Sci.Eng.A*

SYNCHROTRON WAXS & SAXS STUDIES OF MICROSTRUCTURAL EVOLUTION DURING POST-YIELD DEFORMATION OF ISOTACTIC POLYPROPYLEN(PT.III)

E. Schafler¹, H. Wilhelm¹, S. Bernstorff², L. Tarkowski³, G. Ribarik⁴, M. Zehetbauer¹

1.) Institute of Material Physics, University of Vienna, Vienna, Austria

2.) Sincrotrone Trieste, Trieste, Italy

3.) Institute of Metallurgy and Materials Science, Polish Academy of Sciences, Krakow, Poland

4.) Department of General Physics, Eötvös University Budapest, Budapest, Hungary

Like in the preceding proposal [1], the task of this session was to verify the mechanisms of plastic deformation of semicrystalline polypropylene by means of the Multiple X-ray Profile Analysis (MXPA) [2], but this time by means of an in-situ investigation of the diffraction data during deformation which reflect the microstructural processes immediately as they arise in the sample under load. Moreover, samples have been pre-treated by a special thermal program (i) to increase crystallinity, in order to minimize mechanically undefined effects and also background scattering, both arising from the amorphous phase; ii) to obtain a material nearly without texture, which would have undesirable effects on the applied deformation process as well as on the evaluation by MXPA.

The deformation was achieved by a especially designed compression device, also providing very low strain rates and thus allowing to capture a full diffraction spectrum within a minimum range of strain. Fig.1 illustrates one of the measurement procedures. The sample has been deformed in steps to an absolute true strain of 75% and unloaded after each step. The line indicates the deformation cycling, and the full points represent the states where an X-ray spectrum has been recorded. It can easily be seen that the strain required to reach the stress level of the previous deformation step is quite high compared to metals which is due to enhanced effects of viscoelasticity occurring in iPP. Another interesting feature is reflected by the open circles in Fig.1, which indicate the stress drops immediately after stopping of deformation device. The effect seems to be connected to the re-arrangements of the polymer chains and the dislocations in the direction of the applied stress. These processes occur relatively slowly compared to the strain rate applied ($\sim 4 \times 10^{-3} \text{ s}^{-1}$).

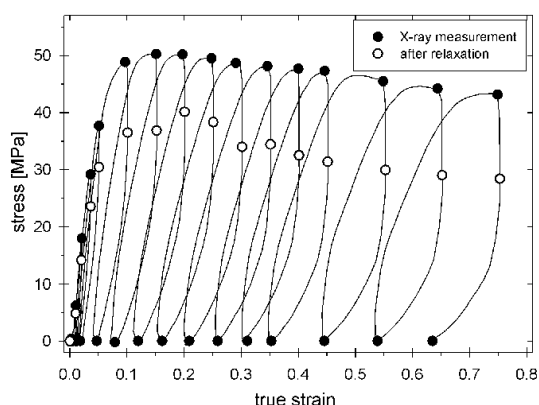


Figure 1. Stress - strain relationship of iPP. The full circles indicate the state of the X-ray measurement, the open ones the stress value after short relaxation time.

For the careful interpretation of the deformation induced microstructural changes, the elastic and the plastic part of total strain were determined by inspecting the residual strain after unloading. In Fig.2 the two strain components are plotted as a function of the total strain. The elastic strain dominates the plastic one in the lower deformation range up to 15%; later, the elastic strain levels off while the plastic strain keeps increasing. As a difference to metals, the elastic part seems to consist of three parts: i) the elastic distortion of the crystal lattice; ii) the

elastic component of the amorphous regions of the material; and iii) the rearrangement process of the polymer chains and/or the dislocations, which is assumed to be reversible, at least to a certain total strain.

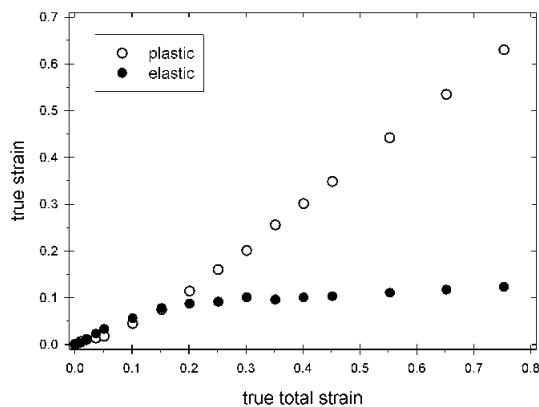


Figure 2. Elastic and plastic part of the strain as determined by the unloading experiment.

The microstructural data evaluated up to now confirm the analysis of strain given above. There have been observed shifts of several WAXS peaks as a function of the applied total strain which corresponds to the changes of lattice constant d shown in Fig. 3: After an increase of d until about 15% of deformation, a re-decrease of d is found with higher deformations where the plastic strain exceeds the elastic one. Further evaluations of the MXPA measurements will show whether the conclusions of the previous proposal [1] concerning the high density of dislocations and their related slip mechanisms will be confirmed from viewpoint of the actual in-situ observations.

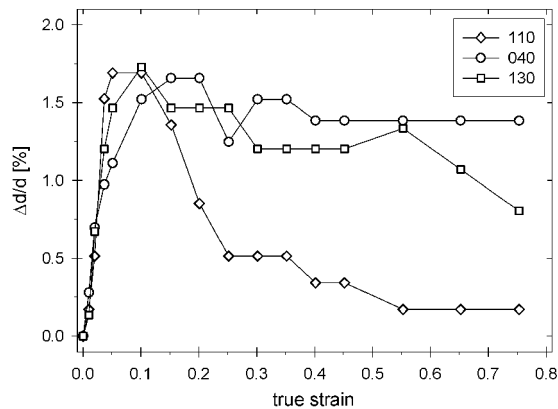


Figure 3. Peak shift in terms of relative lattice spacing changes as function of sum strain.

References:

- [1] H. Wilhelm et. al., Synchrotron WAXS & SAXS Studies of Microstructural Evolution During Post-Yield Deformation of Isotactic Polypropylen (pt. II), see previous report
- [2] T. Ungár, J. Gubicza, G. Ribárik, A. Borbély, „Crystallite size distribution and dislocation structure determined by diffraction profile analysis“, J. Appl. Cryst. 34, 298 (2001)

2. Life Sciences

MYOSIN MOTOR MOLECULAR CONFORMATION IS AFFECTED BY TONICITY

H. Amenitsch¹, C.C. Ashley², M.A. Bagni³, S. Bernstorff⁴, G. Cecchi³, B. Colombini³ and P.J. Griffiths²

- 1.) Institute of Biophysics and X-ray Structure Research, Austrian Academy of Sciences, Schmiedlstrasse 6, A-8042 Graz, Austria.
- 2.) University Laboratory of Physiology, Parks Road, Oxford, OX1 3PT, U.K.
- 3.) Dipartimento di Scienze, Università degli Studi di Firenze, Viale G.B. Morgagni 63, Firenze, I-50134, Italy.
- 4.) Sincrotrone Trieste, Area Science Park, Basovizza/TS, I-34012, Italy.

Myosin motors are transducers of the chemical free energy of ATP hydrolysis into mechanical work, which is performed by myosin translation along filaments of G-actin. Linear molecular motors (i.e. dynein, kinesin and myosin) are involved in cell division, directional transport of intracellular organelles, exo-, endo- and pinocytosis, sound transduction into electrical signals in the ear, and the contraction of all forms of muscle tissue. 17 classes of myosin motor have been identified, but myosin II (responsible for all muscle contractility) has the unique advantage that it aggregates into highly ordered filaments. In skeletal muscle, these ‘thick’ filaments overlap ‘thin’ (actin) filaments in a hexagonal array, giving a quasi-crystalline structure and enabling simultaneous collection of X-ray diffraction and mechanical data from a working population of myosin motors. The subfragment 1 (S1) moiety of myosin is sufficient to produce motor activity, and is composed of a ‘motor domain’ bearing the actin and ATP binding sites, and a 9nm long ‘lever arm’, which is proposed to tilt during the motor power stroke [1], producing ca. 4-10nm translational movement or 2-4pN of force.

The meridional X-ray reflection (M_3) originates from the 3-fold helical projection of S1 ‘crowns’ along the thick filament backbone. Its intensity (I_{M_3}) detects changes in S1 structure during the power stroke, and its behaviour during the synchronized power stroke, which accompanies a step change in actin-myosin overlap, is consistent with a change in lever arm tilt. At 4°C, I_{M_3} is maximal for a 0.8nm increase in overlap ($I_{M_3 \text{ max}}$), produced by shortening of activated muscle accompanying a quick (<0.5ms) release, suggesting that the lever arm tilt after such a release gives rise to the most concentrated axial mass projection of the S1 moiety [2]. We have used this property of I_{M_3} to define S1 structure in different states. We studied changes in I_{M_3} in tibialis anterior fibres from *Rana temporaria* during sinusoidal perturbation of fibre length and found that, at high frequencies (>1kHz), the I_{M_3} response was sinusoidal. At lower frequencies, I_{M_3} was deformed during the shortening phase of the oscillations. This behaviour may arise because, in addition to the effect of the power stroke, lever tilt varies with load in the manner of an elastic element. Instantaneous elastic distortion of S1 then dominates the I_{M_3} signal at high frequencies (>1kHz) because there is insufficient time for the power stroke tilting to occur. At lower frequencies, I_{M_3} contains both elastic and power stroke components to lever arm tilting, increasing the total motion of the arm sufficiently for it to pass through its maximum I_{M_3} disposition, leading to I_{M_3} distortion. By simulation the I_{M_3} signal expected from the experimental force and length signals by a model of the molecular structure of S1, we could show that observed changes in I_{M_3} distortion as a function of frequency were consistent with this explanation, and we could determine the lever arm orientation during isometric contraction required to account for this sensitivity to frequency [3].

It could be argued that the presence of distortion is related to the power stroke event *per se*, and not to an increased lever domain displacement. To resolve this issue, we repeated the observations at high frequency (3kHz), where power stroke tilting is suppressed and I_{M_3} distortion is absent. We increased oscillation amplitude, and were able to show that I_{M_3} distortion could be restored, if the lever arm displacement were large enough, in the virtual

absence of the power stroke event. This finding supports the proposal that power stroke and elastic distortions of S1 both cause a change in lever disposition, and that these distortions are additive.

A rise in temperature from 4°C to 22°C increases tension developed by frog muscle 1.28 fold without change in fibre stiffness, i.e. increasing the load per S1 without recruitment of new S1 moieties. We found that I_{M3} deformation during oscillations increased with temperature, consistent with a shift in lever domain orientation towards its $I_{M3 \text{ max}}$ position when S1 exerts more force. We used our Fourier transform simulations of S1 to demonstrate that this increased distortion of I_{M3} signals could not arise from power stroke acceleration with temperature [4]. To confirm that this was not a specific feature of temperature changes, we examined the observation that force per S1 also varies with bathing medium tonicity. In hypertonic saline (1.4 fold standard tonicity), force is reduced as a result of water loss from the cells until osmotic pressure balance is restored across the cell membrane. At 12°C, there is substantial I_{M3} distortion during sinusoidal length oscillations at 1kHz. We therefore compared distortion in standard and hypertonic salines at this temperature in bundles of 2-4 intact muscle fibres from frog tibialis anterior muscle. Hypotonicity resulted in compression of the myofilament lattice (8%) and a rise in intracellular ionic strength (40%), both of which contributed to a fall in isometric tension (24%) without reduction in the fraction of working myosin motors, as assessed by bundle stiffness. Based on the increased I_{M3} distortion upon elevation of temperature, reduction of force per S1 in hypertonic saline would be expected to show the opposite effect; to move the lever arm further away from $I_{M3 \text{ max}}$ and thus reduce I_{M3} distortion. The effect was found to be present in all experiments (fig. 1). We also obtained preliminary observations under hypotonic conditions (0.8 fold standard tonicity), where force per S1 is increased, and obtained an increased I_{M3} distortion consistent with movement of the lever arm towards its $I_{M3 \text{ max}}$ disposition. These findings strongly support the conclusion of our temperature studies, i.e. that increased S1 force is accompanied by a shift in tilting of the lever arm towards its $I_{M3 \text{ max}}$ position.

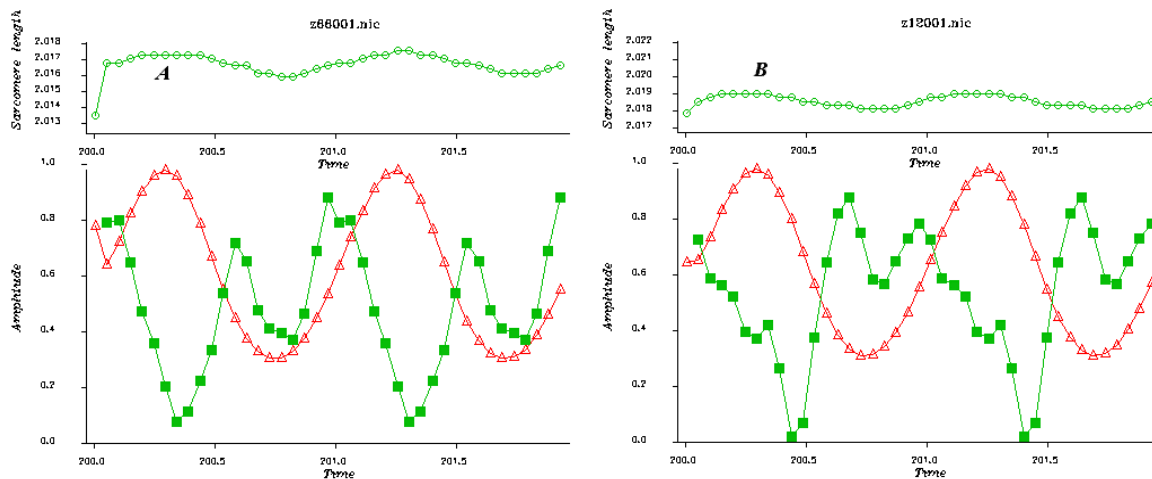


Figure 1. Sarcomere length (top panels), force (triangles) and I_{M3} (squares) during 1kHz sinusoidal oscillations applied at tetanic tension in isotonic (**A**) and hypertonic (**B**) saline. Distortion is apparent as a new intensity minimum at the point of minimum force, forming an intensity double peak during release. Temperature 12°C.

References:

- [1] I. Rayment, W.R. Rypniewski, K. Schmidt-Bäse, R. Smith, D.R. Tomchick, M.M. Benning, D.A. Winkelmann, G. Wesenberg and H.M. Holden. Three-dimensional structure of myosin subfragment-1: A molecular motor. *Science*, **261**: 50-58 (1993)
- [2] V. Lombardi, G. Piazzesi, M.A. Ferenczi, H. Thirlwell, I. Dobbie and M. Irving. Elastic distortion of myosin heads and repriming of the working stroke in muscle. *Nature*, **374**, 553-555 (1995).
- [3] M.A. Bagni, B. Colombini, H. Amenitsch, S. Bernstorff, C.C. Ashley, G. Rapp and P.J. Griffiths. Frequency dependent distortion of meridional Intensity changes during sinusoidal length oscillations of activated skeletal muscle. *Biophys.J.*, **80**: 2809-2822 (2001).
- [4] P.J. Griffiths, M.A. Bagni, B. Colombini, H. Ameritsch, S. Bernstorff, C.C. Ashley and G. Cecchi. Changes in myosin S1 orientation and force induced by a temperature increase. *Proc. Nat. Acad. Sci. USA.*, **99**: 5384-5389 (2002).

SELF ALIGNMENT OF LIPID FILMS STUDIED WITH SURFACE DIFFRACTION

H. Amenitsch¹, M. Rappolt¹, D. Grosso² and P. Laggner¹

1.) Institute of Biophysics and X-ray Structure Research, Austrian Academy of Sciences, Schmiedlstr. 6, A-8010 Graz, Austria

2.) Chimie de la Matière Condensée, UPMC - CNRS, 4 place Jussieu, 75005 Paris, France.

Self alignment of surfactant molecules has attracted considerable interest in manufacturing highly ordered mesoporous films and high quality surface coatings, e.g. [1]. We wanted to adapt this method for lipid films with high quality in terms of homogeneity, optical quality and perfection of the nanostructure. An important prerequisite to exploit this technique is the discovery of the pathway of self-assembly process in lipids on surfaces. Therefore, a clean silicon-wafer was covered with a lipid solution and during the evaporation of the solvent the self-assembly under controlled humidity conditions was studied with time resolved surface diffraction with the substrate kept at constant grazing angle. As solvents ethanol, isopropanol and chloroform have been used and various lipids and lipid mixtures have been studied. The relative humidity was changed in the range from 5% to 80%.

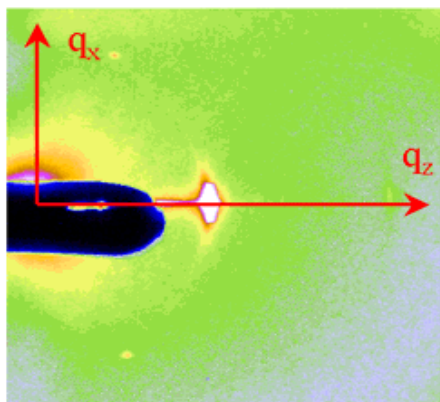


Figure 1. A static diffraction pattern of Soya-PC after the self assembly process at 85 % relative humidity depicting the in plane diffraction peaks of the hexagonal phase.

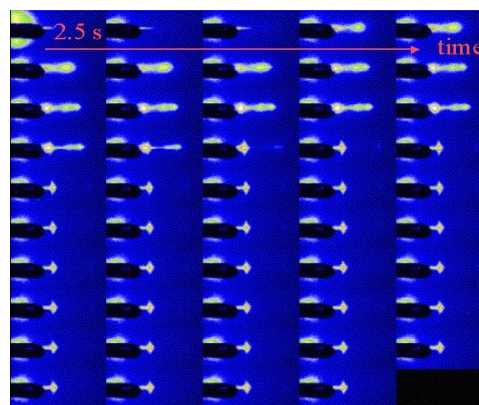


Figure 2. Time sequence of surface diffraction images measured with Soya-PC after covering with lipid solution (solvent ethanol) at 85% relative humidity. The sampling time for each diffraction image was 2.5 s.

Interestingly, although the first steps in general pathway of the surfactants assembly are conserved, i.e., isotropic scattering is followed by the self assembly of a lamellar phase and its shrinkage (see fig. 2), in some cases the final lipid structure resulted mainly in non lamellar phases (hexagonal or 3D-mesh). This is clearly different to the known lyotropic phase behaviour and is attributed to the residual of non evaporated solvent.

In the future we will concentrate to optimise the deposition parameters - such as choice of solvent, relative humidity, temperature, evaporation speed, and removal of the residual solvents in vacuum - for manufacturing high quality homogenous lipid films, and in particular lipid mixtures.

References:

[1] Brinker C.J., Y.F. Lu, A. Sellinger, and H.Y. Fan. 1999. Evaporation-induced self-assembly: Nanostructures made easy. *Adv. Materials* 11, 579.

ANISOTROPIC COMPRESSIBILITIES OF GUANOSINE MONO-PHOSPHATE FOUR-STRANDED HELICES BY HIGH-PRESSURE SYNCHROTRON X-RAY DIFFRACTION

P. Ausili¹, M. Pisani¹, H. Amenitsch², S. Bernstorff³, M. Kriechbaum² and P. Mariani¹

1.) Istituto di Scienze Fisiche and INFN, Università Politecnica delle Marche, Via Ranieri 65, I-60131 Ancona, Italy

2.) Institute of Biophysics and X-ray Structure Research, Austrian Academy of Sciences, Graz, Austria

3.) Sincrotrone Trieste S.C.p.A., Strada Statale 14, km 163.5, I-34016 Basovizza (Trieste), Italy

An interesting case of self-recognition and self-assembly process concerns guanine, which, unique among the nucleic acid bases, forms a variety of non-B-DNA conformations such as quadruplex structures [1-5]. This property is related to the arrangement of H-bond donor and acceptor groups in guanine and is essential for genome integrity and appears to play an important role in cellular aging and cancer [5,6]. As shown in Figure 1, planar tetramers result from the assembling of four guanines in a Hoogsteen-bonded fashion, while four-stranded helices form by the regular stacking of tetramers (tetrads are stacked perpendicular to the column axis at the typical distance of 3.4 Å, rotated with respect to each other of about 30° [3,5,7,8]). Helices have been recognized to lead to columnar lyotropic phases of hexagonal (H) and cholesteric (Ch) type [3,8,9].

To address questions related to the preferential hydration and to the role of lateral forces [10], high pressure effects on the structural properties of GMP helices in the hexagonal phase were examined and the compressibility measured by X-ray diffraction.

Hydrated samples were prepared by mixing the GMP (Sigma, 99 % purity) with the required quantities of freshly bidistilled water or aqueous solution of KCl (1 M and 2 M). Final mixtures (GMP weight fractions c ranging from 0.9 to 0.5) were left for at least two days at 25°C to avoid inhomogeneity. Diffraction experiments were performed at the SAXS beamline at ELETTRA Synchrotron (Trieste, Italy) with $\lambda = 1.54$ Å and $0.03 < Q < 0.6$ Å⁻¹. The wide-angle X-ray scattering detector was used to monitor diffraction patterns in the Q -range from 0.7 to 2.5 Å⁻¹. Pressure cells with diamond windows, which allow to measure diffraction patterns at hydrostatic pressures up to 3 kbar were used. Particular care has been taken to check for radiation damage and for equilibrium conditions. Measurements were repeated several times at the same constant pressure to account for stability in position and intensity of Bragg peaks. Accordingly, samples were gently compressed at a rate of 0.5-2 bar/s to ensure the onset of equilibrium conditions. The diffraction patterns were collected at 25°C.

In each experiment, a number of reflections were observed and their spacings measured following usual procedures [3]. Typical X-ray diffraction patterns are reported in Figure 2: the low angle peaks (from 2 to 5) can be index in a 2D hexagonal lattice and the unit cell dimension, a , (i.e., the lateral interaxial distance between the helices) was then derived as a function of pressure. The narrow band observed in the wide-angle region is the indication of the columnar nature of the H phase: this reflection is indeed related to the tetramer stacking [3] and from its position the distance between the neighboring tetrads, b , can be obtained. No extra low-angle peaks were observed, indicating the absence of smectic-like order (no long-range column-column correlation of the tetramer position exists). It should be noticed that at all concentrations, the interaxial distance increases as a function of pressure, while the tetramer repeat distance reduces. A similar behavior was observed in KCl.

From structural data, axial (1D) and lateral (2D) compressibilities, $\beta_{1D} = -1/b$ (db / dP) and $\beta_{2D} = -1/\sigma$ ($d\sigma / dP$) (where $\sigma = a^2 \sqrt{3}/2$), were calculated. The results, reported in Figure 3 (c,d), deserve some comments: *first*, lateral compressibilities are negative and for increasing concentrations converge to very low (yet negative) values. Since experiments are performed

at constant concentration, this suggests that during compression a change in the local sample composition occurs, a redistribution of water from the axial to the lateral inter-helical region taking place. This is confirmed by the β_{2D} dependence on water concentration. *Second*, the lateral compressibility is rather independent of the ionic strength, suggesting that the role played by electrostatic forces is not primary. *Third*, stacking compressibilities are positive, rather small (as compared with water data, which are in the order of 0.045 to 0.03 kbar⁻¹ [11]) and strongly dependent on KCl concentration. The suggested K/Na ion exchange from the solution to the cavity between guanine tetrads could determine an increase of the aggregate rigidity. *Fourth*, da/dP of few tenths of Å per kbar can be derived from data in Figure 3; these values are significantly different from those observed in lipid direct and inverse phases, where da/dP of -0.2 Å/kbar or from 4 to 10 Å per kbar were measured, respectively [12,13]. Such results confirm that a net release of water from the axial to the lateral region should occur during compression, enforcing the original hypothesis that in guanosine phases water separates into different regions (of different activity) [10]. A detailed analysis of all interactions involved is not possible and then the present analysis is not exhaustive; however, the authors are persuaded that the reported experimental data might help the understanding of the peculiar self-assembling properties of guanosine and the use of theoretical approaches to disentangle the different free energy contributions in further analysis.

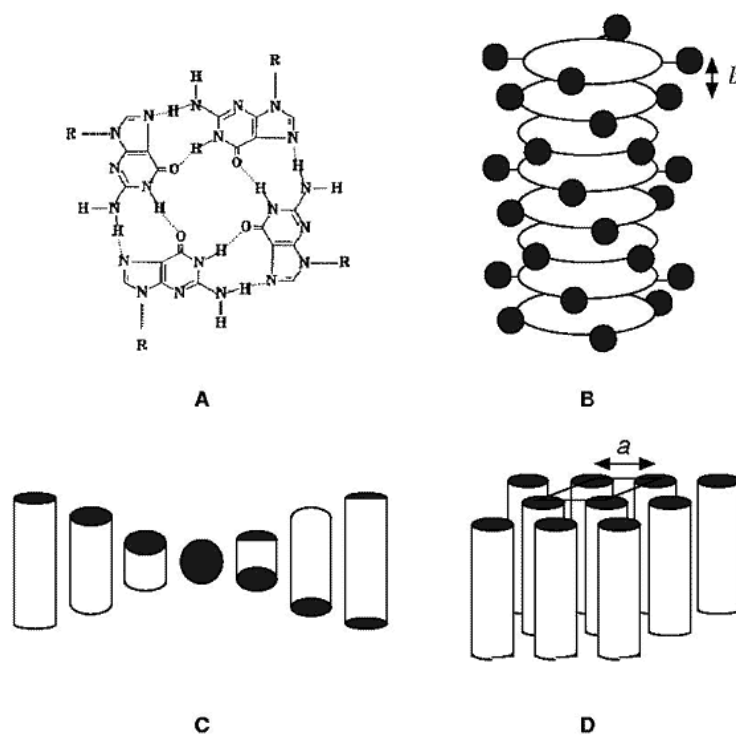


Figure 1. Structural models for the guanosine self-assembling. (A), guanine quartet in the Hoogsteen mode; (B), four-stranded helix; (C) cholesteric and (D) hexagonal phases.

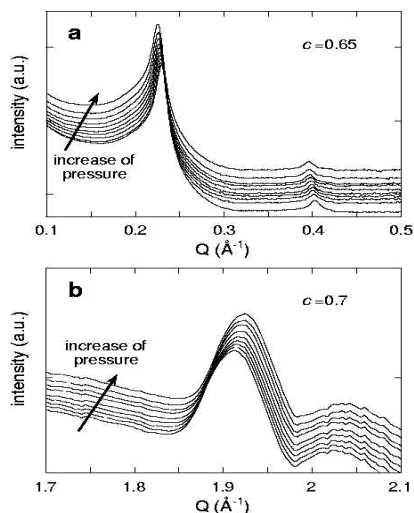


Figure 2. X-ray diffraction profiles obtained from GMP samples in water. (a) low-angle profile, $c=0.65$. (b) high-angle profile, $c=0.7$. Spectra every 200 bar are shown.

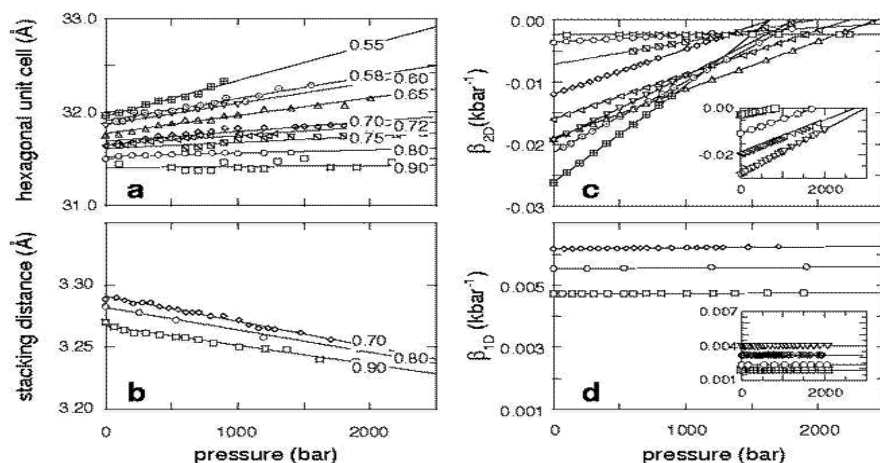


Figure 3. Pressure dependence of (a) hexagonal unit cell, (b) tetramer repeat distance, (c) β_{2D} and (d) β_{1D} compressibilities. Data refer to samples in water, while the inserts in (c) and (d) show compressibilities in 1 M KCl. GMP concentrations c are reported in the graph. Lines are guides to the eye.

References:

- [1] M. Gellert, M.N. Lipsett and D.R. Davies, P.N.A.S. USA **48**, 2013 (1962)
- [2] W. Saenger, Principles of Nucleic Acid Structure (Springer-Verlag, Heidelberg, 1984)
- [3] G. Gottarelli, G.P. Spada and P. Mariani, in Crystallography of Supramolecular Compounds, edited by Tsoucaris & Atwood (Kluwer Academic Publ., Dordrecht, 1996) p. 307.
- [4] D.E. Gibert and J. Feigon, Curr. Op. Struct. Biology **9**, 305 (1999)
- [5] T. Simonsson, Biol. Chem. **382**, 621 (2001)
- [6] J.L. Mergny et al., Anti-Cancer Drug Design **14**, 327 (1999)
- [7] L.Q. Amaral, R. Itri, P. Mariani and R. Micheletto, Liquid Crystals **12**, 913 (1992)
- [8] P. Ausili, H. Strey and P. Mariani (unpublished)
- [9] P. Mariani, C. Mazabard, A. Garbesi and G. P. Spada, J. Am. Chem. Soc. **111**, 6369 (1989); H. Franz et al., Phys. Rev. E, **50**, 395 (1994); G. Gottarelli et al., Biopolymers (1997).
- [10] P. Mariani and L. Saturni, Biophysical J. **70**, 2867 (1996); P. Mariani, F. Ciuchi and L. Saturni, ibid. **72**, 2867 (1998).
- [11] Roark's Formulas for Stress & Strain (sixth edn), edited by W.C. Young (McGraw-Hill, Inc., New York 1989).
- [12] M. Pisani, S. Bernstorff, C. Ferrero and P. Mariani, J. Chem. Phys. B **54**, 5840 (2001)
- [13] M. Pisani, Ph.D. thesis, Ancona University, 2001.

APPLICATION OF TIME – RESOLVED SMALL ANGLE X – RAY SCATTERING COMBINED WITH MECHANICAL TESTING TO STUDY DEFORMATION IN TYPE I TENDON COLLAGEN

H.S. Gupta^{1,2}, K. Misof¹, S. Bernstorff³, P. Roschger¹, B. Aichmayer¹, A. Valenta^{1,2}, M. Weber^{1,2}, K. Klaushofer², and P. Fratzl¹

- 1.) Erich Schmid Institute of Materials Science, Austrian Academy of Sciences, A8700 Leoben, Austria
- 2.) Ludwig Boltzmann Institut of Osteology, 4th Medical Department, Hansch Hospital & UKH-Meidling Hospital, Vienna, Austria
- 3.) Sincrotrone Trieste S.C.p.A, Strada Statale 14, I-34012 Basovizza, Trieste, Italy

Type I collagen, the primary organic component in bone and tendons, consists of fibrils of collagen molecules in a viscous proteoglycan rich matrix, which are arranged in fiber bundles and fascicles, and form the entire organ by means of a hierarchical structure [1]. Not much is known about the deformation mechanisms during application of external loading, in particular the means by which the fibrils in the composite disaggregate or break apart on the application of external stresses [2,3]. Such information is of basic scientific interest in the mechanical and structural modeling of collagen. Due to the axially periodic electron density distribution in the collagen fibril, arising from the gap – overlap stacking of collagen molecules [4], a Bragg diffraction pattern is generated in the low angle regime ($2\theta < 2$ degrees), with a peak separation of $2\pi/D$ where $D \cong 67 \text{ nm}$ is the axial period (Figure 1). If the n^{th} order peak width b_n transverse to the fibril axis direction is plotted as a function of peak order n , in the form $b_n = b_0 + a n$ (all widths in detector pixels), then the transverse width of the axially crystalline domains w and the *fibril tilt angle* α arising from the mosaic spread can be directly determined by means of the following equations : $w = \frac{2\sqrt{2}}{\delta q b_0}$, and $\alpha = a (180 / \pi) / C$. Here

δq is the wave vector step per detector pixel, and C is the number of pixels per collagen order.

We used the facilities of the Austrian SAXS beam line at ELETTRA Sincrotrone Trieste, in conjunction with a self – built mechanical testing apparatus [5], for time – resolved SAXS and WAXD diffraction measurements on native collagen from rat tail tendon, during constant strain rate and cyclic straining measurements. The primary aim was to determine if there occurred a change in w or α with either increased strain on the tendon or following cyclic fatigue. We also measured the effect of age and increased intrafibrillar crosslinking on the mechanical properties, by comparing immature collagen from 6 week old rats and more highly crosslinked collagen from mature 17 week old rats [2].

Figure 2 shows the completely different stress strain curves obtained from immature versus mature collagen, with the mature collagen exceeding the immature in modulus and strength. In contrast the immature collagen exhibits a large plateau – type region where further extension occurs with essentially no change in applied force, thereby increasing the fracture strain, at the cost of a decrease in the strength. A typical example of the change in effective lateral width w and fibril tilt angle α with applied strain is shown in Figure 3. We designate the regions in the stress – strain plot as toe – heel, linear, and finally the damage region, where fracture and defibrillation processes are expected to become important. The effective width w decreases by nearly a factor of 2, from around 420 nm to the typical diameter of a fibril (200 to 250 nm) in the toe – heel region and start of the linear region. An unexpected result is the constancy of w in the linear and damage regions, suggesting that the ultrastructural mechanisms leading to fracture in collagen are operating at length scales larger than 200 to

400 nm. It is noted that the above is the result of a constant strain rate measurement at extremely slow strain rates $de/dt = 7.5 \times 10^{-5} \% \cdot s^{-1}$, during which the viscous shear between the fibrils is expected to play an important part [6]. In contrast, the tilt angle α shows a constant decrease over the entire heel *and* linear region of the tendon. Indeed, Figure 3c appears as an inverted version of the stress versus strain graph in Figure 3a. Wide – angle X – ray scattering patterns of the lateral molecular packing both support and add complementary information to this picture (data not shown), where the molecules are observed to become more highly aligned along the fibril axis with applied strain, but not significantly squeezed together. This implies that the initial reduction in width is not related to Poisson contraction of individual fibrils.

These initial results demonstrate the power of time – resolved SAXS combined with *in – situ* tensile testing to provide insight into the relevant deformation mechanisms in biological connective tissues. Further analysis is in progress, to determine the effect of cyclic loading, variable strain rate, and increasing tissue maturity on the changes in effective width w and tilt angle α with applied strain.

HG is partially supported by the Fonds Wissenschaftlicher Forschung (FWF 14331).

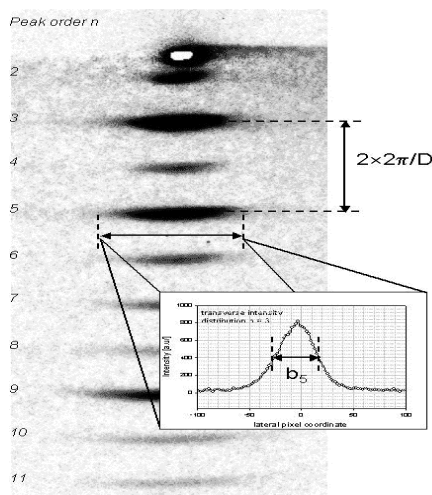


Figure 1. Diffraction pattern arising from the $D \cong 67 \text{ nm}$ periodicity in electron density, along the fibril axis, showing the different peak orders. The transverse intensity pattern and width b_n of a typical peak ($n = 5$) are shown in the inset graph.

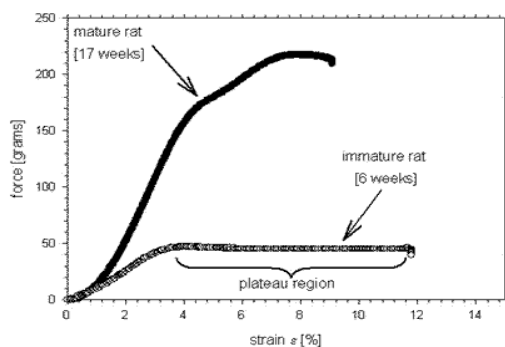


Figure 2. Force versus strain plots for immature (6 week old) and mature (17 week old) tendon, showing the increase in strength and modulus of rat tail tendon with increasing age and increasing degree of crosslinking. Immature collagen shows a plateau in the stress – strain plot for $\epsilon > 4 \%$, which is not observed in mature tissue.

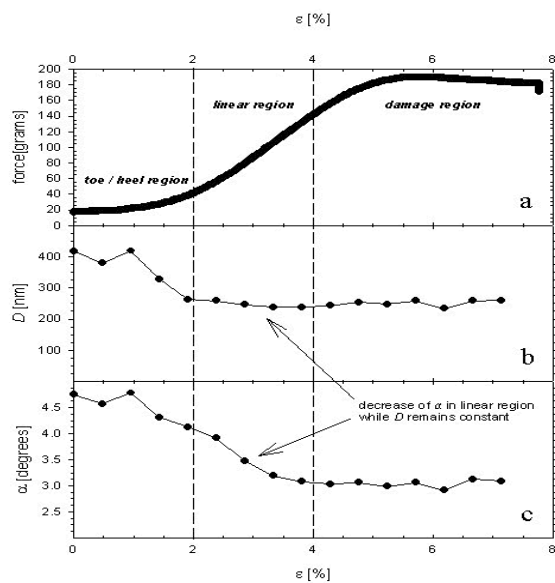


Figure 3. (a) Stress versus strain plot for mature tendon tested at strain rate $d\varepsilon/dt = 7.5 \times 10^{-5} \% \cdot s^{-1}$. The toe – heel ($\varepsilon < 2\%$), linear ($2\% < \varepsilon < 4\%$), and damage ($\varepsilon > 4\%$) regions are indicated. (b) Decrease of the effective diameter of the coherently scattering unit (giving rise to the axial electron – density periodicity) with applied strain. (c) Decrease of the fibril tilt angle α with applied strain.

References:

- [1] V. Ottani, D. Martinin, M. Franchi, A. Ruggeri and M. Raspanti; Hierarchical structure in fibrillar collagens; *Micron* **33**, 587-596 (2002).
- [2] J. Kastelic and E. Baer; Deformation in tendon collagen; *Symp. Soc. Exp. Biol.* **34**, 397-435 (1980).
- [3] P. P. Purslow, T. J. Wess and D. W. L. Hukins; Collagen orientation and molecular spacing during creep and stress-relaxation in soft connective tissues; *J. Exp. Biol.* **201**, 135-142 (1998).
- [4] A. J. Hodge and J. A. Petruska; Recent studies with the electron microscope on ordered aggregates of the tropocollagen molecule, in *Aspects of Protein Chemistry* (G. N. Ramachandran, ed.), 289 – 300 (1963), Academic Press, London.
- [5] K. Misof, G. Rapp and P. Fratzl; A new molecular model for collagen elasticity; *Biophys. J.* **72**, 1376-1381 (1997).
- [6] P. Fratzl, K. Misof, I. Zizak, G. Rapp, H. Amenitsch and S. Bernstorff; Fibrillar structure and mechanical properties of collagen; *J. Struct. Biol.* **122**, 119-122 (1998).

INFLUENCE OF SHEAR ON CRYSTALLIZATION IN EMULSION

D. Kalnin¹, O. Schaffer², G. Keller¹, H. Wille³, H. Amenitsch⁴ and M. Ollivon¹

1.) Equipe Physico-Chimie des Systèmes Polyphasés, F-92296 Châtenay-Malabry,

2.) Nestlé Research Center, PO Box 44, CH-1000 Lausanne 26,

3.) Nestlé S.A., PTC, rue Charles Tellier 60000 Beauvais, France,

4.) Institute of Biophysics and X-Ray Structure Research, Graz, Austria

Triacylglycerols, TAGs, also called triglycerides, are the main constituents of fats. TAGs find a widespread application in form of food or pharmaceutical emulsions. Biopreservation of such emulsions implies their storage at low temperature where TAGs are at least partly crystallized. In these conditions, TAGs display a monotropic polymorphism which makes the study of thermal and structural properties of the fats really complex and frequently prevents their use. Monitoring of crystallisation in emulsion by X-ray diffraction and DSC has been demonstrated recently for aerated emulsions [1]. How does industrial process affect crystallisation is addressed in this research by examining the influence of shear on emulsion behaviour. The experimental Couette cell enabling data acquisition of SAXS - WAXS calorimetry under shear conditions from a quartz glass capillary containing emulsion is shown below. A model O/W emulsion with mean diameter droplets of 0.5 μ m resulting from high pressure homogenisation of 20% vegetable fat in the presence of 2 % of sodium caseinate was used. The influence of shear on TAGs crystallization was observed by comparing thermal and structural behaviours recorded on cooling identical emulsion samples with and without shear. Figures 2A and B respectively show the crystallization behaviour of emulsion as a function of temperature during cooling at 4K/min. under no shear and under shear. SAXS pattern recorded for 1 min at $T = 3^{\circ}\text{C}$ shows the formation of a single crystalline α form characterized by an hexagonal lateral packing of the TAG chains (4.15Å WAXS line) and a 2L stacking of the whole molecule (43Å SAXS line) under no shear while two crystalline forms are observed from 5.5 $^{\circ}\text{C}$ under shear. The second variety (β' form) only observed under shear is characterized by an orthorhombic subcell with lines at 4.15 and 3.8 Å and a 2L stacking of 38.2 Å period corresponding to a tilt of about 25 $^{\circ}$ of the chains over the perpendicular to the stacking plane. In both cases, molecular stacking is observed by SAXS before any lateral chain packing is seen by WAXS. Future aims of our work are to elucidate the influence of the interface constitution affected by concentration of emulsifier upon TAG crystallization in emulsion in the presence of shear as well as modification of the Couette cell to allow quantitative DSC measurements.



Figure 1. Photo of the Couette cell.

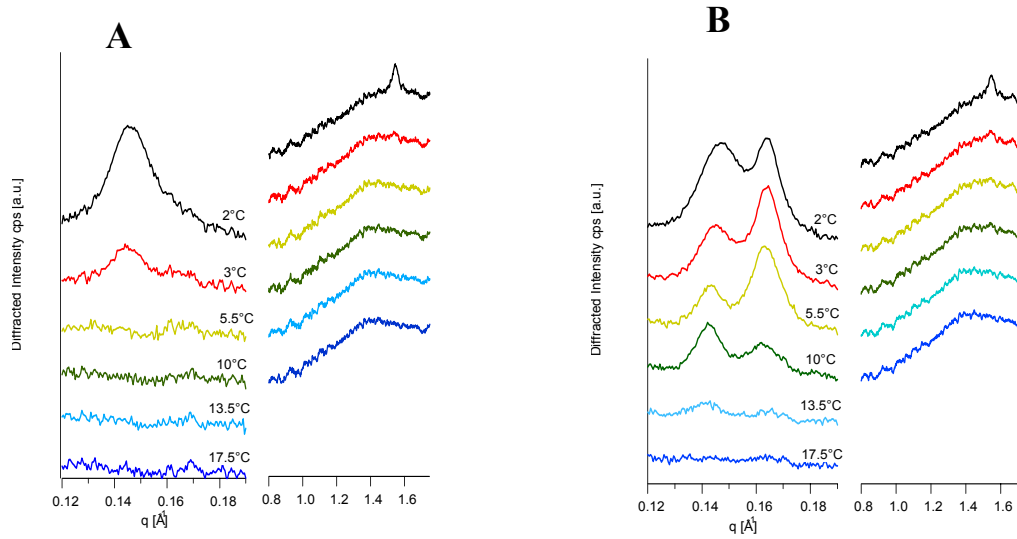


Figure 2. Crystallization behaviour of TAGs during a cooling ramp. For details see text.

References:

- [1] Kalnin D. G. Garnaud, H. Amenitsch & M. Ollivon, Monitoring fat crystallization in aerated food emulsions by combined DSC and TRSXR, *Food Res. Int.*, 35 (2002) 927-934

UNBINDING TRANSITION OF LIPID MULTIBILAYERS

G. Pabst, B. Pozo-Navas, F. Proßnig, H. Amenitsch and K. Lohner

Austrian Academy of Sciences, Institute of Biophysics and X-ray Structure Research, Schmiedlstrasse 6, A-8042 Graz, Austria

We have studied the discontinuous unbinding transition of lipid bilayer stacks composed of zwitterionic 1-palmitoyl-2-oleoyl-phosphatidylethanolamine (POPE) and negatively charged 1-palmitoyl-2-oleoyl-phosphatidylglycerol (POPG) (molar ratio = 9:1) by x-ray diffraction (Fig. 1). The unbinding is reversible and coincides with the main ($L_\beta \rightarrow L_\alpha$) transition of the lipid mixture.

The diffraction patterns in the L_β phase (Fig. 1A, C) are characterized by 3 lamellar quasi-Bragg peaks, typical for multilamellar lipid aggregates. However, the peaks are very broad. The large peak width, which is characteristic of a system with a short scattering correlation length, is an indication that the bilayers are weakly bound. Further, the large lamellar d -spacing of 125 Å shows that the system is in a highly swollen state. Upon heating to 26°C the quasi-Bragg peaks disappear and the diffraction pattern corresponds to diffuse scattering from uncorrelated bilayers. The wide-angle diffraction patterns, corresponding to the in-plane packing of the hydrocarbon chains (Fig. 1, insets), confirm that the system is in the L_β phase at 20°C (A and C) and in the fluid phase at 26°C (B). The unbinding itself appears to be driven by an abrupt increase in steric repulsion resulting from increased thermal undulations of the bilayers upon entering the L_α phase. This observation provides direct experimental evidence for much theorized unbinding transition in bilayer stacks [1].

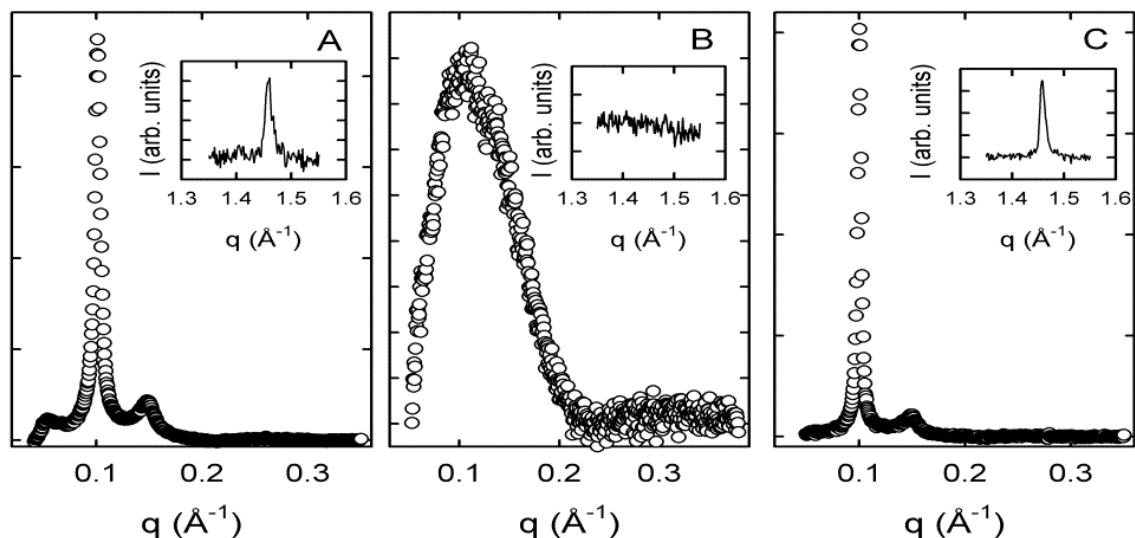


Figure 1. Unbinding transition upon heating through the main phase transition ($T_M \sim 24^\circ\text{C}$) of a POPE/POPG (9:1 mol/mol) mixture (5 wt.%) in Na-phosphate buffer (pH 7.4) containing 100 mM NaCl. Diffraction pattern (A), taken at 20°C corresponds to a weakly bound multibilayer system. Panel (B) shows the system at 26°C, where interbilayer positional correlations are lost. The system returns to its loosely bound state after cooling back to 20°C (C). The corresponding wide-angle diffraction patterns showing the in-plane order of the hydrocarbon chains are given in the insets.

References:

- [1] R. Lipowsky and S. Leibler; Unbinding Transitions of Interacting Membrane; Phys. Rev. Lett. **56**, 2541-2545 (1986)

HYDROSTATIC PRESSURE EFFECTS ON HEXAGONAL PHASES OF LIPID MIXTURES

L. Paccamiccio¹, M. Pisani², G.M. Di Gregorio¹, H. Amenitsch³, S. Bernstorff⁴ and P. Mariani¹

1.) Istituto di Scienze Fisiche, Università Politecnica delle Marche, Ancona, Italy

2.) Dipartimento di Fisica e Ingegneria dei Materiali e del territorio, Università Politecnica delle Marche, Ancona, Italy

3.) Institute of Biophysics and X-Ray Structure Research, Austrian Academy of Sciences, Graz, Austria

4.) Sincrotrone di Trieste, Area Science Park, Trieste, Italy

The aim of this work is the analysis of the structural properties, phase behavior and energetic of a DOPE - DOPC lipid mixture equilibrated in excess of water in the presence of tetradecane (DOPE, L- α -dioleoyl phosphatidylethanolamine; DOPC, L- α -dioleoyl phosphatidylcholine). The analysis was performed using high pressure synchrotron X-ray diffraction.

Samples were obtained by combining the appropriate amounts of the component lipids, dissolved in chloroform, with DOPC molar fraction (X_{dopc}) ranging from 0 to 0.75. The solvent was evaporated and the mixtures were prepared in excess of water after the addition of tetradecane, which is known to stabilize hexagonal phases characterized by small curvatures at the water-lipid interface[1]. Diffraction experiments were performed at the SAXS beamline at ELETTRA Synchrotron (Trieste, Italy) with $\lambda = 1.54 \text{ \AA}$ and $0.03 < Q < 0.6 \text{ \AA}^{-1}$. The wide-angle X-ray scattering detector was used to monitor diffraction patterns in the Q -range from 0.7 to 2.5 \AA^{-1} . Pressure cells with diamond windows, which allow to measure diffraction patterns at hydrostatic pressures up to 3 kbar, were used. Particular care has been taken to check for radiation damage and for equilibrium conditions. Measurements were repeated several times at the same constant pressure to account for stability in position and intensity of Bragg peaks. Accordingly, samples were gently compressed at a rate of 0.5-2 bar/s to ensure the onset of equilibrium conditions. The diffraction patterns were collected at 25°C.

At all the investigated concentrations, the X-ray diffraction profiles confirm the presence of the inverse hexagonal phase at room temperature and at ambient pressure. As expected, in the presence of DOPC the hexagonal unit cells are rather large (if compared to the 68 \AA observed in DOPE in excess of water). For each mixture, a series of diffraction patterns were measured as a function of pressure, from 1 bar to 2 Kbar, with step of 100 bar. In Figure 1, it can be observed that pressure induces the $H_{II} - L_{\alpha}$ phase transition [2]. Under compression, both the hexagonal and lamellar unit cells are detected to increase, as shown in Figure 2: in particular, the pressure dependence is linear. Indeed, this suggests that pressure induces a continuous change in shape of the lipid molecules due to the increase of the chain order parameter [3]. Note that Figures 1 and 2 refer to a sample with $X_{\text{dopc}}=0.17$, but all the other samples show the same behavior.

Three results should be noticed: *first*, as the ratio DOPC/DOPE increases, the pressure at which the $H_{II} - L_{\alpha}$ phase transition occurs decreases (see Figure 3). In the case of $X_{\text{dopc}}=0$, the phase transition occurs at 1800 bar, while for $X_{\text{dopc}}=0.75$ the lamellar phase forms at 400 bar. This behavior confirms the tendency of DOPC to form lamellar phase. *Second*, the L_{α} unit cell dimension (measured at the phase transition) shows a strong dependence on the lipid composition of the mixture (see Figure 4), suggesting that changes in lipid hydration also occurs during compression. Noteworthy is the comparison between the lamellar and the hexagonal unit cells: both increase as DOPC is added to the mixture, even though the hexagonal cell shows a larger increase than the lamellar one (see again Figure 4). This point should be further investigated. *Third*, a general effect on the molecular characteristic of the

hydrostatic pressure can be derived: at all the investigated concentration, high pressure increases the thickness of the hydrocarbon lipid layer, while the area at the lipid-water interface decreases: as a consequence, the curvature of the polar-apolar interface reduces so that the lamellar phase becomes more stable.

The analysis of the energetic contributions that provide the stabilization of the two lipid phases is still in progress.

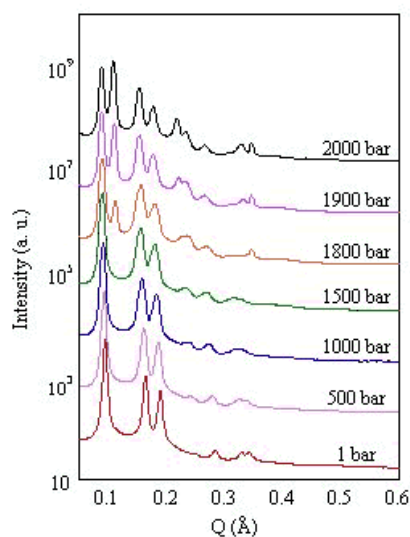


Figure 1. Low-angle X-ray scattering profiles from DOPE/DOPC mixture of molar fraction $X_{dopc}=0.17$ measured at different pressure.

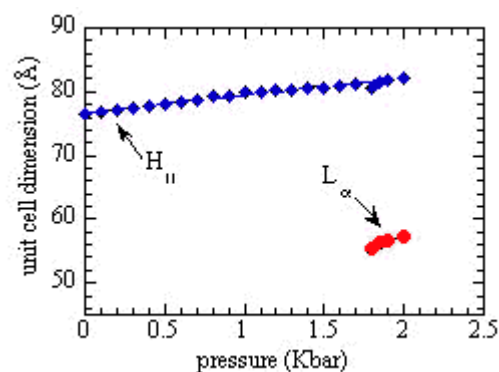


Figure 2. Pressure dependence of the unit cell dimension of the inverse hexagona H_{II} (squares) and lamellar L_{α} (circles) phases of the DOPE/DOPC mixture of molar fraction $X_{dopc}=0.17$.

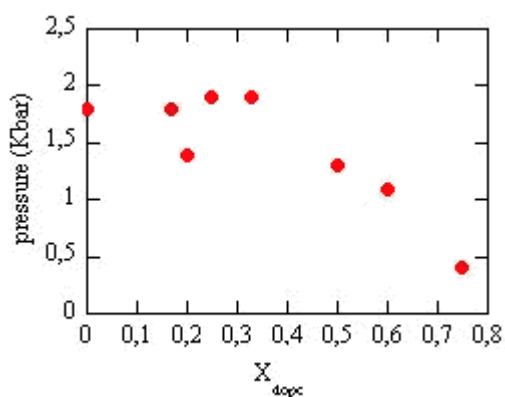


Figure 3. Pressure dependence of the H_{III} - L_{α} phase transition on the DOPE/DOPC molar fractions.

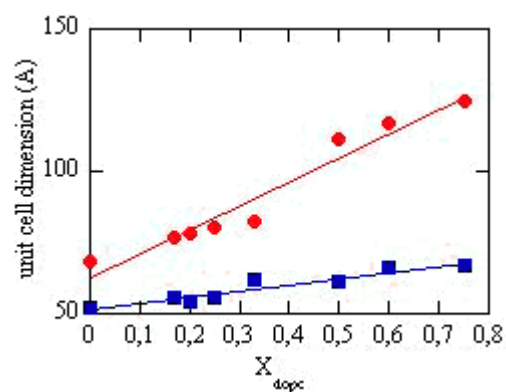


Figure 4. The unit cell dimension for both the hexagonal and lamellar phases is reported as a function of pressure. The values for the lamellar phase are referred to the phase transition pressure.

References:

- [1] R.P., Rand, N.L., Fuller, S.m., Gruner, V.A., Parsegian. *Biochemistry*. **29**(1): 76-87, 1990.
- [2] M. Pisani, T. Narayanan, G. M. Di Gregorio, C. Ferrero and P. Mariani. *Phys. Rev. E*, Submitted, 2003.
- [3] M. Pisani, S. Bernstorff, C. Ferrero, P. Mariani. 2001. *Journal Phys. Chem. B*, 105: 3109-3119.

LAYER AND AGE SPECIFIC TENSILE TESTING OF HUMAN AORTAS: A SMALL ANGLE X-RAY SCATTERING STUDY

C.A.J. Schulze-Bauer¹, G. Sommer¹, M. Rappolt², H. Amenitsch², P. Laggner² and G.A. Holzapfel¹

- 1.) Institute for Structural Analysis, Computational Biomechanics, Graz University of Technology, Austria
<http://www.cis.tu-graz.ac.at/biomech/>
- 2.) Institute of Biophysics and X-ray Structure
Research, Austrian Academy of Sciences, Graz, Austria

For a thorough understanding of the mechanical behavior of soft biological tissues detailed information regarding the relation between collagen structures (nano-domain) and mechanical tissue responses (macro-domain) is required. Data are particularly rare for single layers (intima, media and adventitia) of human arteries. This study is aimed to investigate SAXS (Small Angle X-ray Scattering) diffraction patterns of isolated arterial layers during tensile testing in order to derive a mechanical model.

Human abdominal aortas were excised during autopsies of patients of different ages. Fresh and single-layered arterial stripes of the intima, media and adventitia were prepared. Specimens underwent uniaxial extension tests in a customized tensile testing machine. Test protocols (continuous, jump - relaxations) chosen allowed investigation of the characteristic nonlinear response of arterial tissues within the viscoelastic domain. Simultaneously, 2D diffraction pattern were recorded by means of a CCD camera. After tensile testing the specimens were analyzed histologically by means of light microscopy techniques.

Diffraction patterns obtained were highly specific for collagen fibrils. For unloaded specimens diffraction maxima were ring-shaped, while increasing tensile loads caused peak intensities at the 12 o'clock location indicating successive alignment of the collagen fibrils along the tensile axis. Highest intensities (up to the 11th order) were observed for the adventitia (see fig. 1), followed by the intima. Medial layers showed predominately diffuse scatter and only a weak first order maximum. For the adventitia and intima relations of the D-period and the distribution of the fibril orientation to the axial stresses in the tissue were determined (see figs. 2a-c). In particular, for the adventitia and the intima SAXS diffraction data in combination with tensile testing provide valuable data for micro- and nano-structural constitutive and age specific modeling.

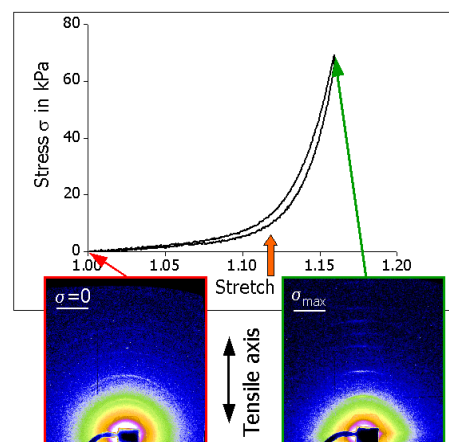
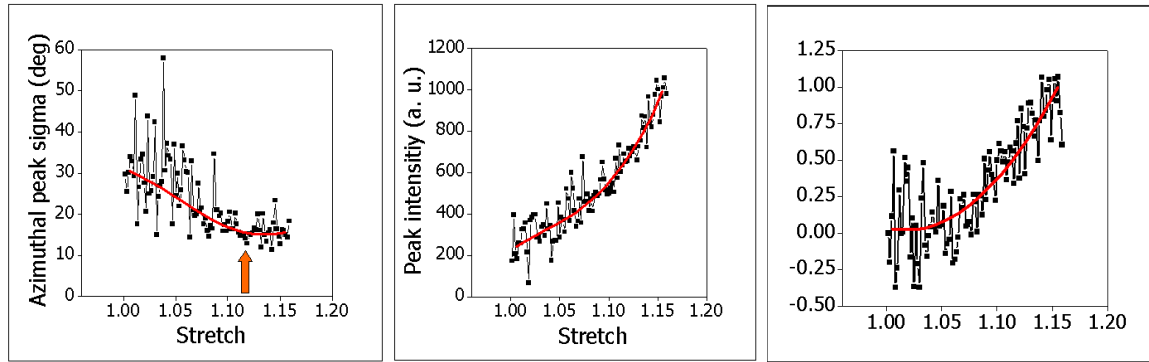


Figure 1. Stress-stretch diagram and 2D-diffraction pattern of the adventitia in the circumferential direction, clearly indicated by the induced ordering of the collagen due to the applied stress



a)

b)

c)

Figure 2. Azimutal peak sigma (a), peak intensity (b) and d-spacing (c) versus applied stretch.

Acknowledgement: Financial support for this research was partly provided by the “*Fonds zur Fortsetzung von Christian’s Forschung*”. This support is gratefully acknowledged.

PRESSURE-ASSISTED COLD DENATURATION OF METMYOGLOBIN BY SAXS

F. Spinozzi¹, P. Mariani¹, S. Cinelli², G. Onori², H. Amenitsch³, S. Bernstorff⁴, M. Kriechbaum³

- 1.) Istituto di Scienze Fisiche and INFM, Università Politecnica delle Marche, Via Ranieri 65, I-60131 Ancona (Italy)
- 2.) Dipartimento di Fisica and INFM, Università di Perugia, Via Pascoli, I-06123 Perugia (Italy)
- 3.) Institute of Biophysics and X-ray Structure Research, Austrian Academy of Sciences, Graz, Austria
- 4.) Sincrotrone Trieste S.C.p.A., Strada Statale 14, km 163.5, I-34016 Basovizza (Trieste), Italy

The native conformations of hundreds of proteins are known in great detail from structural determinations by X-ray crystallography and, more recently, NMR spectroscopy. However, detailed knowledge of the conformations of denatured and partially folded states is lacking, which is a serious shortcoming in current studies of protein stability and protein folding pathways. Therefore, increasing attention has been focused on denatured and partially folded states [1], and most studies dealing with protein denaturation have been carried out at atmospheric pressure with various physico-chemical perturbations, such as temperature, pH, or denaturants [2-4]. The thermal unfolding can often be represented by a two state equilibrium of the type $N \leftrightarrow D$, where N is the fully native and active protein and D an inactive, denatured state. The corresponding thermodynamic description of the phase boundary of protein unfolding has been recently reviewed by Smeller [5]. The Gibbs free energy difference, ΔG , between the two states N and D is written as

$$\Delta G(p,T) = \Delta\beta(p-p_0)/2 + \Delta\alpha(p-p_0)(T-T_0) - \Delta C_p [T(\log(T/T_0) + T_0)] + \Delta V_0(p-p_0) - \Delta S_0(T-T_0) + \Delta G_0 \quad (1)$$

where Δ represents the change of the corresponding parameter during the transition $N \leftrightarrow D$. β is the compressibility factor, α the thermal expansivity factor and C_p is the heat capacity. p_0, T_0 is a reference state (here 1 bar and 298 K). In the p/T plane, the phase diagram assumes a narrow near-elliptic contour, which include thermodynamic points where the protein is in the native state. At ambient pressure, this ellipse may have zero at two temperatures corresponding, respectively, to the temperature T_h for the heat denaturation and to T_c for the cold denaturation of the native protein. Moreover, the elliptic phase diagrams indicates that at room temperature (T_0) it may exist a denaturation pressure, p_d , which marks the separation between the N and the D regions. Therefore, by applying high pressure, one can investigate in detail not only pressure-denatured proteins, but also cold-denatured proteins in solution.

In this experiment, we have analyzed at the SAXS beamline of Elettra small-angle X-ray scattering of proteins in dilute solution under mechanical pressure. For this study metmyoglobin has been selected, because its pressure denaturation pathway has been yet studied by UV-Vis, FTIR and fluorescence spectroscopies [6] and because a number of studies have been performed in various denatured and partially folded states at ambient pressure. SAXS patterns were measured on metmyoglobin at pH 4.5 and at four different temperatures (10, 20, 30 and 45°C). Step of 100 bar in pressure, from 1 to 2000 bar were considered.

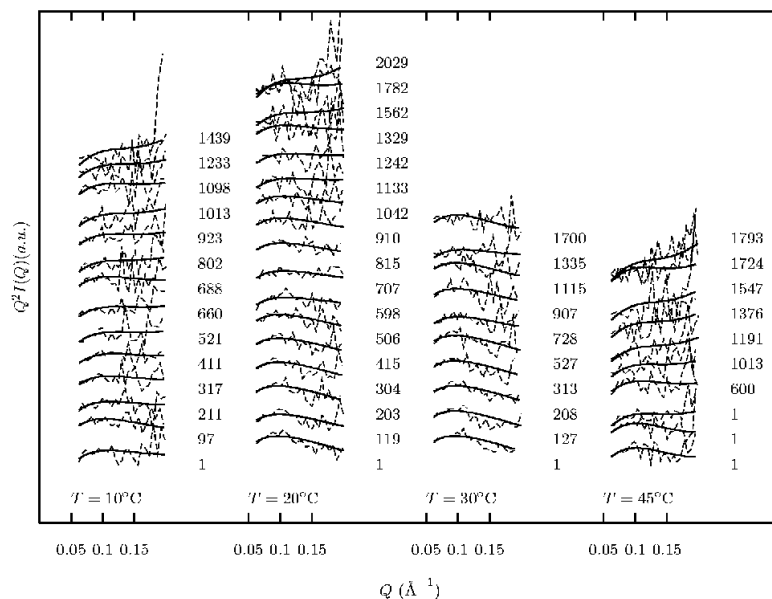


Figure 1. Kratky plots of metmyoglobin at different pressures (values indicated at the right of each curve) and temperatures. Fitting curves have been obtained with the global fitting analysis

Curves are shown in Figure 1 in the form of Kratky plots. To avoid radiation damage, the exposure time was 300 s/frame and a lead shutter was used to protect the sample from excess radiation within periods where no data were recorded. A preliminary Guinier and Debye analysis has been applied to the data. As a result, it has been observed that all the three D states (heat, cold and pressure denatured states) have similar scattering properties and have both radius of gyration and forward scattered intensity consistent with a dimeric structure. Hence, the presence of a unique denatured state is suggested. Afterwards, all the scattering curves have been simultaneously analyzed in the whole Q -range with the expression $I(Q;p,T)=\kappa\{\alpha_D(p,T)P^N(Q)+[1-\alpha_D(p,T)]P^D(Q)\}+B$, where $P^N(Q)$ is the form factor calculated from the crystallographic structure (PDB, entry code 4mbn) through the Monte Carlo method [7] and $P^D(Q)$ is the form factor of the Pedersen worm-like model [8]. $\alpha_D(p,T)$ is the denatured fraction, calculated as $\alpha_D(p,T)=\exp[-\Delta G(p,T)/RT]$, with ΔG from Eq. (1). κ and B represent a scaling factor and a flat background. The worm-like form factor is described by three parameters: R , the radius of gyration of the cross-section; L , the contour length and b , the statistical length. Two of them, b and R , are fitting parameters; the last one, L , is calculated by the constraint of a fixed dimer volume, i.e. $L=(V_D/\pi R^2)$. The other six fitting parameters are the thermodynamic constants $\Delta\beta$, $\Delta\alpha$, ΔC_p , ΔV_0 , ΔS_0 and ΔG_0 . Fitting curves are shown in Fig. 1, while the set of optimum parameters are reported in Table 1.

Table 1. Fitting parameters obtained by the global analysis of SAXS curves.

$\Delta\beta$ (cm ⁶ /cal mol)	$\Delta\alpha$ (cm ³ /°K mol)	ΔC_p (cal/°K mol)	ΔV_0 (cm ³ /mol)
-1.2	0.5	1100	-5.1
ΔS_0 (cal/°K mol)	ΔG_0 (cal/mol)	b (Å)	R (Å)
-90	550	16	13

In fig. 2 is reported the contour $\Delta G(p,T)=0$, corresponding to the midpoint of the N/D transition obtained by this analysis, together with the data reported by Zipp [6] at pH 4 and pH 5. The SAXS-derived curve, obtained at pH 4.5, is nearly in between. This study shows that the use of synchrotron SAXS under high pressure can be a powerful method for investigating the structural and thermodynamic properties of proteins.

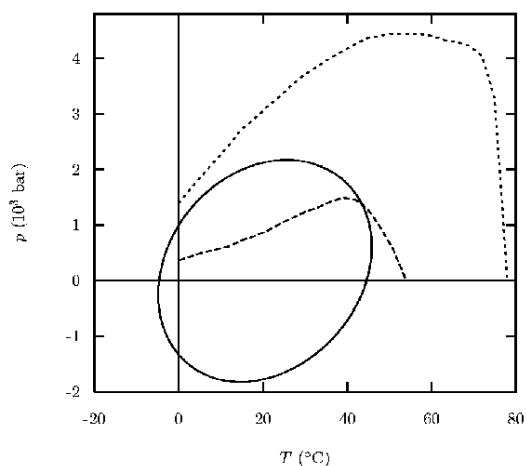


Figure 2. Phase diagram of metmyoglobin obtained by the global fitting of SAXS curves (solid line) at pH 4.5. Dotted (dashed) curve is the result obtained by UV-vis spectroscopy [6] at pH 4 (5).

References:

- [1] V. Calandrini, D.Fioretto, G.Onori and A.Santucci; Role of hydrophobic interactions on the stabilisation of native state of globular proteins; *Chem. Phys. Letters* **324**, 344-348 (2000).
- [2] A.Bonincontro, E.Bultrini, V.Calandrini, S.Cinelli and G.Onori; Effect of trehalose on alkaline transition of cytochrome-C; *J. Phys. Chem.* **104**, 6889-6893 (2000).
- [3] S. Cinelli, G. Onori and A. Santucci; Effect of 1-alcohols on micelle formation and protein folding; *Colloids and Surfaces A: Physicochemical and Engineering Aspects* **160**, 3-8 (1999).
- [4] M. Beltramini, P. Di Muro, R. Favilla, A. La Monaca, P. Mariani, A. L. Sabatucci, B. Salvato, P.L. Solari;. SAXS investigation on the temperature dependence of *Carcinus aestuarii* 5S hemocyanin subunit conformation; *J. Mol. Struct.* **475**, 73-82 (1999)
- [5] L. Smeller; Pressure-temperature phase diagrams of biomolecules; *Biochim. Biophys. Acta* **1595**, 11-29 (2002).
- [6] A. Zipp and W. Kauzmann; Pressure denaturation of metmyoglobin; *Biochemistry* **12**, 4217-4227 (1973).
- [7] S. Cinelli, F. Spinozzi, R. Itri, F. Carsughi, G. Onori and P. Mariani; Structural characterisation of the ph-denatured states of ferricytochrome-c by synchrotron small angle x-ray scattering; *Biophys. J.* **81**, 3522-3533 (2001)
- [8] J. S. Pedersen and P. Schurtenberger; Scattering functions of semi-flexible polymers with and without excluded volume effects; *Macromolecules* **29**, 7602-7612 (1996).

X-RAY SURFACE DIFFRACTION TO STUDY HIGHLY ALIGNED PHOSPHOLIPIDS UNDER INFLUENCE OF AMPHIFILIC MOLECULES AND SALT

C.V. Teixeira¹, H. Amenitsch¹, M. Rappolt¹ and P. Laggner¹

1.) Institute of Biophysics and X-ray Structure Research, Austrian Academy of Sciences, Schmiedlstr. 6, A-8010 Graz, Austria

Surface diffraction on oriented multilamellar membranes is a powerful technique, as it provides higher intensities and allows to derive refined structural information. In our studies we extended the work by Rappolt and colleagues [1,2], who investigated the influence of LiCl on liposomes. The effects of water/LiCl solutions on well aligned multilayers of POPC were followed by time-resolved surface diffraction at constant grazing angle using a transmission X-ray surface diffraction cell similar to [3]. The addition of LiCl solution causes an immediate broadening of the diffraction peaks, which can be separated into two contributions. The first one is related to osmotically stressed membrane stacks and whereas the second is related to unstressed lipid domains. Contrarily to the before mentioned work, the transition into the final equilibrium phase was much shorter than in liposomes (15 min compared to days) and the splitting was not so strongly pronounced.

The different dynamical behavior of the phases is discussed as a consequence of various defects depending on the sample preparation, which either facilitates the Li diffusion through the membranes or establishes osmotic stress. The addition of amphiphilic molecules at low concentrations to the lipids, like 0.1 mol% oleyl alcohol (OA), was supposed to heal the membrane defects. The experiments confirmed this effect of healing by the introducing of osmotic stress after exposing the lipid coatings to LiCl solutions as seen by the diffraction pattern in fig. 1.

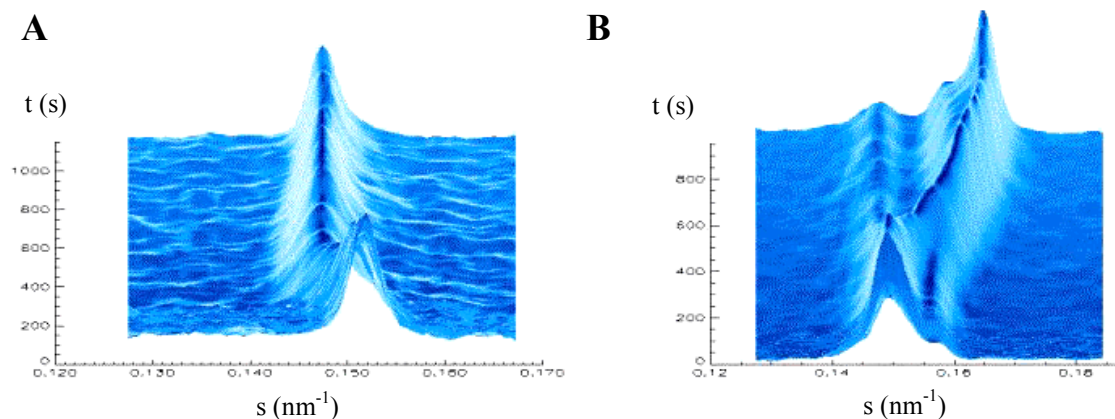


Figure 1. Stack plot of surface X-ray diffraction pattern of POPC during addition of a 0.3 M LiCl solution. (A) Lipid sample prepared with 0.01 mol% oleyl alcohol and (B) with 0.1 mol% oleyl alcohol. In the later many defects are healed out and osmotic stress is built up.

References:

- [1] Rappolt, M., G. Pabst, H. Amenitsch, and P. Laggner. 2001. Salt-induced phase separation in the liquid crystalline phase of phosphatidylcholines. *Colloid and Surfaces A* 183, 171-181.
- [2] Rappolt, M., K. Pressl, G. Pabst, and P. Laggner. 1998. L_{α} -phase separation in phosphatidylcholine-water systems induced by alkali chlorides. *Biochim. Biophys. Acta* 1372, 389-393.
- [3] Vogel, M., C. Munster, W. Fenzl, and T. Salditt. 2000. Thermal unbinding of highly oriented phospho-lipid membranes. *Phys. Rev. Lett.* 84, 390-393.

3. Physics

COCRYSTALLIZATION DYNAMICS IN LAMELLAR SYSTEMS OF PEO/PEO AND PEO/PEO-*b*-PPO-*b*-PEO BLENDS

J. Baldrian¹, M. Steinhart¹, A. Sikora¹, G. Todorova², M. Kriechbaum³, H. Amenitsch³ and S. Bernstorff⁴

- 1.) Institute of Macromolecular Chemistry, Academy of Sciences of the Czech Republic, Heyrovsky Sq.2, 162 06 Prague, Czech Republic
- 2.) Faculty of Physics, University of Sofia, J.Bourchier 5, 1126 Sofia, Bulgaria
- 3.) Institute of Biophysics and X-ray Structure Research, Austrian Academy of Sciences, Schmiedelstr. 6, A-8010 Graz, Austria
- 4.) Sincrotrone Trieste, Basovizza, 34012 Trieste, Italy

This study was aimed at a better understanding of the dynamics of lamellar structures development in two different binary blends PEO/PEO and PEO/PEO-*b*-PPO-*b*-PEO, and thus to contribute to a deeper knowledge of the cocrystallization behaviour of these systems.

Binary mixtures of low-molecular-weight fractions ($M_w \sim 2000, 3000, 4000$ and 6000 - P2, P3, P4, P6; Fluka AG) of poly(ethylene oxide) (PEO) and these polymers with a tri-block copolymer PEO-*b*-PPO-*b*-PEO ($M_w \sim 3340-1760-3340$, Pluronic 6800 - P68, BASF) of 8/2, 6/4, 4/6 and 2/8 compositions were prepared. The copolymer was chosen because it has M_w of PEO tails near to the M_w of neat PEO fractions used. The middle poly(propylene oxide) (PPO) block is amorphous. The blends were studied by the time-resolved SAXS method on the synchrotron and by DSC. Measurements were performed during isothermal melt-crystallization at 35, 40, 45 °C and in the course of cooling of the melt and subsequent heating (60 °C \rightarrow 30 °C \rightarrow 60 °C).

Blends of PEO fractions were studied during isothermal crystallization and during cooling and heating. A single cocrystal system or this system with a small amount of another lamellar systems are formed in the blends during both treatments. The thickness of the cocrystal lamellae increases with increasing concentration of higher molecular-weight PEO in blends (Fig.1). This thickening is caused by a growing number of higher-molecular-weight chains incorporated in cocrystal lamellae. Blends P2/P4 and P2/P6 have the tendency to form during thermal treatment lamellae with thicknesses close to the size of the extended chains of P2. This is associated with the experimental fact that P2 chains are not able to fold and chains of P4 and P6 are able to fold once (1F) and twice (2F) respectively and form stable cocrystalline lamellae with P2.

Binary mixtures of PEO fractions with block copolymer PEO-*b*-PPO-*b*-PEO were studied. Blends of the block-copolymer with PEO fraction P2 form during both thermal treatments a single cocrystalline system consisting of lamellae with thickness around 16 nm. In the neat copolymer and in blends with P3 and P4 where dominated copolymer, two different lamellar systems LP1 (with thicker lamellae) and LP2 are simultaneously formed during isothermal crystallization. In blends with a majority of neat PEO, a single lamellar system is developed. The cocrystal systems are formed in all types of blends during crystallization (Fig.2). The LP1 lamellae in blends with P3 consist of extended chains of P3 and of extended PEO tails of copolymer. The LP1 cocrystal structures developed in blends with P4 are formed by NIF (nonintegrally folded) chains of P4 and NIF and EC of PEO tails of the copolymer. In both kinds of blends, the LP2 lamellar systems are cocrystals consisting of 1F and NIF chains of both components. During heating, near the melting points of components, all blend structures recrystallize in the bulk volume into a new, single cocrystalline structure.

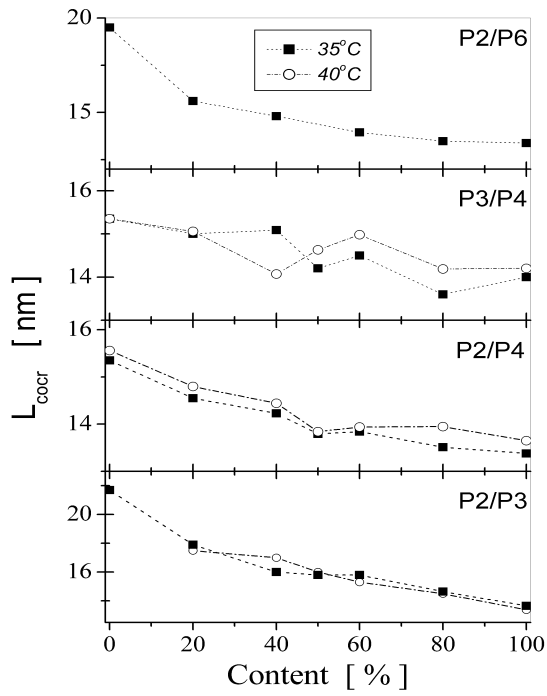


Figure 1. Dependence of thickness of cocrystalline lamellae in PEO/PEO blends on the composition

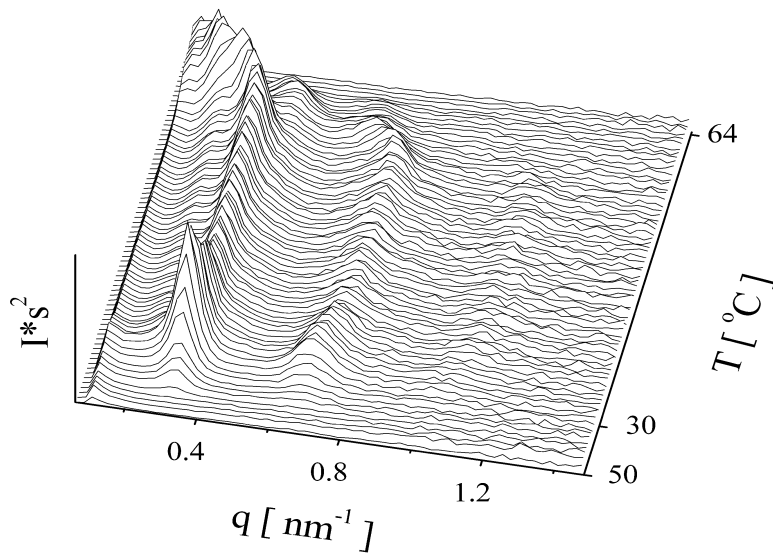


Figure 2. Lorentz-corrected SAXS curves development of P68/P4 2/8 blend during cooling and heating

Research was supported by the Grant Agency of the Czech Republic (grant No. 203/03/0611) and the Grant Agency of the Academy of Sciences of the Czech Republic (grant No. A4050007).

PHASE BEHAVIOUR OF ALPHA-ZIRCONIUM PHOSPHATE INTERCALATED BY HIGHER ALCOHOLS

M. Steinhart¹, L. Benes², K. Melánová², V. Zima², M. Kriechbaum³, H. Amenitsch³ and S. Bernstorff⁴

1.) University Pardubice, Studentská 84, Pardubice, Czech Republic

2.) Joint Laboratory of Solid State Chemistry of Institute of Macromolecular Chemistry of Academy of Sciences and University Pardubice, Studentská 84, Pardubice, Czech Republic

3.) Institute of Biophysics and X-ray Structure Research, Schmiedlstrasse 6, Graz, Austria

4.) Sincrotrone Elettra, Trieste, Basovizza, 34012 Trieste, Italy

Intercalation represents a reversible insertion of mobile atomic or molecular guest species into a solid layer host lattice [1, 2]. By intercalation, a variety of new materials with interesting properties can be prepared. This fact is the obvious reason for the fast development in this region. Intercalates of zirconium phosphate (α -Zr(HPO₄)₂·H₂O, hereafter ZrP) [3] belong among largely studied compounds.

In our previous measurements on the ZrP – liquid alcohol systems research [4], we have observed phase transitions induced by temperature changes. Since the phases involved differ in basal spacing and thereby in crystal thickness, pressure dependence had been expected.

Our recent study has been targeted to better understanding of phase properties of several ZrP – higher alcohol systems in temperature range from 20 – 70 °C and pressure range 1 – 1600 bar including time dependence of phase changes.

ZrP systems intercalated by 1-octanol, 1-nonanol, 1-decanol were prepared. The particular guests were chosen since from our previous measurements we could have estimated the phase boundaries and some model ideas about the expected changes. The high-pressure system capable of time-resolved measurements [5] with an improved temperature control system was used.

The dependence of basal spacing on pressure measured at various temperatures for 1-octanol and 1-nonanol intercalated ZrP is given in the Figures 1. and 2. The intercalates studied show different behaviour. For the 1-nonanol intercalate, there is a gradual linear decrease of basal spacing with increasing pressure at constant temperature up to a certain value of pressure when a second phase appears. The basal spacing of this second phase also decreases with increasing pressure. Both phases coexist in the area of phase transition. The relative amounts of these phases change with time as is shown in Figure 3. For 1-octanol intercalated ZrP, the basal spacing-pressure dependence is more complicated. There is a small increase of basal spacing just before the phase transition. Also the basal spacing of high-pressure phase gradually shifts in a wide range of pressures.

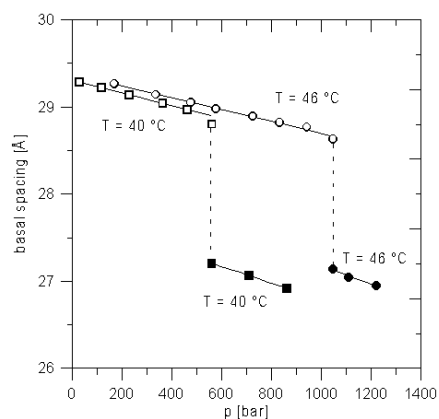


Figure 1. Phase diagram of Zr(HPO₄)₂·2C₉H₁₉OH.

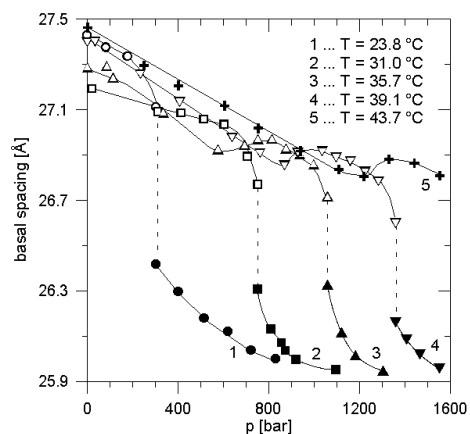


Figure 2. Phase diagram of $\text{Zr}(\text{HPO}_4)_2 \cdot 2\text{C}_8\text{H}_{17}\text{OH}$.

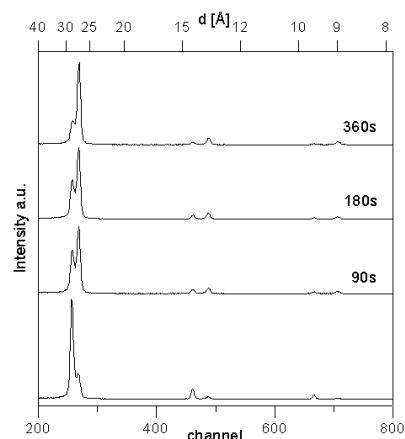


Figure 3. Time development of phase change of $\text{Zr}(\text{HPO}_4)_2 \cdot 2\text{C}_9\text{H}_{19}\text{OH}$ at $46\text{ }^\circ\text{C}$ and 1048 bar.

References:

- [1] A. J. Jacobson in *Encyclopaedia of Inorganic Chemistry*, Ed. R. B. King, Vol. 3, Wiley, Chichester 1994, p. 1556.
- [2] "Intercalation Chemistry", Ed. M. S. Whittingham and A. J. Jacobson, Academic Press, New York, 1982.
- [3] G. Alberti, U. Costantino in *Comprehensive Supramolecular Chemistry*, Ed. J. M. Lehn, Pergamon/Elsevier, Elmsford, 1996, Vol. 7, p. 1.
- [4] U. Costantino, R. Vivani, V. Zima, L. Beneš, K. Melánova; "Microwave-assisted intercalation of 1-alkanols and 1, ω -alkanediols into α -zirconium phosphate. Evidence of conformation phase transformation in the bimolecular film of alkyl chains."; *Langmuir* **18**, 1211-1217 (2002)
- [5] M. Steinhart, M. Kriechbaum, K. Pressl, H. Amenitsch, P. Laggner and S. Bernstorff; "High-pressure instrument for small- and wide-angle x-ray scattering II. Time-resolved experiments"; *Rev.Sci.Instrum.* **70/2**, 1540-1545 (1999)

4. Chemistry

FIRST DIRECT OBSERVATION OF SELECTIVE COUNTERION CONDENSATION IN IONIC MICELLES

V.K. Aswal¹, P.S. Goyal², H. Amenitsch³ and S. Bernstorff⁴

- 1.) Spallation Neutron Source Division, Paul Scherrer Institute, CH-5232 PSI Villigen, Switzerland.
- 2.) IUC-DAEF, Mumbai Centre, Bhabha Atomic Research Centre, Mumbai 400 085, India.
- 3.) Institute of Biophysics & X-Ray Structure Research, Austrian Academy of Sciences, Graz, Austria.
- 4.) Sincrotrone ELETTRA, Trieste, Italy

Surfactant molecules consist of two distinct segments that are opposite in character. One part is polar in character and is known as head group, while the other part is comprised of one or more long hydrophobic tails. These molecules self-aggregate in aqueous solution above critical micelle concentration (CMC) to form micelles [1]. Surfactant molecules such as cetyltrimethylammonium bromide (CTABr) ionize in aqueous solution and the corresponding micelles are aggregates of CTA^+ ions. The micelle is charged and is called an ionic micelle. The Br^- ions, known as counterions, tend to stay near the CTA^+ micellar surface. The shape, size, fractional charge of the micelle and the intermicellar interaction depend on the distribution and the nature of these counterions.

It is known that the effect of addition of salts KBr and KCl to the ionic micellar solutions of cationic surfactant (e.g. CTABr or CTACl) is quite different [2]. In terms of counterion condensation, this suggests the differences in the condensation of Br^- and Cl^- ions that takes place on the charged micelles. We compare the structure in the equimolar surfactant to salt micellar solutions of CTABr/KCl and CTACl/KBr systems and explain the results in terms of selective counterion condensation. In particular, we show that CTACl/KBr micellar solution behaves like CTABr/KCl due to selectivity of counterion condensation.

A combined study of SANS and SAXS has been used to study the counterion condensation. While neutron scattering in micellar solutions is from the core of the micelle, x-rays are largely scattered by counterions especially when the counterion has a large atomic number (e.g. Br^-). The neutron scattering intensity from the counterions is negligible in comparison to that from the core. Thus neutrons see the core of the micelle and x-rays in combination with neutron studies give the information relating to the counterion condensation around the micelle [3]. Figure 1 shows the SANS data from equimolar surfactant to salt CTABr/KCl and CTACl/KBr micellar solutions. These systems have common in them the same number of surfactant CTA^+ ions and as well as Br^- and Cl^- counterions. For comparison, the data from 100 mM CTABr and CTACl micellar solutions without salt are also shown in Figure 1.

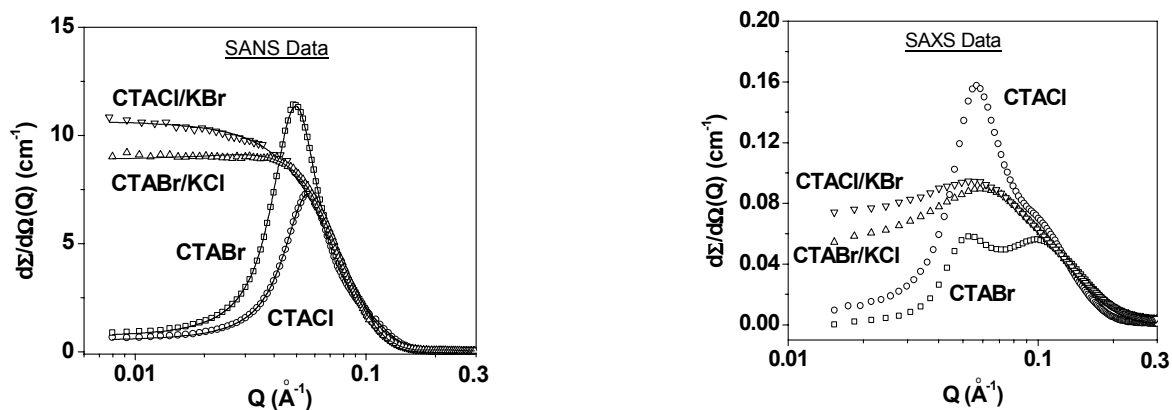


Figure 1. SANS and SAXS data from 100 mM equimolar surfactant to salt micellar solutions of CTABr/KCl and CTACl/KBr. The data from 100 mM CTABr and CTACl micellar solutions without salt are also shown.

It is observed that the counterion condensation is more effective in CTACl/KBr than CTABr/KCl. We believe this is due to selective condensation of the counterions around the micelles [4]. In CTABr/KCl, Br^- counterions from the dissociated CTABr molecules are condensed on the CTA^+ charged micelles. The condensation of Cl^- ions of the salt KCl takes place around the condensed Br^- ions. However, in CTACl/KBr, Cl^- counterions of the CTACl molecules are replaced by Br^- ions of the KBr in the micelle. This is expected since Cl^- ions are less effective than Br^- to neutralize the charge on the micelles. The condensation of Br^- ions around the condensed Cl^- counterions does not seem possible in CTACl/KBr as this contrary to the experimental results would make the counterion condensation less effective in CTACl/KBr than CTABr/KCl to neutralize the charge on the micelles. The above SANS results are directly confirmed by the SAXS experiments (Figure 2), where the scattering data depending on the condensed counterions is expected to be different. Figure 2 shows that while the SAXS data of CTABr and CTACl are very different, the data for CTABr/KCl and CTACl/KBr are quite similar. The small differences in the SANS or SAXS data of CTABr/KCl and CTACl/KBr can be explained in terms of a small fraction of condensed Cl^- counterions in CTACl/KBr, which are not replaced by the Br^- counterions. This provides slightly higher condensation of Cl^- counterions on the micelles of CTACl/KBr than CTABr/KCl, otherwise these two systems have similar counterion condensation of Br^- and Cl^- ions around them. Figure 2 shows the SANS and SAXS data on equimolar surfactant to salt micellar solutions of anionic surfactants of sodium dodecyl sulfate (NaDS) and lithium dodecyl sulfate (LiDS) in presence of LiBr and NaBr, respectively. For comparison, the micellar solutions from pure NaDS and LiDS are also shown in Figure 2. It is found that while the SANS data on pure NaDS and LiDS are significantly different, the equimolar surfactant to salt solutions of NaDS/LiBr and LiDS/NaBr are similar. These results are similar to those on cationic surfactants and support the selective counterion condensation in ionic micellar solutions. It is confirmed from the SAXS data that in LiDS/NaBr micellar solution, Li^+ counterions are replaced by Na^+ counterions, so that this systems has the similar counterion condensation to that of NaDS/LiBr. The Na^+ ions are preferred on the micellar surface due to their less hydrophilicity as compared to Li^+ ions.

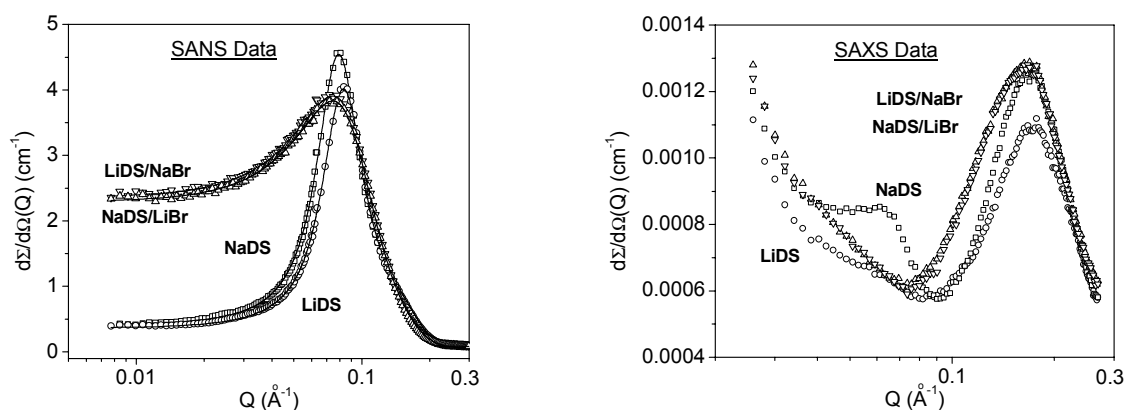


Figure 2. SANS and SAXS data from 200 mM equimolar surfactant to salt micellar solutions of NaDS/LiBr and LiDS/NaBr. The data from 200 mM NaDS and LiDS micellar solutions without salt are also shown.

References:

- [1] Y. Chevalier and T. Zemb, Rep. Prog. Phys. **53**, 279 (1990).
- [2] V.K. Aswal and P.S. Goyal, Phys. Rev. E **61**, 2947 (2000).
- [3] V.K. Aswal et al. Chem. Phys. Lett. **329**, 336 (2000).
- [4] V.K. Aswal and P.S. Goyal, Phys. Rev. E (in press).

SELF-ASSEMBLING OF MESOSTRUCTURED SILICA FILMS CONTAINING FULLERENE DERIVATIVES

P. Falcaro¹, P. Innocenzi², M. Maggini³, D. Grosso⁴ and H. Amenitsch⁵

- 1.) Dipartimento di Ingegneria Meccanica, Università degli Studi di Padova, via Marzolo 9, 35100 Padova, Italy.
- 2.) Dipartimento di Architettura e Pianificazione, Laboratorio di Scienza dei Materiali e Nanotecnologie, Università degli Studi di Sassari, Palazzo Pou Salid, Piazza Duomo, 07041 Alghero, Italy.
- 3.) Dipartimento di Chimica Organica, Università degli Studi di Padova, via Marzolo 1, 35100 Padova, Italy.
- 4.) Chimie de la Matière Condensée, UPMC – CNRS, 4 place Jussieu, 75005 Paris, France.
- 5.) Institute of Biophysics and X-ray Structure Research, Austrian Academy of Science, Schmiedlstraße 6, 8042 Graz, Austria.

Mesostructured ordered silica films can be synthesised via self-assembling processing using many different kinds of surfactants as templating agents [1]. An interesting property of these films is the possibility to functionalize the surface after that the surfactant removal. These materials, especially in the form of films, are an ideal host for organic functional molecules that can be introduced via impregnation, reaction with surface silanols or added in the precursor sol in a “on-pot” synthesis.

Generally the precursor sol is obtained adding a silica alkoxyde such as tetraethoxysilane, a solvent (ethanol), a reactant to hydrolyze the silicon precursor (water), an acid catalyst (HCl) and a surfactant as templating agent. In our case we adopted the Brij-58 and Pluronic F-127: two non-ionic blocks copolymer surfactant. This choice was related to the advantages that they show with respect to ionic surfactants [2].

We have used a “one-pot” route to introduce fullerenes in silica mesostructured films. Because of the low solubility of fullerenes in polar solvents we have modified the composition of the sol substituting part of the ethanol with tetrahydrofuran (THF). Fullerenes show in fact an increased solubility in THF. We have also designed the fullerene derivatives to tune the shape and polarity of the molecule in order to fit the synthesis in presence of block-copolymers. Two different types of fullerene derivatives were selected: N-[(3-triethoxysilyl)propyl]-2-carbomethoxy-fulleropyrrolidine **1** (TPCF) prepared *via* the 1,3-dipolar cycloaddition of azomethine ylides to C₆₀ and N-(3,6-dioxa-9-hydroxynonyl)-fulleropyrrolidine **2** (DHNF) synthesised in 24% isolated yield, *via* azomethine ylide cycloaddition, by treating N-(3,6-dioxa-9-hydroxynonyl)glycine, *para*formaldehyde and C₆₀ in refluxing toluene (Fig.1 a and b). Both TPCF and DHNF can covalently link to the growing porous matrix through the triethoxysilyl and hydroxy group respectively. In principle, this would sustain a structuring action of the fulleropyrrolidine during the self-assembly of the matrix. In DHNF the oxyethylene chain is a further structural element that could favor its participation to the assembly process.

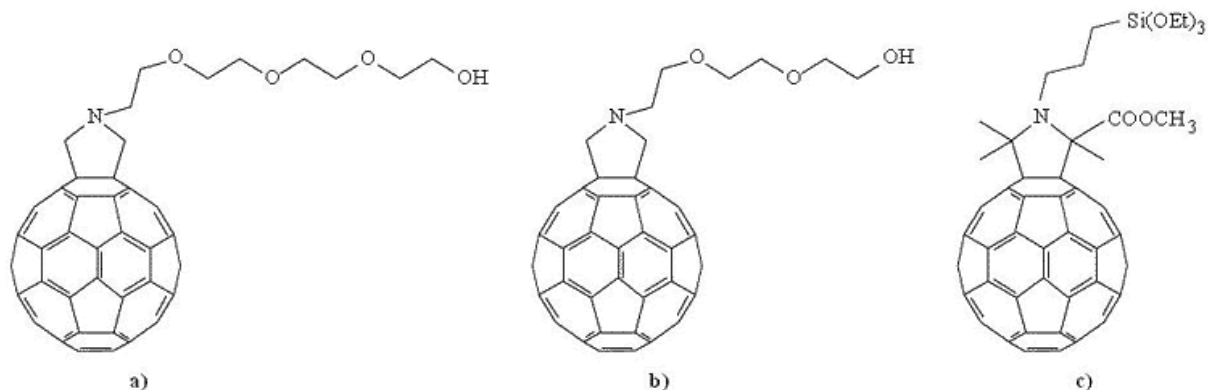


Figure 1. Fullerene derivatives used in the one pot synthesis.

The possibility to verify the feasibility of introducing optically active molecules in the mesostructures films in one pot synthesis conserving a good order degree, was a main goal of our work. The study was realized observing the proceeds of the self assembling after dipping (in-situ time-resolved) and the differences in the kinetic process between the solution (containing THF) with and without fullerene derivatives. The SAXS apparatus was used in transmission or grazing angle and it was evaluated For DHNF doped films, diffraction spots typical of 2D-hexagonal structures were observed after ca. 20 s from deposition, whose intensity increased with the drying time. The time-resolved, *in situ* analysis gave also additional information on the kinetics of the EISA process. The reorganisation of the initially disordered phase into a 2D-hexagonal one required around 1000 s. Then the normal contraction of the film which can last for several minutes, was the only phenomenon that could be observed, as revealed by the change in intensity of the diffraction spots. Different conditions of relative humidity in the deposition room permitted to obtain different 2d hexagonal cells with different parameter lattice for the two surfactants employed: in every case the fullerene derivatives affected did not affect the self assembling process (Fig.2 a - b and c - d).

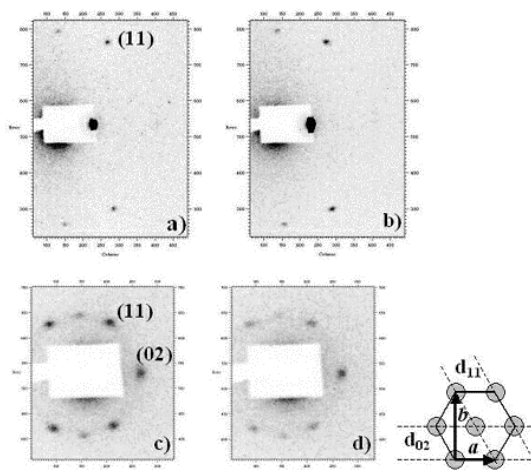


Figure 2. Comparison of two diffraction patterns between films obtained by Brij-58 solution with (b) and without (a) DHNF and Pluronic F-127 with (c) and without (d) DHNF. No significant differences can be observed.

The fullerenes with the $\text{Si}(\text{OH})_3$ functionalities introduced a decrease of the mesophasic order. The distinct behaviour of TPCF and DHNF is likely related to their different structure. In principle, both TPCF and DHNF can bind to the growing inorganic network creating silica blocks tethered to fullerene spheres. The bulky and hydrophobic fullerenes, enclosed in the micelle core during EISA, acts as a center of attraction for the silica units that are pushed to form the hybrid organic inorganic-interface at the micelle surface.

References:

- [1] Galo J. de. A. A. Soler-Illia, Clément Sanchez, Bénédicte Lebeau, Joël Patarin, Chemical Strategies To Design Textured Materials: from Microporous and Mesoporous Oxide to Nanonetworks and Hierarchical Structures, *Chem. Rev.* **102**, 2002, 102, 4093-4138 (2002)
- [2] Galo J. de. A. A. Soler-Illia, Eduardo L. Crepaldi, David Grosso, Clément Sanchez,; Block Copolymer-Templated Mesoporous Oxides; *Curr. Op. Colloid Inter. Sci* (2003), in press

IN-SITU X-RAY DIFFRACTION STUDY OF THE FORMATION OF MESOPOROUS ORGANOSILICATES UNDER ACIDIC CONDITIONS.

V. Goletto¹, R. Blum¹, F. Babonneau¹, M. Tiemann², M. Linden² and H. Amenitsch³

1.) Chimie de la Matière Condensée, UPMC/CNRS, 4 place Jussieu, 75005 Paris

2.) Department of Physical Chemistry, Abo Akademi University, Porthansgatan 3-5, FIN-20500 Turku, Finland

3.) Institute of Biophysics and X-ray Structure Research, Austrian Academy of Sciences, Schmiedelstraße, 8042 Graz, Austria.

Surfactant-templated silicates have played a prominent role in materials chemistry during the last decade. One important way of modifying their physical and chemical properties has been the introduction of organic functions covalently bonded to the framework to form new, functionalizable materials that may have specialized applications in the field of catalysis, sensing, electronics or optics. One synthetic method consists in the direct introduction of the organic functions during the synthesis, via cocondensation of organotrialkoxysilanes ($\text{RSi}(\text{OR}')_3$) and tetraalkoxysilanes ($\text{Si}(\text{OR}')_4$), in presence of a structuring agent. A variety of organic functionalities have already been successfully introduced in nanoporous silicate powders, either as passive or reactive surface groups [1].

Most of the preparations have been so far performed under basic conditions, and result in the formation of 2d-hexagonal phases, with a strong electrostatic interaction (S^+I^-) between the cationic surfactant (S^+) and the highly negatively charged silica surface (I^-). It is also possible to use strong acidic conditions, for which the interaction mode between the surfactant and the inorganic framework can be described as ($\text{S}^+\text{X}^-\text{I}^0$), where X^- is an anion. Such experimental conditions affect the overall self-assembly mechanism, and can stabilize mesophases with higher interface curvature, especially micellar cubic phases. It provides routes to structures with three-dimensional channel connectivities that are attractive for certain applications. Another interesting aspect in the formation of these organosilicate-surfactant mesophases, that has not been yet addressed in the literature, is the role played by the organic functions covalently bonded to the framework in the self-assembly mechanism. This was recently illustrated in our laboratory with phenyl-modified silicates, using CTAB as template. Under acidic conditions, a cubic $Pm\bar{3}n$ phase is obtained while a 2d-hexagonal $p6m$ phase is formed for pure silica [2], suggesting that the phenyl groups are developing specific interactions with the polar head groups of CTAB, increasing the effective size of these entities, and favouring a high interfacial curvature.

This report deals with time resolved X-ray scattering investigation of one-pot synthesis in strong acidic conditions, of a cubic $Pm\bar{3}n$ surfactant-silica mesophase functionalized with phenyl groups.

Experimental. The measurements were performed at the SAXS beamline of the 2GeV electron storage ring ELETTRA, Trieste, Italy. The radiation wavelength was 1.542 Å. The data were collected on a linear position-sensitive Gabriel detector. The batch reactor consists of a beaker containing the synthesis mixture, a peristaltic pump, tubing, and a quartz capillary (diameter : 1 or 2 mm). The synthesis mixture flowing through the capillary is recycled by pumping (25 mL/min) it back to the batch reactor. The time-resolved measurement, with a time resolution of 1-to-30 s per frame, was started ($t=0$) by initiating the mixing of the two-phase solution (CTAB in acidic aqueous solution and mixture of silanes) and switching on the pump. After each measurement, the tubing was cleaned with a 1M NaOH solution for about 10 minutes, then with distilled water for another 10 minutes.

Results. The first study was performed on a silicate/CTAB system prepared from tetraethoxysilane (TEOS) in strong acidic conditions. Figure 1 illustrates the formation of the hexagonally ordered material as a function of time. The organisation appears 3 minutes after the mixing of reactants although the solution already shows the formation of a solid. One can observe a low angle Bragg reflection as well as two other reflections at wider angles of weak intensity; that could be indexed as the (10), (11) and (20) reflections of a 2D-hexagonal structure ($a=4.19$ nm). The (10) peak increases in intensity and shifts to a wider angle with time, indicating a progressive contraction of the cell parameter to $a=4.12$ nm (-2%) after 10 min. One can notice the sharpness of the main peak, which may be related to the presence in solution, after this short reaction time, of poorly condensed oligosiloxanes, which behave like a liquid crystal solution.

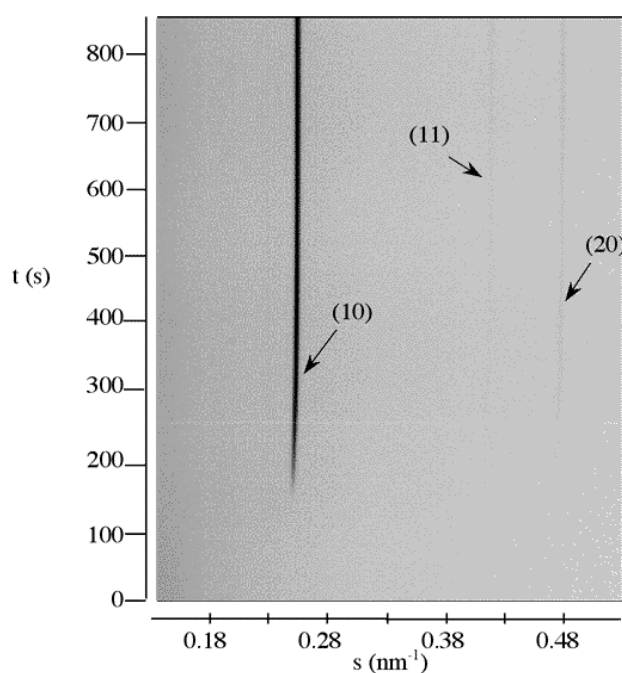


Figure 1. Time-resolved X-ray scattering pattern for the silica-surfactant system (TEOS/CTAB/H₂O/HCl = 1.0:0.12:130:9.2 in molar ratios)

The same study was then performed on the phenyl-functionalized silica system prepared from phenyltriethoxysilane (PTES) and TEOS in a 1:4 molar ratio. In this case, the only first 6 minutes could be recorded, the blocking of the capillary at that time preventing any further measurement, even when using a 2 mm capillary. Figure 2 presents the X-ray scattering patterns obtained for this system. In this case, the induction period (around 1 minute) is shorter than for the pure TEOS/CTAB system: a single reflection peak appears, corresponding to a correlation distance of 3.89 nm. This peak shifts in position, indicating a continuous and large contraction of the system (-6 %). Four minutes after the beginning of the experiment, two new peaks appear at smaller angles. The three peaks could then be indexed as the (200), (210) and (211) of the final Pm3n cubic structure, leading to a cell parameter of 8.94 nm. Their position shifts to larger values, showing again a contraction of the structure down to a cell parameter of 8.73 nm. Interestingly, the position of the first peak perfectly matches the position of the (210)_{cub} peak, which suggests an epitaxial relation between the intermediate phase and the final cubic one. This is in agreement with a study reported in the literature on the formation of SBA-1-type silica with a Pm3n structure [3].

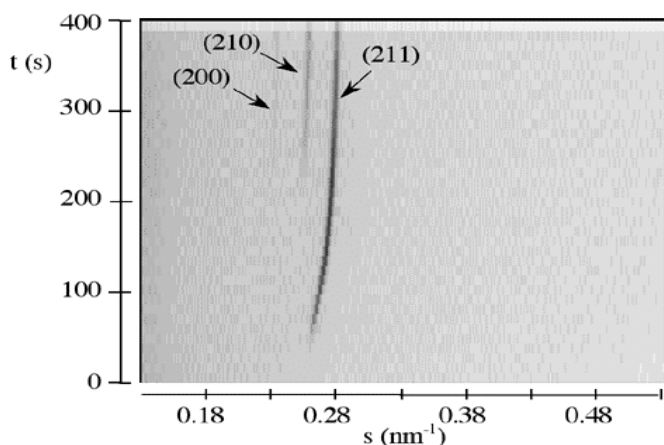


Figure 2. Time-resolved X-ray scattering pattern for the phenyl-functionalized silica-surfactant system (PhTES/TEOS/CTAB/H₂O/HCl = 0.2:0.8:0.12:130:9.2 in molar ratios)

The formation of the cubic Pm3n phase when phenyl groups are covalently bonded to the silica framework, suggests a specific interaction between these phenyl groups and the CTAB polar head groups. In parallel to the previous study, we have thus studied the formation of mesoscopically ordered silica/surfactant composites under acidic synthesis conditions with benzene used as an additive ($0 \leq \text{benzene/CTAB} \leq 8.33$). We found that benzene acts as a weak swelling agent although most of the benzene molecules are found to reside near the surfactant/silicate interface region rather than in the micelle cores. With increasing relative amounts of benzene the curvature of the micellar aggregates decreases, which finally leads to a transition from (hexagonally) rod-like to lamellar (Figure 3). A mechanism for this change in curvature is represented in Figure 4.

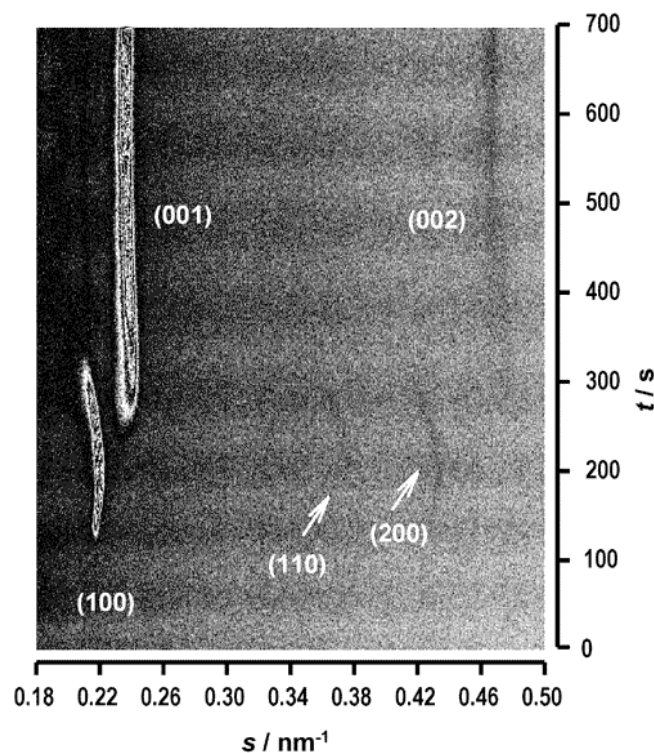


Figure 3. Temporal evolution of the SAXS pattern for a synthesis of meso-structured silica/surfactant composites with benzene as an additive (benzene/CTAB = 6.58 molar ratio).

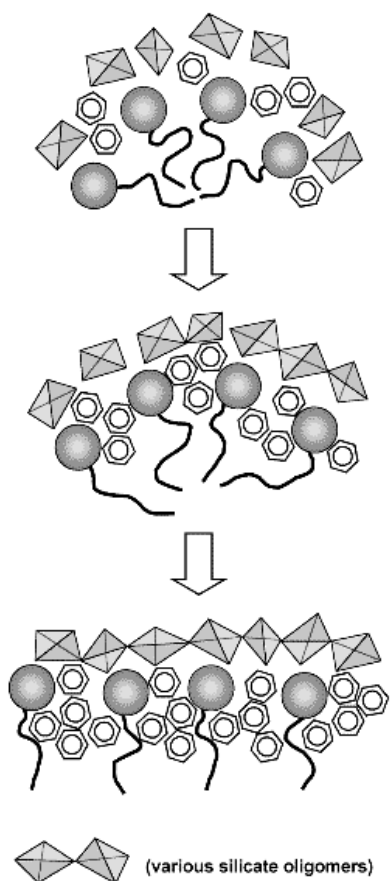


Figure 4. Schematic drawing of the change in the curvature of the silica/surfactant aggregates in presence of benzene as an additive.

References:

- [1] A. Stein, B.J. Melde and R.C. Schroden, *Adv. Mater.*, **12** 1403 (2000).
- [2] V. Goletto, M. Imperor and F. Babonneau in *Studies in Surface Science and Catalysis 129* – A. Sayari et al. (Eds) – Elsevier (2000) p. 287-294
- [3] S. Che, S. Kamiya, O. Terasaki, T. Tatsumi, *J. Am. Chem. Soc.*, **123**, 12089 (2001).

INFLUENCE OF THE CPG CONFINEMENT ON THE NEMATIC-SMECTIC A LIQUID CRYSTAL PHASE TRANSITION

A. Zidanšek¹

1.) J. Stefan Institute, Jamova 39, Ljubljana, Slovenia

Influence of the pore surface treatment on the nematic (N) to smectic A (SmA) phase transition of the 8CB (octylcyanobiphenyl) liquid crystal confined to controlled pore glass (CPG) matrices has been studied. The void surface was either nontreated or covered with silane enforcing planar or homeotropic anchoring, respectively. The phase and the structure of confined liquid crystal in this system reflect the interplay between elastic and surface interactions.

We studied the smectic order parameter and the smectic correlation length as a function of temperature and characteristic diameter of CPG voids between 300 nm and 24 nm using the small angle X-ray scattering (SAXS) method [1]. The SAXS patterns showing a first order diffraction peak at the inverse distance between the smectic layers in the SmA phase were measured between 20 and 50° C. In silane-treated samples with void diameter between 130 nm and 300 nm the N-SmA phase transition is shifted to a higher temperature. In non-treated samples with the void diameter above 130 nm there is a much smaller temperature shift in the N-SmA transition. This indicates that the surface ordering effect is stronger for the silane-treated samples. In smaller pores the Smectic A phase is much less pronounced and appears at a lower temperature than in the bulk. Results have been analysed in terms of a Landau-Ginsburg type description.

References:

[1] A. Zidanšek, S. Kralj, R. Repnik, G. Lahajnar, M. Rappolt, H. Amenitsch, and S. Bernstorff, *J. Phys.: Condensed Matter*, 2000, vol. 12, pp A431 - A436.

5. Instrumentation

DETECTOR DEVELOPMENT AT THE SAXS BEAM LINE ⁺

Ralf -Hendrik Menk¹, Heinz Amenitsch², Sigrid. Bernstorff¹, Hans Juergen Besch⁴, Francesco Voltolina³

1.) Sincrotrone Trieste, S.S.14, km 163.5, Basovizza, 34012 Trieste, Italy

2.) Institute of Biophysics and X-Ray Structure Research, Graz, Austria

3.) Univ. degli Studi di Trieste, Trieste, Italy

4.) Fachbereich Physik, Universität-GH Siegen, 57068 Siegen, Germany

Recently there are new detector developments on the way in aiming to overcome rate and dynamic problems in SAXS measurements. Although gaseous detectors are often considered as “classical” or “old fashioned” devices, in combination with novel gas amplification structures and sophisticated electronics they reveal unique features that make them a superior detection device and thus well suited for installation at modern beam lines.

Clearly, the use of single photon counters carries several advantages since they do not contribute additional noise and hence their dynamic range is almost unlimited at least as long no dead time losses are introduced. However, these devices are in general rate limited. On the other side integrating detectors have a higher rate capability but since they comprise always an inherent noise level they are not so suitable for low flux applications. In the following a novel detector device will be presented that comprises the advantages of both detector types. Basically it is an integrating device based on the principle of a highly segmented gaseous ionization chamber, which can be operated in gas amplification mode. In this fashion the gas gain mechanism is used to adjust the total charge in the detector according to the incoming photon flux, so that for each single photon a signal is always generated which is significantly higher than the noise background of the integrating electronics. Hence, for almost all photon fluxes single photon precision can be obtained.

Principle of charge generation and mechanic set-up

The one dimensional (Fig.1) detector [1] -is a highly segmented ionization chamber featuring an active area of 192 cm x 10 mm. The configuration as described here is suitable for the detection of x-rays in the energy range between (5-25 keV). As depicted in (Fig.2), photons entering the detector through the entrance window (thin carbon fiber) and the drift cathode (aluminized Mylar foil) are absorbed mainly by photoelectric absorption in the detector gas (such as Ar / CH₄, Ar / CO₂ or Xe/CO₂ under pressure up to 3 bars). During this process $n = E_{\gamma}/W_{ion}$ primary charges are generated, when E_{γ} is the energy of the photon and W_{ion} is the mean energy required to create an ion / electron pair in the detector gas. For the distance of 20 mm between drift cathode and MicroCAT and a photon energy below 12 keV the quantum efficiency (QE) can be calculated as 100% for a Xe/CO₂ gas mixture at 3 bar pressure. In the constant drift field of 20 mm length the ions are transported to the drift cathode, while the electrons are transported to the gas amplification structure (MicroCAT) [2]. The MicroCAT is a 55 μ m thick perforated nickel foil with micro-holes (116 μ m diameter) in a hexagonal arrangement. The center to center pitch of the holes is 164 μ m. At a distance of about 200 μ m below the MicroCAT, which is supplied with negative high voltage (typically 100-1000 V), the virtual grounded anode is placed. Due to this configuration the electric field increases strongly in the

⁺ Project is supported by the European Community Contract No. FMBICT 980104

vicinity of the micro-holes reaching an almost constant plateau between the MicroCAT and the anode (typically 5-80 kV/cm). Most of the field lines starting from the drift cathode aim through the micro holes onto the anode. In this fashion almost all electrons produced in the primary charge are feed through the micro holes of the MicroCAT and are transferred on the anode with an electron transparency of about 100% (in contrast to the optical transparency of the MicroCAT which lies in the order of 50%). Thus the MicroCAT structure can be utilized as an excellent shielding grid, which enables frame rates as high as 10kHz. If the field is high enough secondary electrons are produced, which subsequently builds avalanches in the vicinity of the anode (gas gain) [3]. Depending on the applied fields this avalanche comprises up to 10^5 electrons per primary electron. However, in order to maintain a constant gas gain along the direction of the position encoding, the distance between MicroCAT and anode has to be kept in the order of some 10 μm . For the active area given here the use of frame-like spacer outside the active region is sufficient as long as the anode features sufficient planarity. The position encoding in one direction (192 cm) stems from the subdivision of the anode into 1280-readout strips having a pitch of 150 μm between two adjacent strips in the active area. This anode (Fig.3) is realized using ultra thin multilayer processes on a Kapton foil*, which was subsequently glued on a very precise aluminum board of 10 mm thickness. Typically the resistance between two adjacent strips is $10^{13} \Omega$.

As mentioned before the precision in terms of planarity (better than 20 μm on 192 cm) of the board and thus of the read out anode is crucial for spatially homogeneous gas gain operations. The anode is partially accommodated in an aluminum housing comprising the conversion gas mixtures mentioned before. It is sealed with the anode using Torr SealTM, which is an excellent sealant in vacuum equipment requiring vacuum down to 10^{-9} or lower. It forms a high strength bond with metals, ceramics or glass. Since no solvent are involved to evaporate this kind of glue ensures the purity of the gas as required for gas gain operations.

The electrons released either in the primary charge generation (ionization chamber mode) or after the gas amplification (gas gain mode) are collected on the anode strips and integrated for a certain time (time frame) in attached amplifier channels.

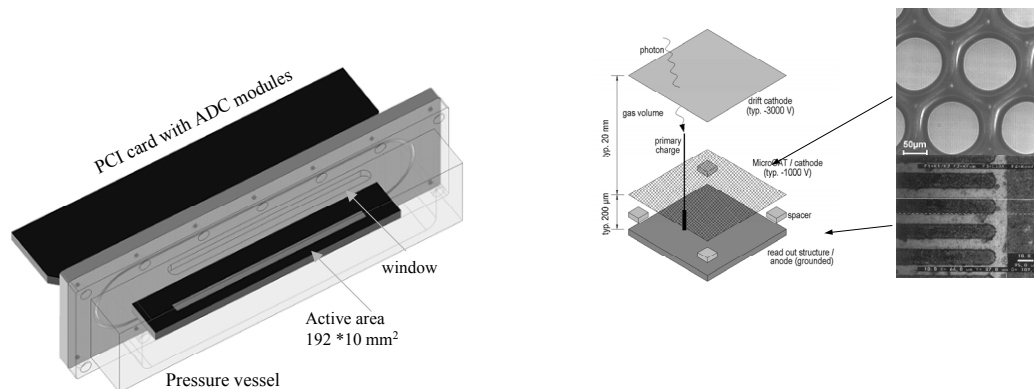


Figure 1. Schematic view of the detector housing showing the read out anode bonded to the pressure vessel.

Figure 2. Exposed view of the detector plus details of the gas gain structure (MicroCAT) and the position-encoding anode. The full active area of 192 x 10 mm² is composed of 1280 anode strips with a pitch of 150 μm .

* ILFA Address, Lohweg 3, 30559 Hannover, Germany

Analog Electronics

Outside the pressure vessel the anode strips are fan-out and subsequently are connected via micro connectors to 10 VLSI carrier boards. Each carrier board comprises two custom made mixed analog digital chips that are successors of the JAMEX VLSI [4]. This new monolithic read out system (Fig. 4) comprises 64 low noise analog integrators with reset switch followed by 64 sample and hold stages including a eight times correlated sampling stage as well as a 64:1 multiplexer and a differential output buffer. Sixteen different feedback capacities and subsequently 16 different gains can be programmed for eight blocks of eight channels. Those capacities range from 0.4pF to 47.4pF. Suitable integration times lay between 0.1 – 200 ms and can be selected by the user. However, the leakage current of the JFET gate, which builds the first amplifier stage, is of the order of some pA. For an integration time of 0.1 ms the equivalent charge accumulated is thus 25 electrons. This gives an acceptable signal to leakage current ratio considering that for instance a single 8 keV photon releases around 300 electrons (with no gain in the MicroCAT). Since the noise of the leakage current for that integration time is in the order of 5 electrons equivalent a unique discrimination for a single photon is ensured for an integration time of 0.1 ms and thus a frame rate of 10 kHz. While integrating the charges in the feed back capacity it is possible to read the contents of the sample and hold stages. However, due to the reset times of the feedback capacities a detector dead time or 8% at the maximum frame rate of 10 kHz is observed. This means a reduction in the detective quantum efficiency (DQE)[5] of 8%, which is for most applications acceptable.

Digital Electronics

The acquisition electronics is built around a commercially available multi channel ADC system developed by SUNDANCE[#] (Fig.5 and Fig.6).

However, the Sundance system does not match the requirements of the Jamex Chips in the first place. Thus both systems have to be interfaced via a so-called Jamex to the Sundance (J2S) interface card that is a big mixed-signal board 337x130 mm in dimension using 6 layers gold plated technology. As mentioned before the JAMEX features a differential current output stage to match the high requirements on the noise performances and rejection.

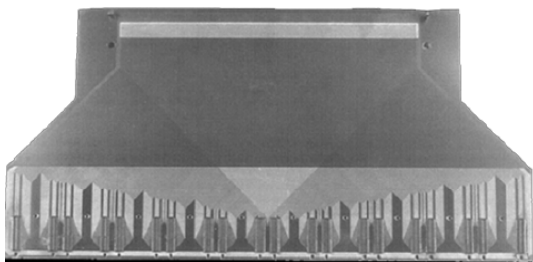


Figure 3. Photograph of the readout anode.

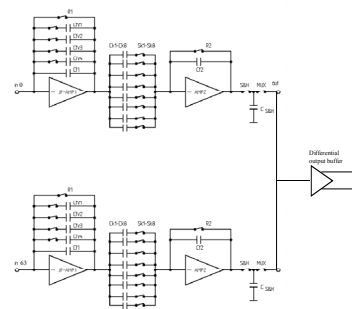


Figure 4. Sketch of 64 channel JAMEX monolithic read out system

[#] www.sundance.com

Therefore the J2S board performs differential to single ended conversion, individually programmable offset shifting in order to use full resolution of each A/D converter. Moreover, an analog 1st order low pass filtering is provided in order to reduce the overall system noise of the chain. A PGA (programmable gain amplifier) provides better flexibility for high dynamic range imaging and a built in limiting function helps to avoid A/D overflow recovery problems. Another important function of the J2S board is to provide linear power supply, reference rails and the correct LVDS digital signals to control the operation and time frames of the 20 Jamex chips, allowing functionality like individual gain setting for each channel group, and different operation modes. The cabling between the Jamex hybrids (using flexifoil links) and the Sundance ADCs cards take place through several connectors on this separate board. Test signal generation capability is also embedded on the J2S board in order to give the possibility to test all the detector electronics without the need to use an x-ray source.

On the SUNDANCE side a single PCI bus board carries (Fig.7) up to 4 standard TIM modules. In the present configuration 3 Sundance ADC modules (Fig.8) are used providing 8 ADCs @10 Mhz, 14 bit each, for a total of 24 analog inputs on 1 board. In this way it is possible to connect the outputs of the Jamex chips directly to 20 of the analog ADCs inputs available. The four spare inputs are used to monitor other signals and are used for debugging purposes. There are 2 additional modules on a second PCI carrier board containing one 320C64x DSP chip as well as one Virtex FPGA module. Next to other tasks the DSP is in charge for offset corrections and channel gain normalization. The DSP as well as the FPGA card are programmed using special communication ports on the PCI carrier board.

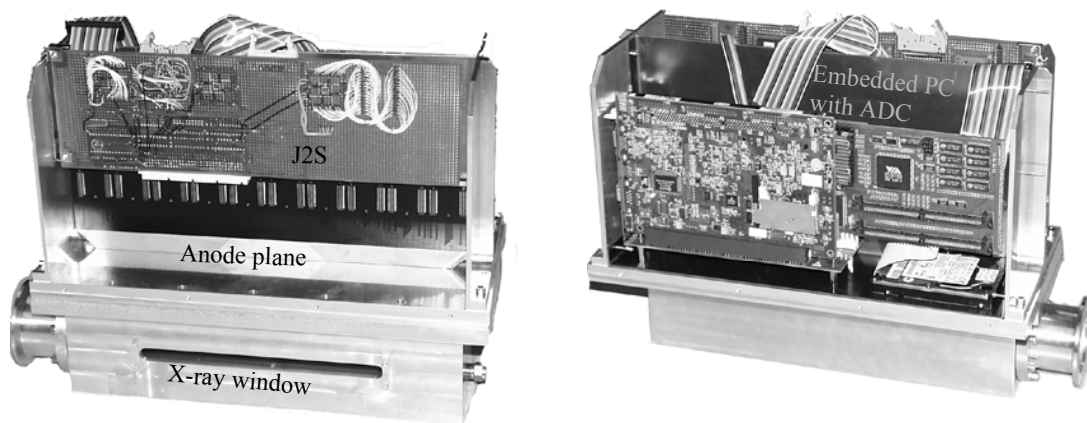


Figure 5. Photograph of the front side of **Figure 6.** Backside of the detectors with the detector. Visible are x-ray entrance embedded PC and carrier support for the window, partially the anode structure as multi channel ADC cards. well as the J2S.

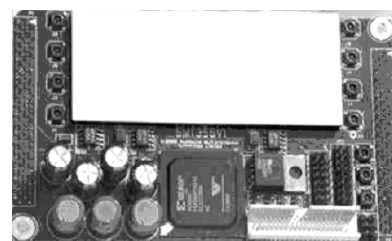
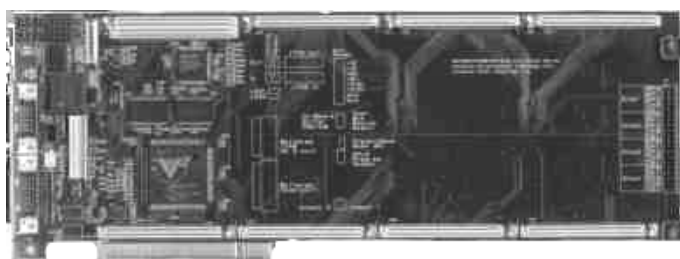


Figure 7. Photograph of the Sundance PCI carrier board. **Figure 8.** Photograph of the Sundance ADC board.

Both PCI carrier boards are stacked inside the detector together with a small half-size PCI card embedded computer and a custom bus back-plane. All digital equipment is placed inside the detector in a specific shielding box in order to avoid electro-magnetic pick-up by the Jamex chips or the buffering electronics on the J2S card.

The configuration described here allows a very short cabling between the Jamex output signal and the ADC inputs and thus improves in signal to noise and distortion in comparison with a long cable analog signal transmission solution.

All the communication between the external outside world and the embedded PC takes place via a standard Ethernet interface. This allows easy software maintenance and firmware reconfiguration for the whole system.

Conclusion and outlook

The unique feature of the Micro-CAT structure allows combining the advantages of a single photon counter with the characteristics of an integrating detector. If single photon resolution is required the gas gain can be adjusted in such a fashion that the charge released by the single photon is substantially higher than the equivalent noise charge of the integrating electronics. Moreover, the choice of the conversion gas and the gas pressure provides a high flexibility for applications in different energy ranges. A high intensity precision is combined with a good spatial resolution, a high local rate capability and time resolution of 100 μ s.

The entire system with 1280 channels will be tested in May 2003 on the SAXS beam line.

References:

- [1] R. H. Menk, F. Arfelli, S. Bernstorff, D. Pontoni, A. Sarvestani, H.J. Besch, A.H. Walenta (1998). Nucl. Instr. and Meth. A 422, 698-703
- [2] A. Sarvestani, H. J. Besch, M. Junk, W. Meißner, N. Sauer, R. Stiehler, A. H. Walenta, R. H. Menk, "Study and Application of Hole Structures as Gas Gain Devices for Two Dimensional High Rate X-ray Detectors", Nucl. Instr. and Meth. A 410, pp. 238-258, 1998.
- [3] R.H. Menk, A. Sarvestani, H.J. Besch, A.H. Walenta, H. Amenitsch, S. Bernstorff, "Gas gain operations with single photon resolution using an integrating ionization chamber in small-angle X-ray scattering experiments" Nucl. Instr. and Meth. A 440 (1): 181-190 JAN 21 2000
- [4] W. Buttler, G. Cesura, P.F. Manfredi, V. Re, V. Speziali, G. Burbach, H. Vogt: A bulk JFET and CMOS/SIMOX technology for low noise, high speed charge-sensitive amplifier, IEEE International SOI Conference, 5.-7. October 1993, Palm Springs, California
- [5] R.H. Menk, W. Thomlinson, N. Gmur, Z. Zhong, D. Chapman, F. Arfelli, W.R. Dix, W. Graeff, M. Lohmann, G. Illing, L. Schildwachter, B. Reime, W. Kupper, C. Hamm, J. Giacomini, H.J. Gordon, E. Rubenstein, J. Dervan, H.J. Besch, A.H. Walenta The concept of spatial frequency depending DQE and its application to a comparison of two detectors used in transvenous coronary angiography, Nucl. Instr. and Meth. A 398 (2-3): 351-367 OCT 21 1997

Publications

Publications in 2002

M.A. Bagni, G. Cecchi, B. Colombini, S. Bernstorff, H. Amenitsch, C.C. Ashley and P.J. Griffiths

Changes in force and myosin heads orientation induced by temperature increase in frog muscle fibres.

Biophysical Journal 82, 1795 (2002)

J. Baldrian, M. Horky, M. Steinhart, P. Laggner, P. Vlèek, H. Amenitsch and S. Bernstorff

Time-resolved SAXS/WAXS study of phase behaviour and crystallization in polymer blends

Journal of Macromolecular Science-Physics B41, pp. 1023-1032 (2002)

A.D. Bokare, D.Das, H.Amenitsch, and A.Patnaik

Orientalional ordering in polymorphic terephthal-bis-4- butylaniline (TBBA)

Solid State Communications 122, 329-333 (2002)

J.Bonarski, M.Zehetbauer, Z.Swiatek, E.Schafler and S.Bernstorff

Structural Investigation of Silicon Platelets for Solar Cells By Advanced Methods of X- Ray Diffraction

Proc. Review Seminar "Physics and Materials Science", Polish Academy of Sciences, (May 27-30, 2001, Vienna, Austria), p. 171-177 (2002)

W. Bras, H. Amenitsch, and S.U.Egelhaaf

Time-resolved small angle scattering in soft condensed matter and biological systems

Synchrotron Radiation News 15, 27-31 (2002)

M. J. M. Darkes, T. A. Harroun, S. M. A. Davies & J. P. Bradshaw

The effect of fusion inhibitors on the phase behaviour of N-methylated dioleoylphosphatidylethanolamine

Biochim. Biophys. Acta 1561, 119-128 (2002)

P. Dubcek, S. Bernstorff, U.V. Desnica, I.D. Desnica-Frankovic, K. Salamon

GISAXS Study of Cadmium Sulfide Quantum Dots

Surface Review and Letters, Vol. 9, No. 1 (2002) 455-459

P. Dubcek, N. Radic, O. Milat and S. Bernstorff

Grazing Incidence Small Angle X-Ray Scattering Investigation of Tungsten-Carbon Films Produced by Reactive Magnetron Sputtering

Surface and Coatings Technology 151-152, pp. 218-221 (2002)

R. Gianni, F. Delben, G. Liut, S. Bernstorff, H. Amenitsch and R. Rizzo

Synthesis and conformational properties of cyanoethylscleroglucan

Carbohydrate Polymers 47 (2002) 387-391

P.J. Griffiths, M.A. Bagni, B. Colombini, H. Amenitsch, S. Bernstorff, C.C. Ashley and G. Cecchi

Changes in myosin S1 orientation and force induced by a temperature increase
Proc. Nat. Acad. Sci. USA, 99/8, 5384-5389 (2002)

P.J. Griffiths, M.A. Bagni, B. Colombini, H. Amenitsch, S. Bernstorff, C.C. Ashley, and G. Cecchi.

Time-resolved X-ray studies of head domain orientation in the molecular motor, myosin, during force generation
J. Physiol., 543: 15-16s (2002)

H. Grigoriev, A. Wolińska-Grabczyk, S. Bernstorff

Solvent Influenced Mesostructures in Polyurethane-based Membranes of Different Transport Parameters using SAXS
Journal of Materials Science Letters 21 (2) 113-116 (2002)

H. Grigoriev, A. Wolińska-Grabczyk, M.Plusa, S. Bernstorff

Kinetics of the Structural Changes in Polyurethanes Saturated with Benzene During Desorption Process
J Mater Sci. Lett. 21-15, pp. 1179-1182 (2002)

H. Grigoriev, A. Wolińska-Grabczyk, S. Bernstorff, A. Jankowski

Temperature effected structural transitions in polyurethanes saturated with solvents studied by SAXS synchrotron method
J Macromol. Sci. – Pure Appl. Chem. A39(7), pp. 629-642 (2002)

D. Grosso, F. Babonneau, P.A. Albouy, H. Amenitsch, A.R. Balkenende, A. Brunet-Bruneau, J. Rivory

An in-situ study of mesostructured CTAB-silica film formation during dip-coating, using time-resolved SAXS and interferometry measurements
Chem. Mater. 14-2, pp. 931-940 (2002)

D. Grosso, F. Babonneau, G.J.D..A. Soler-Illia, P.A. Albouy, H. Amenitsch

Phase transformation during cubic mesostructured silica film formation
Chemical communications 7, pp. 748-749 (2002)

M. Hammel, M. Kriechbaum, A. Gries, G. M. Kostner, P. Laggner, and R. Prassl

Solution structure of human and bovine b2-Glycoprotein I revealed by small angle x-ray scattering.
J. Molecular Biology, 321/1, 85-97 (2002)

T. A. Harroun, M. J. M. Darkes, S. M. A. Davies & J. P. Bradshaw

The effect of fusion inhibitors on the phase behaviour of DOPE-Me, and their role in Fusion
Biophysical Journal 82, 542A (2002)

D. Kalnin, G. Garnaud, H. Amenitsch, M. Ollivon

Monitoring fat crystallization in aerated food emulsions by combined DSC and time resolved synchrotron X-ray diffraction
Food Res. Int., 35 (2002) 927-934

- N. P. Kumar, S. Major, Satish Vitta, S.S. Talwar, P. Dubcek, H. Amenitsch, S. Bernstorff, V. Ganesan, A. Gupta and B.A. Dasannacharya
Molecular packing in cadmium and zinc arachidate LB multilayers
 Colloids and Surfaces A: Physicochemical and Engineering Aspects 198-200 (2002) 75-81
- N. Prasanth Kumar, S.N. Narang, S. Major, Satish Vitta, S.S. Talwar, P. Dubcek, H. Amenitsch and S. Bernstorff
Structure of CdS-arachidic acid composite LB multilayers
 Colloids and Surfaces A: Physicochemical and Engineering Aspects 198-200 (2002) 59-66
- V. La Carrubba, V. Brucato and S. Piccarolo
Phenomenological approach to compare the crystallisation kinetics of Isotactic Polypropylene and Polyamide-6 under pressure
 Journal of Polymer Science – Part B – Polymer Physics, Volume 40, Number 1, Issue January 1, (2002) 153-175
- V. La Carrubba, V. Brucato and S. Piccarolo
Influence of „controlled processing conditions“ on the solidification of iPP, PET and PA6
 Macromolecular Symposia, Volume 180, Issue 1 (2002) 43-60
- P. Laggner, H. Amenitsch and M. Kriechbaum
Single-Molecule / High-Throughput / Real-Time: The Challenges for X-Ray Structure Research"
 Proceedings of SAMBA 2 (Symposium on Applications of Particle Detectors in Medicine, Biology and Astrophysics, 27-29 May 2002, Miramare, Trieste, Italy)
- M.L. Lavcevic, A. Turkovic
The measurements of particle/crystallite size in nanostructured TiO₂ films by SAXS/WAXD method
 Scripta Materialia 46, pp. 501-505 (2002)
- A. Lind, J. Andersson, S. Karlsson, P. Ågren, P. Bussian, H. Amenitsch, M. Lindén
Controlled solubilization of toluene by silicate-cationic surfactant mesophases as studied by in situ and ex situ XRD
 Langmuir 18 (2002) 1380-1385
- F. Lo Celso, A. Triolo, F. Triolo, D.I. Donato, M. Steinhart, M. Kriechbaum, H. Amenitsch, R. Triolo
SAXS investigation on aggregation phenomena in supercritical CO₂
 European Physical Journal E, 8/3 (2002) 311-314
- O. López, M. Cócera, R. Pons, H. Amenitsch, J. Caelles, J.L. Parra, L. Coderch and A. de la Maza
Use of Synchrotron Radiation SAXS to Study the first Steps of the Interaction between Sodium Dodecyl Sulphate and Charged Liposomes
 Spectroscopy 16, 343 -350, 2002

- Menk, R.H., H. Amenitsch, F. Arfelli, F. Montanari, and D. Dreossi
Preliminary results of A combined USAXS and diffraction enhanced imaging system with synchrotron radiation
 Proceedings of 2002 IEEE International Symposium on Biomedical Imaging Washington DC, July 7-10 2002, CD-ROM:565-567
- A. Orthen, H. Wagner, H.J. Besch, R.H. Menk and A.H. Walenta
Charge transfer considerations of MicroCAT-based detector systems
 Nucl. Instr. and Methods A 492 (2002) 160-177
- G. Pabst, J. Katsaras, V.A. Raghunathan, and M. Rappolt
Pretransitional swelling of Phospholipid bilayers above the main transition
 National Research Council of Canada, Annual Report 2002, pp. 52-53
- O. Paris, H. Gupta, W. Tesch, P. Roschger, P. Fratzl
Scanning -SAXS: A Tool for Structural Characterization of Complex Materials at the Micrometer and the Nanometer Scale
 Acta Cryst. A58 (supplement) (2002) C25
- L. Pidol, D. Grosso, G.J.A..A. Soler-Illia, E. Crepaldi, C. Sanchez, P.A. Albouy, H. Amenitsch and P. Euzen
Hexagonally organised mesoporous aluminium-oxo-hydroxide thin films prepared by the template approach. In-situ study of the structural formation
 Journal of Material Chemistry 12, pp. 557-564 (2002)
- D. Posedel, A. Turkovic, P. Dubcek and Z. Crnjak-Orel
Grazing-incidence X-ray reflectivity on nanosized vanadium oxide and V/Ce oxide films
 Materials Science & Engineering B90, 154-162 (2002)
- R. Puxkandl, I. Zizak, O. Paris, J. Keckes, W. Tesch, S. Bernstorff, P. Purslow and P. Fratzl
Viscoelastic properties of collagen - synchrotron radiation investigations and structural model
 Phil. Trans. Roy. Soc. London B 357, 191-197 (2002)
- M. Rappolt, A. Hickel, F. Bringezu and K. Lohner
Structural study in the lamellar/inverse hexagonal phase region of phosphatidyl-ethanolamines.
 Chem. Phys. Lipids, 118 (2002) 55
- F. Spinozzi, D. Gazzillo, A. Giacometti, P. Mariani, F. Carsughi
Interaction of proteins in solution from small angle scattering: a perturbative approach
 Biophys. Journal 82, 2165-2175 (2002)
- M. Tiemann, V. Goletto, R. Blum, F. Babonneau, H. Amenitsch, M. Lindén
In-situ SAXS Studies on the Formation of Silicate-Surfactant Mesophases with Solubilized Benzene under Acidic Conditions
 Langmuir, 18 (2002) 10053-10057

- A. Triolo, F. Lo Celso, C. Di Giovanni, H. Amenitsch and R. Triolo
Morphology of solid polymer electrolytes: a TR-WAXS investigation
Physica A 304, pp. 129-134 (2002)
- A. Triolo, F. Lo Celso, F. Triolo, H. Amenitsch, M. Steinhart, P. Thiyagarajan, S. Wells, J. M. De Simone and R. Triolo
Kinetics of block copolymers aggregation in super critical CO₂
Journal of Non-Crystalline Solids 307, pp. 725-730 (2002)
- F. Triolo, A. Triolo, F. Lo Celso, D.I. Donato and R. Triolo
Dilute and Semi dilute Solutions of Block Copolymers in water, Near-critical and Super-critical CO₂: a Small Angle Scattering Study of the Monomer-Aggregate Transition.
Physica A, 304, 135–144 (2002)
- R. Triolo, F. Lo Celso, A. Triolo, F. Triolo, D.I. Donato, M. Steinhart, M. Kriechbaum, H. Amenitsch
SAXS investigation on aggregation phenomena in supercritical CO₂
Eur. Phys. J. E-Soft Matter 8, 311-314 (2002)
- R. Triolo, A. Triolo, F. Lo Celso, F. Triolo, H. Amenitsch, M. Steinhart, P. Thiyagarajan, S. Wells and J. M. DeSimone
Kinetics of block copolymers aggregation in supercritical CO₂
J. Non- Crystal. Sol., 307-310, 725-730 (2002)
- R. Triolo, A. Triolo, F. Locelso, C. Di Giovanni and H. Amenitsch
Structural and dynamical characterization of melt PEO-salt mixtures
Physica A 304, 308-313 (2002)
- R. Triolo, A. Triolo, F. Lo Celso, C. Di Giovanni and H. Amenitsch
Morphology of Solid Polymer Electrolytes : a TR WAXS Investigation
Physica A 304, 129-134 (2002)
- V. Vidya, N. Prasanth Kumar, S. Major, Satish Vitta, S.S. Talwar, P. Dubcek, H. Amenitsch and S. Bernstorff
Molecular packing in CdS containing conducting polymer composite LB multilayers
Colloids and Surfaces A: Physiochemical and Engineering Aspects 198-200 (2002) 67-74
- H. Wagner, H.J. Besch, R.H. Menk, A. Orthen, A. Sarvestani, A.H. Walenta and H. Walliser
On the dynamic two-dimensional charge diffusion of the interpolating readout structure employed in the MicroCAT detector
Nucl. Instr. and Methods A 482 (2002) 334-346
- H. Wagner, A. Orthen, H.J. Besch, R.H. Menk, A.H. Walenta and U. Werthenbach
On the improvement of a flexibly applicable gaseous 2D MicroCAT detector for highly time-resolved X-ray imaging
Proceedings of SAMBA 2 (Symposium on Applications of Particle Detectors in Medicine, Biology and Astrophysics, 27-29 May 2002, Miramare, Trieste, Italy)

M. Zehetbauer, E. Schafler, T. Ungar, I. Kopacz and S. Bernstorff
Investigation of the Microstructural Evolution During Large Strain Cold Working of Metals by Means of Synchrotron Radiation - A Comparative Overview
J. Eng. Mater.-Technol. Transaction ASME, 124-, pp. 41-7 (2002)

Publications in January to July 2003

B. Alonso, A.R. Balkenende, P.A. Albouy, H. Amenitsch, M.N. Rager and F. Banonneau
Hybrid 3D ordered mesoporous thin films made from organosiloxane precursors
Journal of Sol-Gel Science and Technology 26, pp. 587-591 (2003)

F. Cagnol, D. Grosso, G.J.D.A. Soler-Illia, E.L. Crepaldi, F. Banonneau, H. Amenitsch and C. Sanchez
Humidity-controlled mesostructuration in CTAB-templated silica thin film processing. The existence of a modulable steady state.
Journal of Materials Chemistry 13, pp. 61-66 (2003)

J. De Roche, C.M. Gordon, C.T. Imrie, M.D. Ingram, A.R. Kennedy, F. Lo Celso, A. Triolo
Application of Complementary Experimental Techniques to Characterization of the Phase Behavior of [C16mim][PF6] and [C14mim][PF6]
Chem. Mater. 15-16, pp. 3089-9 (2003)

I.D. Desnica-Frankovic, U.V. Desnica, P. Dubcek, M. Buljan, S. Bernstorff, H. Karl, I. Großhans and B. Stritzker
Ion beam synthesis of buried Zn-VI quantum dots in SiO₂ – grazing incidence small-angle X-ray scattering studies
J. Appl. Cryst. **36**, 439-442 (2003)

U. V. Desnica, P. Dubcek, I.D. Desnica-Frankovic, M. Buljan, K. Salamon, O. Milat, S. Bernstorff and C.W. White
GISAXS studies of morphology and size distribution of CdS nanocrystals formed in SiO₂ by ion implantation
Nuclear Instruments and Methods B 200, 191-195 (2003)

U. V. Desnica, P. Dubcek, I.D. Desnica-Frankovic, M. Buljan, S. Bernstorff and S.W. White
Grazing incidence small-angle X-ray scattering studies of the synthesis and growth of CdS quantum dots from constituent atoms in SiO₂ matrix
J. Appl. Cryst. 36, 443-446 (2003)

P. Dubcek, U. V. Desnica, I.D. Desnica-Frankovic, S. Bernstorff and A. Meldrum
GISAXS study of shape and size of CdS nanocrystals formed in monocrystalline silicon by ion implantation
Nuclear Instruments and Methods B 200, 138-141 (2003)

P. Dubcek, B. Pivac, S. Bernstorff, F. Corni, R. Tonini, and G. Ottaviani
Grazing incidence small-angle X-ray scattering study of defects in deuterium implanted monocrystalline silicon
J. Appl. Cryst. 36, 447-449 (2003)

- P. Dubcek, B. Pivac, S. Bernstorff, R. Tonini, F. Corni and G. Ottaviani
GISAXS study of structural relaxation in amorphous silicon
Nuclear Instruments and Methods B 200, 110-113 (2003)
- P. Dubcek, N. Radic and O. Milat
Characterization of grains in tungsten-carbon films
Nuclear Instruments and Methods B 200, 329-332 (2003)
- O. Francescangeli, V. Stanic, L. Gobbi, P. Bruni, M. Iacussi, G. Tosi, and S. Bernstorff
Structure of self-assembled liposome-DNA-metal complexes
Phys. Rev. E 67, 011904 1 - 011904 11 (2003)
- D. Gracin, P. Dubcek, M. Jaksic and S. Bernstorff
Nanostructural properties of amorphous silicon carbide by GISAXS and optical spectroscopy
Thin Solid Films 433 (2003) 88-91
- D. Grosso, F. Banonneau, C. Sanchez, G.J.D.A. Soler-Illia, E.L. Crepaldi, P.A. Albouy, H. Amenitsch, A.R. Balkenende and A. Brunet-Bruneau
A first insight of the mechanisms involved in the self-assembly of 2D-hexagonal templated SiO₂ and TiO₂ mesostructured films during dip-coating
Journal of Sol-Gel Science and Technology 26, pp. 561-565 (2003)
- F. Lo Celso, A. Triolo, F. Triolo, P. Thiyagarajan, H. Amenitsch, M. Steinhart, M. Kriechbaum, J.M.DeSimone and R. Triolo
A combined small-angle neutron and X-ray scattering study of block copolymers micellisation in supercritical carbon dioxide. Small Angle Scattering Study of PEO Based Block Copolymers' Solutions
J. Appl. Cryst. 36, 660-663 (2003)
- Pabst, G., J. Katsaras, V. A. Raghunathan, and M. Rappolt
Structure and Interactions in the Anomalous Swelling Regime of Phospholipid Bilayers.
Langmuir 19, 1716-1722 (2003)
- Gerd Persson, Håkan Edlund and Göran Lindblom
Thermal behaviour of cubic phases rich in 1-monooleoyl-rac-glycerol in the ternary system 1-monooleoyl-rac-glycerol/n-octyl-beta-D-glucoside/water
European Journal of Biochemistry 270, pp. 56-65 (2003)
- B. Pivac, P. Dubcek, S. Bernstorff, A. Borghesi, A. Sassella, and M. Porrini
Small angle X-ray scattering study of oxygen precipitation in silicon
Nuclear Instruments and Methods B 200, 105-109 (2003)
- B. Pivac, O. Milat, P. Dubcek, S. Bernstorff, F. Corni, C. Nobili and R. Tonini
Early stages of bubble formation in helium-implanted (100) silicon
Physica Status solidi (a) 198, No. 1, 29-37 (2003)
- B. Pozo-Navas, V. A. Raghunathan, J. Katsaras, M. Rappolt, K. Lohner, and G. Pabst
Discontinuous Unbinding of Lipid Multibilayers
Phys. Rev. Lett. 91 028101 (2003)

M. Rappolt, A. Hickel, F. Bringezu and K. Lohner
Mechanism of the Lamellar/Inverse Hexagonal Phase Transition Examined by High Resolution X-Ray Diffraction
Biophysical Journal 84, 3111-3122 (2003)

M. Rappolt, M. Vidal, M. Kriechbaum, M. Steinhard, H. Amenitsch, S. Bernstorff, and P. Laggner
Structural, Dynamic and Mechanical Properties of POPC at Low Cholesterol Concentration Studied in Pressure/Temperature Space
Europ. Biophys. J. 31, 575-585 (2003)

Matthias F. Schneider, Roman Zantl, Christian Gege, Richard R. Schmidt, Michael Rappolt and Motomu Tanaka
Hydrophilic / hydrophobic balance determines morphology of glycolipids with oligolactose headgroups
Biophysical Journal 84, 306-313 (2003)

L. Valkova, A. Menelle, N. Borovkov, V. Erokhin, M. Pisani, F. Ciuchi, F. Carsughi, F. Spinozzi, R. Padke, S. Bernstorff and F. Rustichelli
SAXS, SANS and neutron reflectivity studies of LB films of copper tetra-tert-butyl-azaporphyrines
J. Appl. Cryst. 36, 758-762 (2003)

I. Zizak, P. Roschger, O. Paris, Barbara M. Misof, A. Berzlanovich, S. Bernstorff, H. Amenitsch, K. Klaushofer, P. Fratzl
Characteristics of Mineral Particles in the Human Bone-Cartilage Interface
J. Struct. Biol. 141, pp 208-217 (2003)

Publications in print (July 2003)

P. Ausili, M. Pisani, C. Ferrero, S. Finet, P. Mariani
Pressure effects on columnar lyotropics: X-ray diffraction investigation on d(GMP) and GMP
In "High Pressure in Bioscience and Biotechnology", R. Winter Editor, Springer-Verlag (Heidelberg)

J. Baldrian, M. Horky, M. Steinhart, A. Sikora, M. Mihailova H. Amenitsch, S. Bernstorff, G. Todorova
SAXS and DSC study of cocrystallization of low-molecular PEO fractions in polymer blends
SPIE Proceedings „Fibers & Textiles in Eastern Europe“

M. Buljan, K. Salamon, P. Dubcek, S. Bernstorff, I.D. Desnica-Frankovic, O. Milat and U.V. Desnica
Analysis of 2D GISAXS patterns obtained on semiconductor nanocrystals
Vacuum

- G. Cecchi, M.A. Bagni, B. Colombini, C.C. Ashley, H. Amenitsch, S. Bernstorff and P.J. Griffiths
Use of sinusoidal length oscillations to detect myosin conformation by time-resolved x-ray diffraction
 Adv. Exp. Med. Biol.
- M. Cócera, O. López, R. Pons, H. Amenitsch and A. De la Maza
Effect of the electrostatic charge on the mechanism inducing liposome solubilization: A kinetic study by Synchrotron radiation SAXS
 Biophys. J.
- Croce G, Frache A., Milanesio M., Viterbo D., Amenitsch H., Bavestrello G., Benatti U, Giovine M.,
Fiber diffraction study of spicules from marine sponges
 Microsc. Res. Tech.
- U.V. Desnica, M. Buljan, I.D. Desnica-Frankovic, P. Dubcek, S. Bernstorff, M. Ivanda and H. Zorc
Direct ion beam synthesis of II-VI nanocrystals
 Nucl. Instrum. & Methods B
- P. Dubcek, B. Pivac, S. Bernstorff, F. Corni, C. Nobili and R. Tonini
Grazing incidence small angle X-ray scattering study of He irradiation induced defects in monocrystalline silicon
 Nucl. Instrum. & Methods B
- P. Dubcek, B. Pivac, O. Milat, S. Bernstorff and I. Zulim
Study of structural changes in krypton implanted silicon
 Nucl. Instrum. & Methods
- Gracin, Davor; Jaksic, Milko; Dubcek, Pavo; Medunic, Zvonko
Nano-structural properties of amorphous hydrogenated silicon-carbon alloys by IBA technique, optical methods and GISAXS
 Vacuum
- D. Grosso, P.A. Albouy, H. Amenitsch, A.R. Balkenende and F. Babonneau
Time-resolved in-situ X-ray diffraction study of the formation of 3D-hexagonal mesoporous silica films
 Mater. Res. Soc. Symp. Proc. Vol 628
- H. S. Gupta, P. Roschger, I. Zizak, N. Fratzl-Zelman, A. Nader, K. Klaushofer, and P. Fratzl
Mineralized microstructure of calcified avian tendons: a scanning small-angle X-ray scattering study
 Calcif. Tissue Int.
- Hrestak, Kristina; Turkovic, Aleksandra; Dubcek, Pavo; Crnjak Orel, Zorica
Raspröenje rentgenskih zraka sinkrotronskog izvora pri malom kutu u nanostrukturnim V/Ce oksidnim slojevima
 Strojarstvo

F. Lo Celso, A. Triolo, F. Triolo, J. McClain, J.M. Desimone, R.K. Heenan, H. Amenitsch, R. Triolo

Industrial Applications of Aggregation of Block Copolymers in Supercritical CO₂: a SANS Study

Applied Physics A

M. Lucic-Lavcevic and A. Turkovic

The morphological parameter of nanostructured TiO₂ films

Acta materialia

Lucic-Lavcevic, Magdy, Dubcek, Pavo; Turkovic, Aleksandra

Nanostructured CeO₂ thin films: a Saxs study of the interface between grains and pores

Scripta Materialia

A. Orthen, H. Wagner, H.J. Besch, R.H. Menk, A.H. Walenta and U. Werthenbach.

Investigation of the performance of an optimised MicroCAT, a GEM and their combination by simulations and current measurements

Nucl. Instr. and Methods A

M. Pisani, T. Narayanan, G.M. Di Gregorio, C. Ferrero, H. Amenitsch and P. Mariani

Compressing inverse lyotropic phases: effects on dioleoyl phosphatidyl ethanolamine at low hydration

Phys. Rev. E

N. Radic, A. Tonejc, J. Ivkov, P. Dubcek, S. Bernstorff, Z. Medunic

Sputter-deposited amorphous-like tungsten

Surface and Coatings Technology

J.B. Rosenholm, M. Lindén

Controlled synthesis and processing of ceramic oxides – A molecular approach

Handbook of Surface and Colloid Science, 2nd edition, CRC Press

H. Wagner, H.J. Besch, R.H. Menk, A. Orthen, A. Sarvestani, A.H. Walenta, H. Walliser

On the dynamic two-dimensional charge diffusion of the interpolating readout structure employed in the MicroCAT detector

Nucl. Instr. and Meth.

H. Wilhelm, A. Paris, E. Schafler, S. Bernstorff, J. Bonarski, T. Ungar, M. J. Zehetbauer,

„Evidence of dislocations in melt-crystallised and plastically deformed polypropylene“,

Mater.Sci.Eng.A.

International Conferences and Workshops in 2002

P. Agren, M Lindén, H. Amenitsch, A. Hahn, D. Kumar, T. Narayanan

Formation of mesoporous particles (MCM 41) in the early stages: an insitu small angle X-ray scattering study

E-MRS 2002 Spring Meeting, Strasbourg (France), June 18 to 21, 2002 (poster)

P. Agren, M Lindén, H. Amenitsch, A. Hahn, D. Kumar, T. Narayanan
Formation of mesoporous particles (MCM 41) in the early stages: an insitu small angle X-ray scattering study
XII International Conference on Small-Angle Scattering (SAS2002), Venice, Italy, August 25-29, 2002 (poster)

H. Amenitsch
Application of small angle scattering in material sciences
ETH, Lausanne, Swiss, 2.-5.11.02

H. Amenitsch
Small Angle Scattering from bulk to surfaces
MPI, Mühlheim, Germany, 26.11.02

H. Amenitsch
SAXS under extreme conditions
ICTP School for Synchrotron Radiation, Trieste, Italy, 8.5.02 (invited talk)

H. Amenitsch and M. Rappolt
Discussion of the experimental results taken at Elettra
ICTP School for Synchrotron Radiation, Trieste, Italy, 10.5.02 (invited talk)

H. Amenitsch, U. Benatti, M. Causà, G. Croce, A. Frache, M. Giovine, L. Marchese, M. Milanesio, D. Viterbo
Chemical and physical investigations of siliceous spicules from natural sponges
Giornate Italo-Francesi di Chimica Juan les Pins, France. 18-19 april 2002

H. Amenitsch, U. Benatti, G. Croce, A. Frache, M. Giovine, M. Milanesio, D. Viterbo
SAXS study of spicules from marine sponges
XXXII Congresso Associazione Italiana di Cristallografia, Bressanone, Italy. 24-27 Settembre 2002

H. Amenitsch, C.V. Teixeira, M. Rappolt, P. Laggner
Use of surface diffraction to study lipids under the influence of salts
10th International Users' Meeting, ELETTRA, Trieste, Italy, 29.10.2002 (poster)

F. Babonneau
Mesostructured materials: from bulk to surfaces
European Materials Research Society, "Synchrotron radiation and materials science",
Strasbourg (France), 17-20 June 2002 (Invited talk)

F. Babonneau, D. Grosso, V. Goletto, B. Alonso, P.A. Albouy, H. Amenitsch, M. Linden
Surfactant-templated materials: time-resolved in-situ SAXS measurements during the formation of silica and organosilica powders and films
SFC Eurochem, Toulouse (France), 7-11 July 2002 (talk)

F. Babonneau

Caractérisation structurale de poudres et films de silice mésoporeuse fonctionnalisée par des groupes organiques

Laboratoire de Chimie-Physique, Université Paris-Sud Orsay (France), 18 January 2002 (seminar talk)

F. Babonneau

Mesostructured silica and organosilica materials : from bulk to surfaces

Department of Chemistry, University of California, Los Angeles (USA), 10 April 2002 (seminar talk)

F. Babonneau

Mesostructured silica and organosilica materials: from bulk to surfaces

Department of Materials Science, Università Tor Vergata, Roma (Italie), 27 June 2002 (seminar talk)

J. Baldrian, M. Steinhart, A. Sikora, H. Amenitsch, S. Bernstorff and G. Todorova

Real-time SAXS and DSC study of structure development in crystalline polyer blends

XII International Conference on Small-Angle Scattering (SAS2002), Venice, Italy, August 25-29, 2002 (poster, Abstract p. 139)

J. Baldrian, M. Steinhart, A. Sikora, G. Todorova, H. Amenitsch, S. Bernstorff

Cocrystallization behaviour of low-molecular-weight PEO fractions in polymer blends

4th Czech-Korean Joint Symposium on Macromolecular Chemistry, Prague 2002, Lecture

S. Bernstorff

GISAXS, GID and X-Ray Reflectivity in Materials Science

ICTP School for Synchrotron Radiation, Trieste, Italy, 9.5.02 (invited talk)

M. Buljan, K. Salamon, P. Dubcek, S. Bernstorff, I.D. Desnica-Frankovic, O. Milat, U. V. Desnica

Analysis of 2D GISAXS spectra of CdS nanocrystals in SiO₂ matrix

IX. International Scientific Meeting "Vacuum science and technologies", Trakoscan, Croatia, May 15, 2002 (talk)

M. Buljan, K. Salamon, P. Dubcek, S. Bernstorff, I.D. Desnica-Frankovic, O. Milat and U.V. Desnica

Determination of size distribution and concentration of semiconductor nanocrystals from 2D GISAXS patterns

9th Joint Vacuum Conference (JVC-9), Schloss Seggau, Leibnitz by Graz, Austria, June 16 - 20, 2002 (poster)

M. Buljan, K. Salamon, P. Dubcek, S. Bernstorff, I.D. Desnica-Frankovic, O. Milat and U.V. Desnica

Determination of size distribution and concentration of semiconductor nanocrystals from 2D GISAXS patterns

10th International Users' Meeting, ELETTRA, Trieste, Italy, 29.10.2002 (poster)

P. Bussian, P. Ågren, M. Lindén, W. Schmidt, H. Amenitsch and F. Schüth
Zinc Sulfide Precipitation in a Liquid Jet: An in situ SAXS study
XII International Conference on Small-Angle Scattering (SAS2002), Venice, Italy, August 25-29, 2002 (talk)

T. Clausen, T. Schmidt, S. Gangopadhyay, J. Falta, J. I. Flege, S. Heun, S. Bernstorff, P. Dubcek, L. Gregoratti, A. Barinov, B. Kaulich, M. Kiskinova
Strukturelle Untersuchungen von ultradünnen Si₃N₄-Filmen
Spring meeting of the German Physical Society, Regensburg, Germany, 11.03.-15.03.2002 (Talk O 19.5)

I.D. Desnica-Frankovic, U.V. Desnica, P. Dubcek, M. Buljan, S. Bernstorff, H. Karl, I. Großhans and B. Stritzker
Ion beam synthesis of buried Zn-VI quantum dots in SiO₂ – GISAXS studies
XII International Conference on Small-Angle Scattering (SAS2002), Venice, Italy, August 25-29, 2002 (poster)

I.D. Desnica-Frankovic, U.V. Desnica, P. Dubcek, M. Buljan, S. Bernstorff, H. Karl and I. Großhans
GISAXS studies of ZnS and ZnTe nanocrystals formed in SiO₂ by ion implantation
10th International Users' Meeting, ELETTRA, Trieste, Italy, 29.10.2002 (poster)

U.V. Desnica, P. Dubcek, M. Buljan, I.D. Desnica-Frankovic, S. Bernstorff, C.W. White
GISAXS Analysis of CdS quantum dots in SiO₂ matrix
10th International Users' Meeting, ELETTRA, Trieste, Italy, 29.10.2002 (poster)

U.V. Desnica, P. Dubcek, I.D. Desnica-Frankovic, M. Buljan, K. Salomon and S. Bernstorff
GISAXS Studies of Morphology and Size Distribution of CdS Nanocrystals formed in SiO₂ by Ion Implantation
E-MRS 2002 Spring Meeting, Strasbourg (France), June 18 to 21, 2002 (poster)

U. V. Desnica, P. Dubcek, I.D. Desnica-Frankovic, M. Buljan, K. Salomon, O. Milat and S. Bernstorff
GISAXS studies of the synthesis and growth of CdS quantum dots from constituent atoms in SiO₂ matrix
XII International Conference on Small-Angle Scattering (SAS2002), Venice, Italy, August 25-29, 2002 (poster)

U. Desnica, B. Pivac, D. Desnica Franović, B. Etlinger, P. Dubcek, M. Pavlovic, N. Urli, I. Kovacevic, M. Buljan
The influence of defects and nano-structures on properties of semiconductors
Nano-science Network - Scientific-professional meeting, Zagreb, December, 19, 2002.

P. Dubcek
Istrazivanje strukture tankih filmova raspršenjem rendgenskog zracenja pod malim kutevima
IX. International Scientific Meeting "Vacuum science and technologies", Trakoscan, Croatia, May 15, 2002 (talk)

- P. Dubcek, U. V. Desnica, I.D. Desnica-Frankovic and S. Bernstorff
GISAXS Study of Shape and Size of CdS Nanocrystals formed in Monocrystalline Silicon by Ion Implantation
 E-MRS 2002 Spring Meeting, Strasbourg (France), June 18 to 21, 2002 (talk)
- P. Dubcek, B. Pivac, S. Bernstorff, R. Tonini, F. Corni and G. Ottaviani
Grazing incidence small angle X-Ray scattering study of irradiation induced defects in monocrystalline silicon
 XII International Conference on Small-Angle Scattering (SAS2002), Venice, Italy, August 25-29, 2002 (poster)
- P. Dubcek, B. Pivac, S. Bernstorff, R. Tonini, F. Corni and G. Ottaviani
GISAXS study of defects in deuterium implanted monocrystalline silicon
 XII International Conference on Small-Angle Scattering (SAS2002), Venice, Italy, August 25-29, 2002 (poster)
- P. Dubcek, B. Pivac, S. Bernstorff, F. Corni, R. Tonini and G. Ottaviani
GISAXS Study of Structural Relaxation in Amorphous Silicon
 E-MRS 2002 Spring Meeting, Strasbourg (France), June 18 to 21, 2002 (poster)
- P. Dubcek, B. Pivac, O. Milat, S. Bernstorff, R. Tonini, F. Corni and G. Ottaviani
GISAXS Study of Hydrogen Implanted Silicon
 E-MRS 2002 Spring Meeting, Strasbourg (France), June 18 to 21, 2002 (poster)
- P. Dubcek, N. Radic and O. Milat
Characterization of grains in tungstun-carbon films
 E-MRS 2002 Spring Meeting, Strasbourg (France), June 18 to 21, 2002 (poster)
- J. Falta, T. Schmidt, T. Clausen, O. Brunke, S. Gangopadhyay, J. I. Flege, S. Heun, S. Bernstorff, P. Dubcek, L. Gregoratti, A. Barinov, B. Kaulich, M. Kiskinova
Structural Characterization of Ultra-thin SIN Films on Si(111)
 E-MRS 2002 Spring Meeting, Strasbourg (France), June 18 to 21, 2002 (talk)
- V. Goletto, B. Alonso, D. Grosso, G. Trimmel, F. Babonneau, P.A. Albouy, H. Amenitsch, M. Linden
Structural characterization of Periodic porous organosilica powders and thin films
 Materials Research Society, "Hybrid Organic/Inorganic Materials", San Francisco (USA), 1-5 April 2002 (Poster)
- D. Gracin, M. Jaksic, P. Dubcek, and Z. Medunic
The nano-structural properties of amorphous silicon-carbon alloys investigated by IBA technique, optical spectroscopy and GISAXS
 9th Joint Vacuum Conference (JVC-9), Schloss Seggau, Leibnitz by Graz, Austria, June 16 - 20, 2002 (poster)
- D. Gracin, P. Dubcek and M. Jaksic
Nanostructural properties of amorphous silicon carbide by GISAX and optical spectroscopy
 ICTF 12, Bratislava, Slovakia, Sept. 15-20, 2002

A. Gupta, B.A. Dasannaharya, G. Principi, A. Maddalena, M. Meyer, S. Dal Toe', P. Sharma, N. Paul, S. Bernstorff and H. Amenitsch

In-situ SAXS and WAXS studies of nanocrystallization of some softmagnetic alloys
10th International Users' Meeting, ELETTRA, Trieste, Italy, 29.10.2002 (poster)

H.S. Gupta, K. Misof, I. Zizak, P. Messner, P. Roschger, S. Bernstorff, H. Amenitsch, K. Klaushofer and P. Fratzl

In-situ synchrotron X-ray scattering investigations of nanostructured changes of mineralized collagen fibrils during tensile testing
52. Annual Meeting of the Austrian Physical Society, Leoben, Austria, 23.-26.9.2002 (poster P-NES22)

H. S. Gupta, K. Misof, I. Zizak, P. Messmer, P. Roschger, S. Bernstorff, K. Klaushofer, and P. Fratzl

Non-linear elastic behavior in mineralized collagen relates to inhomogeneous deformation at the fibrillar level
Gordon Conference „Biomaterialization“ 2002, Colby-Sawyer College, New London, New Hampshire, USA, August 11 – 16, 2002. (poster)

A. Hahn, D. Kumar, H. Amenitsch, P. Agren, M Linden, R. Menk, A. Hahn, T. Narayanan, K.K. Unger

Nucleation and growth of mesoporous stoeber particles studied by time-resolved small angle X-ray scattering
E-MRS 2002 Spring Meeting, Strasbourg (France), June 18 to 21, 2002 (talk)

Hrestak, Kristina; Turkovic, Aleksandra; Dubcek, Pavo; Crnjak Orel, Zorica

Utjecaj interkalacije Li⁺ iona u matricu nanostrukturnih V/Ce oksida
IX. International Scientific Meeting "Vacuum science and technologies", Trakoscan, Croatia, May 15, 2002 (talk)

P. Laggner

Supramolecular phases in bulk and at surfaces. From biotechnology to nanotechnology.
UNESCO Workshop, Bahia Blanca, Argentina, 23.-26.04.02 (talk)

P. Laggner

Time-resolved characterization of controlled-release formulations by small- and wide-angle X-ray scattering
IWPCPS, 3rd Int. Workshop on the Physical Characterization of Pharmaceutical Solids, Oxford, UK, 9.-14.06.02 (talk)

P. Laggner

Small- and wide-angle x-ray scattering in food- and drug-research and industrial practice
ICXRI 2002, Int. Conf. on X-Rays and Related Techniques in Research and Industry, Kuala Lumpur, Malaysia, 30.-31.10.02 (invited talk)

P. Laggner

Technique and application of small- and wide-angle X-ray scattering
Shahidan Radiman, Univ. of Kebangsaan Malaysia, Faculty of Science and Technology, Selangor, D. E., Bangi, Malaysia, 1.11.02 (invited talk)

P. Laggner

Single-molecule / high-throughput / real-time: the challenges for X-ray structure research
Inst. of Materials Research & Engineering, Synchrotron Light Source, Singapore, Malaysia,
5.11.02 (invited talk)

P. Laggner, H. Amenitsch, M. Kriechbaum, M. Rappolt, G. Pabst

Biomimetic reactions with liposomes in bulk and at solid surfaces

1st Central European Conf. „Chemistry towards Biology,, Portoros, Slovenia,

8.-12.09.02 (invited lecture)

P. Laggner, H. Amenitsch and M. Kriechbaum

Single-Molecule / High-Throughput / Real-Time: The Challenges for X-Ray Structure Research"

SAMBA 2 (Symposium on Applications of Particle Detectors in Medicine, Biology and Astrophysics), Miramare, Trieste, Italy, 27-29 May 2002 (invited talk)

F. Lo Celso, A. Triolo, F. Triolo, P. Thiagarajan, H. Amenitsch, M. Steinhart, M. Kriechbaum and R. Triolo

A combined SANS SAXS study of block copolymers micellisation in supercritical carbon dioxide

XII International Conference on Small-Angle Scattering (SAS2002), Venice, Italy, August 25-29, 2002 (talk)

F. Lo Celso, A. Triolo, F. Triolo, P. Thiagarajan, R. K. Heenan, J.S. Lin, H. Amenitsch, L. Paduano and R. Triolo

Small Angle Scattering Study of PEO Based Block Copolymers' Solutions

XII International Conference on Small-Angle Scattering (SAS2002), Venice, Italy, August 25-29, 2002 (poster)

F. Lo Celso, A. Triolo, F. Triolo, A. Wiedenmann, M. Steinhart, M. Kriechbaum, H. Amenitsch

SAS of block copolymers in normal and supercritical fluids

ESS conference, Bonn, Germany, May 16-17, 2002 (poster)

O. López, M. Cócera, R. Pons, H. Amenitsch, J. Caelles, J.L. Parra, L. Coderch, A. de la Maza

Time resolved SAXS study by synchrotron radiation of the mechanism inducing the solubilization of lipid membranes: effect of electrostatic charges

First International Conference on „Biomedical Spectroscopy: From molecules to men“, Cardiff, Wales, UK, 2002 (Poster)

P. Mariani

SAS shape analysis in assessing protein structures obtained by computational prediction techniques

XII International Conference on Small Angle Scattering, Venezia, 26-29 Agosto 2002 (invited plenary lecture)

P. Mariani

Pressure effects on columnar lyotropics: anisotropic compressibilities in guanosine monophosphate four-stranded helices

LLB Round Tables, Orsay (Francia) 28-29 Novembre 2002 (invited lecture)

Menk, R.H., H. Amenitsch, F. Arfelli, F. Montanari, and D. Dreossi

Preliminary results of A combined USAXS and diffraction enhanced imaging system with synchrotron radiation

IEEE International Symposium on Biomedical Imaging Washington DC, July 7-10 2002

G. Pabst

Modelling of diffraction data from fluid like multibilayer systems

HMI, Berlin, Germany, 17. 6. 2002 (invited talk)

G. Pabst

Recent developments of global x-ray analysis techniques of multibilayer systems

XIIth Intern. Conf. On Small-Angle Scattering, Venice, Italy, 25-29.08.2002 (talk, IUCr Otto-Kratky Award for Young Scientists!)

G. Pabst, Y. Liu, M. Rappolt, H. Amenitsch, P. Laggner, S. Tristram-Nagle, J.F. Nagle, V. A. Raghunathan and J. Katsaras

Recent developments in global diffraction data analysis of lipid/water systems

E-MRS 2002 Spring Meeting, Strasbourg, France, June 18 to 21, 2002 (poster)

G. Pabst, Y. Liu, M. Rappolt, H. Amenitsch, P. Laggner, S. Tristram-Nagle, J.F. Nagle, V. A. Raghunathan and J. Katsaras

Recent developments in global diffraction data analysis of lipid/water systems

10th International Users' Meeting, ELETTRA, Trieste, Italy, 29.10.2002 (poster)

A. Paris, E. Schafler, H. Wilhelm, J. Bonarski, M. Zehetbauer

Application of X-Ray Multiple Whole Profile Analysis (XMPA) for Identification of Deformation Induced Dislocations in Semicrystalline α -Polypropylene

52. Annual Meeting of the Austrian Physical Society, Leoben, Austria, 23.-26.9.2002 (poster P-FKP34)

A. Paris, S. Bernstorff, H. Wilhelm, E. Schafler, J. Bonarski, M. Zehetbauer

Application of X-Ray Multiple Whole Profile Analysis (XMPA) for Identification of Deformation Induced Dislocations in Semicrystalline α -Polypropylene

10th International Users' Meeting, ELETTRA, Trieste, Italy, 29.10.2002 (poster)

A. Paris, H. Wilhelm, E. Schafler, M. Zehetbauer

Application of X-Ray Multiple Whole Profile Analysis (XMPA) for Identification of Deformation Induced Dislocations in Semicrystalline α -Polypropylene

Junior Euromat 2002, Lausanne, Schweiz (poster)

A. Paris und H. Wilhelm

Synchrotron WAXS & XPA Messungen an verformtem Polypropylen

Gruppenseminar Hochleistungsmaterialien, Inst. f. Materialphysik, Univ. Wien, Dezember 2002, Vienna, Austria (Talk)

B. Pivac, P. Dubcek, S. Bernstorff, A. Borghesi, A. Sassella and M. Porrini
SAXS Study of Oxygen Precipitation in Silicon
E-MRS 2002 Spring Meeting, Strasbourg (France), June 18-21, 2002 (poster)

M. Rappolt, A. Hickel, F. Bringezu and K. Lohner
Interface study in the lamellar/inverse hexagonal phase region of PEs: a major component of bacterial membranes
XII International Conference on Small-Angle Scattering (SAS2002), Venice, Italy, August 25-29, 2002 (talk)

M. Rappolt, A. Hickel, F. Bringezu and K. Lohner
Structural study of the lamellar/inverse-hexagonal phase region of phosphatidylethanolamines
10th International Users' Meeting, ELETTRA, Trieste, Italy, 29.10.2002 (poster)

M. Rappolt, Hickel, Bringezu and K. Lohner
Structural study in the lamellar/inverse hexagonal phase region of phosphatidylethanolamines.
43rd ICBL, Graz, Austria, 11.-14.9.2002 (poster)

K. Salamon, O. Milat, P. Dubcek, N. Radic
Structure of W-C films deposited on Si substrate: surface and subsurface analysis by GISAXS and SAXS patterns
9th Joint Vacuum Conference (JVC-9), Schloss Seggau, Leibnitz by Graz, Austria, June 16 - 20, 2002 (poster)

Salamon, Kresimir, Milat, Ognjen, Dubcek, Pavo, and Radic, Nikola
Povrainska i Podpovrainska analiza nanostrukture W-C sloja na si podlozi
Zbornik sauetaka 9. Medunarodni sastanak Vakuumska znanost i tehnika / Radic, Nikola (ed.), Zagreb : Hrvatsko vakuumsko druotvo, 2002, p. 26

F. Spinozzi, F. Rustichelli, H. Amenitsch, P. Tortora, R. Casadio and P. Mariani
Structure of sulfolobus solfataricus carboxypeptidase determined by molecular modelling and SAXS
XII International Conference on Small-Angle Scattering (SAS2002), Venice, Italy, August 25-29, 2002 (poster)

E. Schafner
Röntgen Bragg Profilanalyse (XPA)– Eine universelle Methode zur Charakterisierung der Mikrostruktur plastisch verformter Materialien
Institut für Materialphysik der Universität Wien, Juni 2002 (invited talk)

C.V. Teixeira, H. Amenitsch, M. Rappolt, M. Majerovic and P. Laggner
Use of surface diffraction to study phospholipids under influence of salt.
14th Surfactants In Solution Symposium, Barcelona, Spain, 9.-14.06.2002 (talk)

C. V. Teixeira, H. Amenitsch, M. Rappolt and P. Laggner
Influence of salts in membranes through surface diffraction
XII International Conference on Small-Angle Scattering (SAS2002), Venice, Italy, August 25-29, 2002 (poster)

W. Tesch, P. Roschger, I. Zizak, O. Paris, S. Bernstorff, H. Amenitsch, K. Klaushofer and P. Fratzl

Characterization of mineralization in bone diseases
OSTEOLOGIE 2002, Graz, Austria, 6.-10.3.2002 (Poster)

W. Tesch, P. Roschger, S. Bernstorff, H. Amenitsch, K. Klaushofer, and P. Fratzl

Bone matrix mineralization in Paget's and in coeliac disease
Osteologie 2002, Graz, Austria, March 6 – 10, 2002. (poster)

A. Triolo, V. Baiata, F. Lo Celso, S. Bernstorff, C. Gordon and R. Triolo

Room temperature ionic liquids: a TR SAXS-WAXS investigation
XII International Conference on Small-Angle Scattering (SAS2002), Venice, Italy, August 25-29, 2002 (poster)

A. Triolo, L. Crapanzano, A. Wiedenmann, S. Bernstorff, R. Triolo

SAX Study of PMMA-b-PEO di-block in Aqueous Solution
ESS conference, Bonn, Germany, May 16-17, 2002 (poster)

L. Valkova, A. Menelle, N. Borovkov, V. Erokhin, M. Pisani, F. Ciuchi, F. Spinozzi, S. Bernstorff, R. Padke, and F. Rustichelli

SAXS, SANS and neutron reflectivity study of azaporphyrine LB films
XII International Conference on Small-Angle Scattering (SAS2002), Venice, Italy, August 25-29, 2002 (poster)

M.F. Vidal, M. Kriechbaum, M. Rappolt, M. Steinhart, H. Amenitsch, S. Bernstorff, P. Laggner

Dual effect of cholesterol on the fluidity in phospholipid bilayers. Time resolved synchrotron SAXS studies
14th Surfactants In Solution Symposium, Barcelona, Spain, 9.-14.06.2002 (poster)

M. F. Vidal, M. Kriechbaum, M. Steinhart, P. Laggner, C. V. Teixeira, M. Rappolt, H. Amenitsch and S. Bernstorff

Pressure scanning SAXS on lipid/cholesterol mixtures
XII International Conference on Small-Angle Scattering (SAS2002), Venice, Italy, August 25-29, 2002 (poster)

M. Vidal, M. Kriechbaum, M. Rappolt, M. Steinhart, H. Amenitsch, S. Bernstorff and P. Laggner

Dual effect of cholesterol on the fluidity of lipid membranes. Time-resolved SAXS studies
43rd ICBL - International Conference on the Bioscience of Lipids, Graz, AT, 11.-14.9.2002 (poster)

Vidal, Kriechbaum, Steinhart, Laggner, Teixeira, Rappolt, Amenitsch, Bernstorff

Pressure scanning SAXS on lipid/cholesterol mixtures
10th Int. Users' Meeting, Trieste, Italy, 29.10.2002 (Poster)

H. Wagner, A. Orthen, H.J. Besch, R.H. Menk, A.H. Walenta and U. Werthenbach
On the improvement of a flexibly applicable gaseous 2D MicroCAT detector for highly time-resolved X-ray imaging

SAMBA 2 (Symposium on Applications of Particle Detectors in Medicine, Biology and Astrophysics), Miramare, Trieste, Italy, 27-29 May 2002 (invited talk)

A. Zidansek, S. Kralj, G. Lahajnar, S. Sumer, H. Amenitsch, M. Rappolt, S. Bernstorff
Influence of the CPG Confinement on the Nematic-Smectic Liquid Crystal Phase Transition
19th International Liquid Crystal Conference (ILCC), Edinburg, Great Britain, July 2002

ELETTRA Highlights 2001-2002

H. Amenitsch, G. Bavestrello, U. Benatti, M. Causà, G. Croce, M. Giovine, M. Milanesio, D. Viterbo

SAXS study of spicules from marine sponges

Elettra Highlights 2001-2002, 26-28 (2002)

P.J. Griffiths, M.A. Bagni, B. Colombini, H. Amenitsch, S. Bernstorff, C.C. Ashley and G. Cecchi

Time-resolved X-ray studies of the molecular motor, myosin, in living cells

Elettra Highlights 2001-2002, 29-31 (2002)

A. Triolo, F. Lo Celso, V. Baiata, R. Triolo, H. Amenitsch, S. Bernstorff and C.M. Gordon

Ionic liquids: phase diagram characterisation with combined SAXS-WAXS

Elettra Highlights 2001-2002, 54-57 (2002)

SAXS Training Courses

In May 2002 Heinz Amenitsch, Sigrid Bernstorff and Michael Rappolt participated at the international school „ICTP School for Synchrotron Radiation“, organized by the International Centre for Theoretical Physics (ICTP), Trieste (Italy) in giving lectures, carrying out experiments at the Austrian SAXS beamline and organizing a SAXS tutorial from 8.5.-10.5.02.

In the framework of the 12th international conference on small-angle X-ray scattering (SAS 2002, 25.-29.8.2002, Venice, Italy), a workshop on Small Angle X-ray Scattering (23.8.-24.8.2002) was held ELETTRA (Trieste, Italy). This workshop was organized by Heinz Amenitsch, Sigrid Bernstorff, Manfred Kriechbaum and Michael Rappolt.

In collaboration with Prof A. Cesaro, BBCM, University of Trieste, the SAXS group (Heinz Amenitsch, Sigrid Bernstorff and Michael Rappolt) gave lectures and experimental tutorials of the SAXS technique for the chemistry students of the University of Trieste on the 12.12.2002.

Master Theses (Tesi di Laurea)

Torben Clausen

Strukturuntersuchungen an ultradünnen Siliziumnitridfilmen
Universität Bremen, Germany (2002)

Gloriana Evangelisti

Effetti della pressione idrostatica sulle proprietà strutturali e sulla stabilità di sistemi biologici macromolecolari: studio delle quadrieliche di guanosina monofosfato mediante diffrazione dei raggi X
Tesi di Laurea in Scienze Biologiche, Facoltà di Scienze Matematiche, Fisiche e Naturali, Università di Ancona, Italia, A.A. 2001/2002

Lydia Paccamiccio

Effetti della pressione, della composizione e della temperatura su sistemi lipidici di membrana. Il caso della DOPE
Tesi di Laurea in Scienze Biologiche, Facoltà di Scienze Matematiche, Fisiche e Naturali; Università di Ancona, Italia, A.A. 2001/2002

Alfred Paris

Application of the Bragg Profile Analysis for the determination of deformation induced dislocations in Polypropylene
Diploma Thesis, University of Technology, Wien, and University of Vienna, Wien, Austria (2002)

PhD Theses

Michela Pisani

Effetti della pressione sulle proprietà strutturali di sistemi liotropici di interesse biologico
University of Ancona, Italy, 12/ 2001

M. Fernandez-Vidal

Effects of Salts, Cholesterol and Melittin on Phospholipid Membranes. X-Ray Studies in the Concentration-Pressure-Temperature Space.
Technical Univ. Graz, Austria, 09/2002

Pamela Ausili

Studio delle proprietà strutturali di quadrieliche di guanosina mediante diffrazione dei raggi X: effetti della temperatura, concentrazione, forza ionica, pH e pressione meccanica
Università di Ancona, Italy, 11/ 2002

Walter Tesch

Influence of mineral particle characteristics on the local mechanical properties of calcified tissues
Montanuniversitaet Leoben, Leoben, Austria, 2002

Author Index

AUSILI, P.	77
AICHMAYER, B.	80
ALEXE, G.	40
AMENITSCH, H.	42, 57, 63, 65, 73, 76, 77, 83, 85, 86, 88, 90, 93, 95, 97, 100, 102, 104, 110
ASHLEY, C.C.	73
ASWAL, V.K.	100
BABONNEAU, F.	104
BAGNI, M.A.	73
BALDRIAN, J.	95
BAVESTRELLO, G.	42
BENATTI, U.	42
BENES, L.	97
BERNSTORFF, S.	40, 45, 47, 49, 51, 53, 55, 57, 61, 68, 70, 73, 77, 80, 86, 90, 95, 97, 100, 110
BESCH, H.J.	110
BLUM, R.	104
BONARSKI, J.	68
BORGHESI, A.	61
BOWEN, P.	65
BULJAN, M.	45, 47
BUSCALIA, V.	65
CECCHI, G.	73
CINELLI, S.	90
CLAUSEN, T.	40
COLOMBINI, B.	73
CORNI, F.	49, 51, 53
CROCE, G.	42
DESNICA, U.V.	45, 47
DESNICA-FRANKOVIC, I.D.	45, 47
DI GREGORIO, G.M.	86
DUBCEK, P.	45, 47, 49, 51, 53, 55, 61
FALCARO, P.	102
FALTA, J.	40
FRACHE, A.	42
FRATZL, P.	80
GIOVINE, M.	42
GOLETTA, V.	104
GOYAL, P.S.	100
GRIFFITHS, P.J.	73
GROBHANS, I.	47
GROSSO, D.	76, 102
GUPTA, A.	57
GUPTA, M.	57
GUPTA, H.S.	80

HOLZAPFEL, G.A.	88
HOMMEL, D.	40
INNOCENZI, P.	102
JONGEN, N.	65
KALNIN, D.	83
KARL, H.	47
KELLER, G.	83
KLAUSHOFER, K.	80
KRIECHBAUM, M.	77, 90, 95, 97
LAGGNER, P.	76, 88, 93
LINDEN, M.	104
LO CELSO, F.	59
LOHNER, K.	85
MAGGINI, M.	102
MARCHESE, L.	42
MARIANI, P.	77, 86, 90
MELÁNOVÁ, K.	97
MENK, R-H.	110
MILANESIO, M.	42
MILAT, O.	45, 55
MISOF, K.	80
OLLIVON, M.	83
ONORI, G.	90
OTTAVIANI, G.	49, 51, 53
PACCAMICCIO, L.	86
PABST, G.	85
PADUANO, L.	59
PARIS, A.	68
PASSOW, T.	40
PISANI, M.	77, 86
PIVAC, B.	49, 51, 53, 61
PORRINI, M.	61
POZO-NAVAS, B.	85
PROBNIG, F.	85
RADIC, N.	55
RAPPOLT, M.	76, 88, 93
REDDY, V.R.	57
RIBARIK, G.	70
ROSCHGER, P.	80
SALAMON, K.	45
SAPRA, S.	63
SARAIYA, A.	57
SARMA, D.D.	63
SASSELLA, A.	61
SCHAFFER, O.	83
SCHAFLER, E.	68, 70
SCHMIDT, TH.	40
SCHULZE-BAUER, C.A.J.	88

SIKORA, A.	95
SOARE, L.C.	65
SOMMER, G.	88
SPINOZZI, F.	90
STEINHART, M.	95, 97
STRITZKER, B.	47
TARKOWSKI, L.	70
TEIXEIRA, C.V.	93
TIEMANN, M.	104
TODOROVA, G.	95
TONINI, R.	49, 51, 53
TRIOLO, A.	59
TRIOLO, R.	59
UNGAR, T.	68
VALENTA, A.	80
VISWANATHA, R.	63
VITERBO, D.	42
VOLTOLINA, F.	110
WEBER, M.	80
WHITE, C.W.	45
WILHELM, H.	68, 70
WILLE, H.	83
ZEHETBAUER, M.	68, 70
ZIDANŠEK, A.	108
ZIMA, V.	97